Multiscale Modeling and Analysis of Nanofibers and Nonwoven Materials

by Sezen Buell

M.S. Mechanical Engineering
Koc University, 2004

B.S. Mechanical Engineering
Bogazici University, 2002

Submitted to the Department of Materials Science and Engineering
in partial fulfillment of the requirements for the degree of

DOCTOR OF PHILOSOPHY IN MATERIALS SCIENCE AND ENGINEERING

at the

MASSACHUSETTS INSTITUTE OF TECHNOLOGY

February 2010

Signature of Author: _____
Department of Materials Science and Engineering
January 04, 2010

Certified by: _____
Gregory C. Rutledge
Lammot du Pont Professor of Chemical Engineering
Thesis Advisor

Certified by: _____
Krystyn J. Van Vliet
Thomas Lord Associate Professor of Materials Science and Engineering
Thesis Advisor

Accepted by: _____
Christine Ortiz
Associate Professor of Materials Science and Engineering
Chair, Departmental Committee on Graduate Students

Multiscale Modeling and Analysis of Nanofibers and Nonwoven Materials

by

Sezen Buell

Submitted to the Department of Materials Science and Engineering in partial fulfillment of the requirements for the degree of Doctor of Philosophy in Materials Science and Engineering

Abstract

Nanostructured fibrous materials have been made more readily available in large part owing to recent advances in electrospinning, which is a technique for the production of nanofibers with diameters down to the range of a few nanometers. The nonwoven structure has unique features, including interconnected pores and a very large surface to volume ratio, which enable such nonwoven materials to have many applications. The properties of the fibers and nonwoven fabrics produced, as well as the means for characterizing these, have remained bottlenecks in the development of the technology, both for scale-up purposes and for quality control and reproducibility during fabrication. The aim of this thesis is to model and identify the size dependent properties of polymeric nanofibers, to evaluate the interactions between two fibers and to construct a framework to model the nonwoven mats.

First, molecular dynamics (MD) simulations are used to investigate the properties of polymeric nanofibers. The fibers consist of chains that mimic the prototypical polymer polyethylene that have diameters in the range 1.9-23.0 nm. We analyzed these nanofibers for signatures of emergent behavior in their structural, thermal and mechanical properties as a function of diameter. The mass density at the center of all fibers is constant and comparable to that of the bulk polymer. The surface layer thickness ranges from 0.78 to 1.39 nm for all fibers and increases slightly with fiber size. The calculated interfacial excess energy is 0.022 J/m^2 for all of the nanofibers simulated. The chains at the surface are more confined compared to the chains at the center of the nanofiber; the latter acquire unperturbed dimensions in sufficiently large nanofibers. Consistent with experiments and simulations of amorphous polymer films of nanoscale thickness, the glass transition temperature of these amorphous nanofibers decreases with decreasing fiber diameter, and is independent of molecular weight over the range considered. We find that, for a given temperature, the Young's elastic modulus E decreases with fiber radius and can be as much as 52% lower than that of the corresponding bulk material. Poisson's ratio ν of the polymer comprising these nanofibers was found to decrease from a value of 0.3 to 0.1 with decreasing fiber radius. Our findings also indicate that a small but finite stress exists on the simulated nanofibers prior to elongation, attributable to surface tension. When strained uniaxially up to a tensile strain of ε=0.2 over the range of strain rates and temperatures considered, the nanofibers exhibit a yield stress σ_y between 40 and 72 MPa,

which is not strongly dependent on fiber radius; this yield stress is approximately half that of the same polyethylene simulated in the amorphous bulk.

Another focus of this thesis was to study the interfiber interactions between these nanofibers. For this purpose, we employ similar MD simulations and energy minimization, or molecular statics (MS). MD simulations show that fibers aligned parallel and within 9 nm of one another experience a significant force of attraction. These fibers tend to coalesce on a very short time scale, even below T_g. In contrast, our MS simulations suggest an interfiber interaction that transitions from an attractive to a repulsive force at a separation distance of 6 nm. The results of either simulation approach can be used to obtain a quantitative, closed-form relation describing fiber-fiber interactions. However, the predicted form of interaction is quite different for the two approaches. This difference can be understood in terms of differences in molecular mobility within and between fibers, and whether such mobility is appreciable or not. The results of these simulations are used to interpret experimental observations for electrospun polymer nanofiber mats. These findings highlight the role of temperature and kinetically accessible timescales in predicting interface-dominated interactions at polymer fiber surfaces, and prompt further experiments and simulations to confirm these effects in the properties of nonwoven mats comprising such fibers.

Finally, we use a novel Monte Carlo (MC) technique which can incorporate since nanofiber properties and interfiber interaction. In this model, the nonwoven network is composed of several fibers that are represented by linked, cylindrical segments. Fiber flexibility is obtained by varying the material and geometrical properties of the segments in stretching, bending and twisting. We are able to create networks with different fiber orientations and with volume fractions of 5-25%, comparable to those of real electrospun nonwovens.

Acknowledgements

First, I am truly thankful to my supervisors, Professor Greg Rutledge and Professor Krystyn Van Vliet, for the guidance, advice and support from the initial to the final level. I learned a lot from them and I truly appreciate their efforts to make this thesis a first-rate research and to make me a better scientist, I hope I was able to live up to their expectations. I would also like to thank my thesis committee members; Professor Sidney Yip and Dr. Simona Socrate, for their input and constructive criticisms that helped guide my research.

I have been fortunate enough to share my life at MIT with the members of two research groups, who have been helpful in a variety of ways. Though I cannot possibly list them all, I'd like to give special thanks to members of Rutledge group; Dr. Joe Lowery for his friendship and answering my endless questions about electrospinning, Chia-ling Pai for helping me out with my attempts to do experiments and providing me with everything I needed during the process, Dr. Fred Bernardin and Predrag Djuranovic for all the great conversations about anything and everything, and other past and present members, Dr. Jian Yu, Dr. Minglin Ma, Dr. Erik Allen, Dr. Miguel Amat, Dr. Jung Ah Lee, Dr. Sanghun Lee, Peng Yi and Dr. Ying Yang. Within the Van Vliet group, I absolutely need to thank Dr. Catherine Tweedie, Emily Walton, Irene Chen, Hansohl Cho, Ilke Kalcioglu, Ranjani Krishnan, John Maloney, Dr. Karen Stewart, Dr. Meng Qu and Adam Zeiger.

I would like to thank my first MIT roommate and my great friend, Grace Zheng, for supporting me and being with me through all the good times and bad times at MIT and I wish her the best at her own Ph.D.

A huge thank you goes to my dear friends Cem Biro and Dr. Tugba Ozal, who were with me all the way even though they were an ocean away. I cannot thank enough to Cem for all the moral support as well as material support (including Turkish books/CDs) and phone calls to remind me that he was there for me. I send my special thanks to Tugba, for helping me get through all these years and for being a special friend.

This thesis would not have been possible without the support of those people who love me and support me no matter what.

I am indebted to my dear friend, Dr. Ayse Asatekin, who has been a truly great friend and colleague. We have shared so many things together and she has always been there for me with her beautiful smile and loving heart. I'm so proud to be her friend and know that she'll be very successful in anything she'll do.

I would also like to thank my brother Gediz Curgul, my sister-in-law Hande Curgul and my little niece Duru, who joined us 2.5 years ago and brought joy to our lives. I have always felt and really appreciated their love and support.

My dear husband, Steven Buell, deserves special thanks for providing me all the love, motivation and encouragement and just about everything else I needed throughout these years. He is my best friend and my biggest supporter and I feel very lucky to have met him. I certainly couldn't do this without him.

My deepest thank you goes to my parents, Ismail and Semra Curgul, who have always supported me and provided me with everything I needed in life. I cannot thank them enough for everything that they've done for me and for raising me up to be the person I am.

This thesis is dedicated to my dad who always believed in me: I hope I made you proud.

Table of Contents

List of Figures

List of Tables

CHAPTER 1: SCOPE AND OVERVIEW

1.1. Scope

Electrospinning is a promising approach for development and commercialization of nanofibers and nonwoven fabrics comprising such nanofibers. Because of the combined characteristics of small fiber diameter (50-500 nm), large surface area (10-100 m^2/g), and interfibrillar distances that are small relative to fiber diameter, these materials have been advocated for use in filtration media [1], tissue engineering [2], biomedical applications [3], composites [4], and other industrial applications [5]. Of fundamental necessity for many of these applications is an understanding of the determinants not only of fiber diameter, but also of the junctions between the fibers constituting the interconnected pore structure and the fiber-fiber interactions. Challenges in facile and repeatable measurement and characterization of the properties of the fibers and nonwoven fabrics have presented bottlenecks to the efficient development of the technology.

The aims of this project are to develop the necessary modeling tools to quantify and describe the structural, thermal and mechanical properties of polymer nanofibers and to investigate the interactions between these fiber pairs. These models developed herein provide a means to evaluate the fiber properties as a function of fiber diameter and thereby help us understand the origin of transition from the regime of *bulk-like* behavior to that of *nanomaterial* behavior. They also allow estimation and prediction of properties that may be impractical to measure experimentally due to the limitations of instrument capabilities or availability of material samples.

We also aim at laying the groundwork for the modeling of nonwoven mats which incorporates single nanofiber properties and interfiber interactions. This groundwork allows us to establish a quantitative connection between nanoscale properties and nonwoven mat properties and permit parametric studies for specification of materials criteria for selected design objectives. With these capabilities, the research scientist and engineer would be better equipped to exploit opportunities in this developing field.

1.2. Overview

Chapter 2 is a general overview of electrospinning and electrospun materials. This chapter begins with the historical development of the electrospinning technology, and gives background information of the electrospinning process. This section also includes the experimental and modeling studies of polymer nanofibers and nonwoven materials. Finally, Chapter 2 introduces the motivation for the detailed computational and modeling studies of these systems.

Chapter 3 focuses on the results of molecular dynamics simulations to model and characterize polyethylene nanofibers. In this chapter, these nanofibers are analyzed for signatures of emergent behavior in their structural and thermal properties as a function of fiber radius. The effect of the free surface on structural properties, such as molecular orientation and conformations, is demonstrated. Glass transition temperature depression with decreasing fiber diameter is investigated, and a layer model is derived to explain this physical phenomenon.

Chapter 4 focuses on the mechanical properties of the single, free standing amorphous polyethylene nanofibers. In this chapter, elastic and plastic deformations of these nanofibers as a function of fiber diameter and temperature are explored. A layer model that explains the trends observed in the simulation data is introduced. The length scales from two layer models are compared and physical insight to this comparison is given in terms of cooperatively rearranging regions and dynamics of polymers.

Chapter 5 introduces the derivation of an interfiber interaction potential using two different methods: molecular dynamics and molecular statics simulations. The results from each method are discussed in terms of the physical phenomena and corresponding experimental conditions under which these results are valid.

Chapter 6 focuses on constructing a preliminary framework to model the nonwoven mats. A novel Monte Carlo method which can incorporate nanoscale properties (i.e., individual

nanofiber properties and interfiber interactions) is presented. The important dimensionless parameters of the model are identified and an example parametric analysis is given to explore the model. Fiber orientation distributions from image analysis of real electrospun mats and model generated nonwoven mats are also given and compared in this chapter.

Finally, Chapter 7 includes a summary of conclusions, an outlook on the implications of this research, and identification of future research opportunities.

REFERENCES

[1] Barhate R.S.; Ramakrishna S. *Journal of Membrane Science* **2007**, *296*, 1-8.

[2] Martins A.; Araujo J.V.; Reis R.L.; Neves N.M. *Nanomedicine* **2007**, *2*, 929-942.

[3] Liang D.; Hsiao B.; Chu B. *Advanced drug delivery reviews* **2007**, *59*, 1392-1412.

[4] Yeo L.Y.; Friend J.R. *Journal of experimental nanoscience* **2006**, *1*, 177-209.

[5] Burger C.; Hsiao B.; Chu B. *Annual Review of Materials Research* **2006**, *36*, 333-368.

CHAPTER 2: BACKGROUND

2.1 Electrospinning: Introduction and historic development

Zhou et al. recently reviewed several methods for forming nanofibers, including bicomponent spinning, melt-blowing, flash spinning and electrospinning [1]. Of these, electrospinning has been shown to be the most robust, and has been used to process a wide range of different chemistries. Compared to bottom-up methods, this top-down approach to nanofiber formation offers the greatest promise for large scale production [2], and has been actively researched by numerous research groups.

Electrospinning is a novel and efficient fabrication process that can be utilized to assemble fibrous polymer mats composed of fiber diameters ranging from several microns down to fibers of diameter lower than 100 nm. Although the term "electrospinning", derive from "electrostatic spinning", was used relatively recently, its fundamental idea dates back more than 100 years earlier. Electrospinning first appeared in the patent literature in 1902 [3].

In 1960s, fundamental studies on the jet forming process were initiated by Taylor [4]. In 1969, Taylor studied the shape of the polymer droplet produced at the tip of the needle when an electric field is applied and showed that it is a cone and the jets are ejected from the vertices of the cone [4]. This conical shape of the jet was later referred to by other researchers as the "Taylor cone". In 1971, Baumgarten reported the electrospinning of acrylic microfibers of diameters ranging from 500 to 1100 nm [5]. Baumgarten determined the spinnability limits of a polyacrylonitrile/dimethylformamide (PAN/DMF) solution, and observed a specific dependence of fiber diameter on the viscosity of the solution. He showed that the diameter of the jet reached a minimum value after an initial increase in the applied field and then became larger with increasing electric fields. Larrondo and Mandley produced polyethylene and polypropylene fibers from the melt, which were found to be relatively larger in diameter than solvent-spun fiber [6-7]. In 1987, Hayati et al. studied the effects of electric field, experimental conditions, and the

factors affecting the fiber stability and atomization [8]. They concluded that liquid conductivity plays a major role in the electrostatic disruption of liquid surfaces. Relatively stable jets were produced with semi conducting and insulating liquids, such as paraffinic oil. After a decade or so, research on nanofibers gained momentum due to the work of Doshi and Reneker [9]. Doshi and Reneker studied the characteristics of polyethylene oxide (PEO) nanofibers by varying the solution concentration and applied electric potential [9]. Jet diameters were measured as a function of distance from the apex of the cone, and they observed that the jet diameter decreases with the increase in the distance.

In recent years, the electrospinning process has regained more attention. This renewed research activity can be attributed in part to a surging interest in nanotechnology, as ultrafine fibers or fibrous structures of various polymers can be easily fabricated with this process. To date, approximately one hundred different polymers have been successfully spun into ultrafine fibers using this technique. Although electrospinning process has shown potential promising and has existed in the literature for quite a few decades, its understanding is still very limited. The properties of the fibers and nonwoven fabrics produced, as well as the means for characterizing these, have remained bottlenecks in the development of the technology, both for scale-up purposes and for quality control and reproducibility during fabrication.

2.2. Electrospinning: Fundamental aspects

A schematic diagram to interpret electrospinning of polymer nanofibers is shown in Figure 2.1. There are basically three components required to fulfill the process: a high voltage power supply, a spinneret (a metallic needle) and a collector (a grounded conductor). The spinneret is connected to a syringe pump; the solution can be fed through the spinneret at a constant and controllable rate. When a high voltage is applied, the pendant drop of polymer solution at the nozzle of the spinneret will become highly electrified. As a result, the drop will experience two major types of electrostatic forces: the electrostatic repulsion between the surface charges and the Coulombic force exerted

by the external electric field. Under the action of theses electrostatic interactions, the liquid drop will be distorted into a conical object, commonly known as the Taylor cone. Once the strength of the field surpassed a threshold value, the electrostatic forces can overcome the surface tension of the polymer solution and thus force the ejection of a liquid jet from the nozzle. This electrified jet then undergoes a stretching and whipping process, leading to the formation of a long and thin jet. As the liquid jet is continuously elongated and the solvent is evaporated, its diameter can be reduced from hundreds of micrometers to as small as tens of nanometers. Attracted by the grounded collector placed under the spinneret, the charged fiber is often deposited as a randomly oriented, nonwoven mat. Through appropriate modifications of the spinnerette, electric field, or collector, final products ranging from uniform nonwoven mats, to patterned membranes, to yarns, to well-aligned arrays of fibers have been demonstrated. Significantly, the process has been used in the production of submicron fibers for filters, composites, fuel cells, nanowires, catalyst supports, drug delivery devices, tissue scaffolds, and other applications.

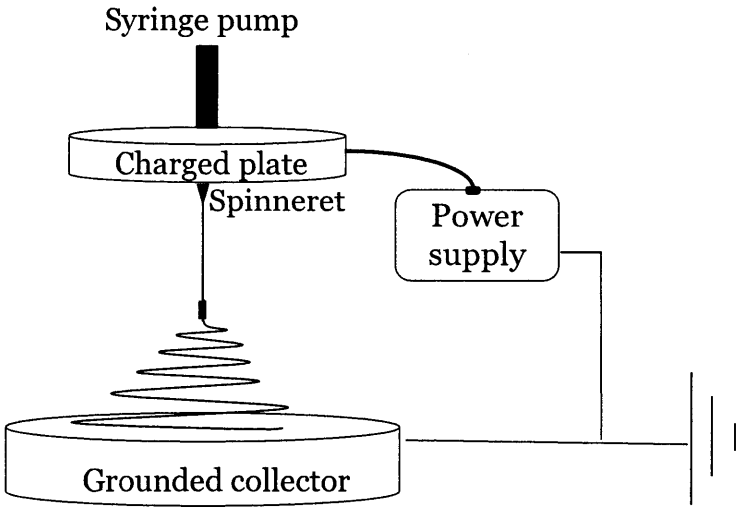

Figure 2.1 Diagram of electrospinning apparatus. Spinneret and collector electrodes provide applied electric field. The product is collected on the grounded collector, which may be stationary or moving.

2.3. Properties of single nanofibers

2.3.1. Experimental studies

By convention, a nanomaterial will exhibit at least one dimension that is reduced in length to < 100 nm, where 1 nm=10^{-9} m. Any emergent properties of the nanomaterial may then originate from three features: the reduced linear dimension L ("confinement-dominated materials"), the high surface area S ("surface-dominated materials") and, eventually a reduced dimension from d=3 (bulk material) to d=2,1,0 in thin films, nanofibers and nanoparticles, respectively ("dimensionality effects").

Effects of confinement on material behavior at the nanometer size scale have been a subject of considerable interest for years [10-13]. By confining polymer molecules to dimensions that are comparable to the different length scales characterizing the molecules, the motion of the molecules can be significantly different than in bulk. For example, the effect of confinement on the segmental motion of polymers has been studied using a variety of experimental geometries: interfaces in semicrystalline polymers [10], polymer solutions in porous glasses [11], polymers intercalated into the 2 nm gaps of layered compounds [12], polymer spheres with diameters of tens of nanometers [13], and thin polymer films. It has been shown that segmental mobility can be enhanced in very thin polymer films though the motion of entire chains is unchanged from that in bulk. In particular, the results obtained for freely standing polymer membranes are unique and remarkable, with very large reductions in the apparent glass transition temperature T_g and no corresponding enhancement of whole-chain motion for very thin films. Although there is no experimental data for a single polymer nanofiber, the DSC studies on the electrospun nonwoven poly(L-lactic acid) (PLLA) membrane showed that PLLA fibers have lower crystallinity, T_g and melting temperature T_m than semicrystalline PLLA resins [14]. Zong et al. attributed the decrease in T_g to the large surface to volume ratio of nanofibers, with air as the plasticizer. The T_g and T_m of the electrospun polyethylene terephthalate (PET) and polyethylene naphthalate (PEN) were measured to be significantly lower than the bulk material, which were attributed to the increase in the segmental mobility [15]. Poly(ethylene oxide) (PEO) fibers have shown a lower melting

temperature and heat of fusion than PEO powder, which is attributed to poor crystallinity of the electrospun fibers [16].

Experimental studies on the mechanical characterization of nanofibers have become an increasingly reported effort in recent years. Various attempts have been made to quantify the elastic properties of isolated polymer fibers of diameter $d < 1$ μm via direct experimental measurements [17-28]. Figure 2.2 shows Young's elastic modulus E vs. fiber diameter, which is plotted by using the data given in these studies [17-28].

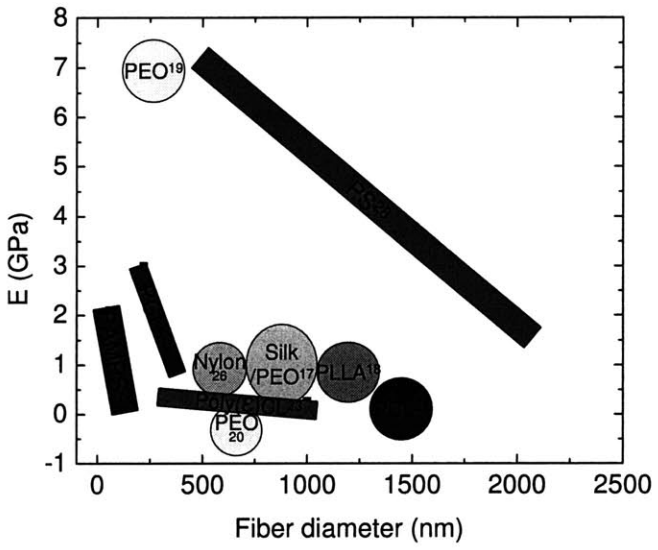

Figure 2.2 Young's modulus E vs. fiber diameter that summarizes the studies mentioned in the text [17-28]. The circles represent measurement of E for a single fiber diameter. The rectangles represent E measured at different fiber diameters.

Mechanical characterization techniques that have been developed to test individual polymer fibers include uniaxial tensile loading [18], as well as bending and indentation of individual fibers using atomic force microscopy (AFM) cantilevered probes to impose deformation [19]. For example, the effects of processing conditions on mechanical properties of electrospun poly(L-lactide) (PLLA) nanofibers with diameters of 610 nm and 890 nm were investigated via tensile testing [18]. Higher rotation rate of the

collection roller correlated with higher tensile Young's elastic modulus E and strength of the nanofibers, which was attributed to the ordered structure developed during the collection process. [18] Bellan et al. measured the Young's moduli of polyethylene oxide (PEO) fibers with diameters 80 nm < d < 450 nm using an atomic force microscopy (AFM) cantilevered probe to deflect the suspended fibers, and reported E in significant excess of that reported for bulk PEO [19]. The authors attributed this enhanced stiffness to the molecular orientation of PEO chains within the fibers [19]. Tensile testing of polycaprolactone (PCL) nanofibers with diameters 1.03 μm < d < 1.70 μm to the point of mechanical failure showed that fibers of smaller diameter exhibited higher fracture strength but lower ductility [21]. Mechanical properties of single electrospun nanofibers composed of PCL and poly(caprolactone-co-ethlyethylene phosphate) (PCLEEP) were also measured under uniaxial tension, indicating an increase in both stiffness and strength as the fiber diameter decreased from 5 μm to ~250 nm [22]. Chew et al. also found that E of these PCL nanofibers were at least twice that of PCL thin films of comparable thickness [22]. Recently, Wong et al. reported an abrupt increase in tensile strength and stiffness of these PCL fibers below fiber diameter of 1.4 μm, and attributed this to improved crystallinity and molecular orientation in fibers of smaller diameter [23]. Young's moduli of electrospun nylon-6 nanofibers were found to increase from 20 GPa to 80 GPa as the fiber diameter decreased from 120 nm to 70 nm [24]. In separate tensile studies on electrospun nylon-6,6 nanofibers, E was reported to increase threefold for fibers with diameters <500 nm [27]. No significant increase in degree of crystallinity or chain orientation accompanied this increase in E [27]. Using scaling arguments, these authors reasoned that this size-dependent stiffening effect was due to the confinement of a supramolecular structure, consisting of molecules with correlated orientation, comparable to the nanofiber diameter. Finally, the shear elastic modulus G of glassy electrospun polystyrene (PS) fibers of 410 nm < d < 4 μm was estimated using an AFM probe via shear modulation force spectroscopy of the fiber surface, and also reported to increase with decreasing fiber diameter [28]. This trend was attributed to molecular chain alignment frozen in during the electrospinning process. When functionalized clay was added to these PS nanofibers, G of the fibers was further increased, although the stiffening mechanism remains unclear [28]. Importantly, although these reports generally

indicate increasing elastic modulus and strength with decreasing fiber diameter, all of these fibers (with the exception of the PS fibers of Ref. 28) are also semicrystalline.

Mechanical properties of metallic and ceramic nanofibers have also been the subject of many studies [29-40]. Lee et. al. [29] have developed a modified three-point bending method for testing the mechanical properties of TiO_2 nanofibers for biomedical implants [29]. Khalil et al. [30] fabricated a nanocomposite using electrospun hydroxyapatite and nickel oxide. It was shown that the sintering behavior, toughness, and hardness of the resulting composites were significantly enhanced by the inclusion of NiO nanofibers [30]. Ostermayer et al. [31] have reported the V50 behavior of the first nylon-6 clay composite electrospun fibers using a fragment simulating a projectile. Lee et al. [32] have compared the elastic modulus of anatase nanofibers with carbon nanotube-nanofiber composites. A modified three-point bending test was carried out as described before using an AFM. The mean elastic modulus was found to be 75.6 and 156.9 GPa for the anatase and carbon nanotube-anatase nanocomposite, respectively [32]. Mechanical properties of conventional silica fibers of diameter < 1μm have been measured resonant frequency measurements [34, 35] and using direct measurement of force during controlled displacement of a compliant cantilevered probe within a scanning probe microscope [36]. Same method has been used to measure the stiffness and strength of carbon nanotubes, nanorods, as well as nanowires made of silicon carbide [37], gold [38], silver [39] and manganese oxide [40] among others.

An alternative way to characterize mechanical properties of the nanofiber is molecular scale simulations. This approach has the potential to provide quantitatively accurate results on the nanoscale. Most results of molecular simulations on nanoscale matters have been focused on nanotubes, metal nanowires, or nanoparticles [41]. To our knowledge, computational studies and predictions of the mechanical properties of polymer nanofibers fabricated from electrospinning have not been reported previous to this thesis work. Molecular scale simulations can also help to elucidate several different mechanical phenomena that may govern the emergent properties of electrospun fibers. Yarin et al. [42] reported failure modes of electrospun polymer nanofibers of diameters 80 nm < d < 400 nm and lengths greater than several centimeters. They observed multiple necking

formations at a high rate of stretching of the nanofibers. The results clearly distinguish nanofibers from macroscopic polymer specimens, for which multiple necking is seldom reported as a failure mode. The authors attributed this difference to the fact that macroscopic specimens cannot accommodate more than a single neck, while nanofibers can but did not provide a physical explanation [42].

Geometric properties of nanofibers such as fiber diameter, diameter distribution, and fiber morphology (i.e., cross-section shape and surface roughness) can be characterized using scanning electron microscope (SEM), field emission scanning electron microscopy (FESEM), transmission electron microscopy (TEM) and atomic force microscopy (AFM). [43-46] AFM imaging can be used to characterize the roughness of fibers. The roughness value is the arithmetic average of the deviations of height from the central horizontal plane given in terms of millivolts of measured current [43]. Another approach for geometrical characterization of nanofibers can be to make use of conventional molecular scale simulation methods such as molecular dynamics and Monte Carlo. When these methods are applied to atomistically detailed models of the materials, such tools provide a rigorous approach to study fiber properties on the length scale of molecular dimensions. The advantage of molecular simulations over experiments is that variation in polymer structure on the scale of 1-10 nm (comparable to intermolecular interaction distances) can be efficiently simulated. In contrast, it is very difficult to acquire such accuracy with current experimental methods at this length scale.

The configuration of macromolecules in a nanofiber can be characterized by optical birefringence [50-62], wide-angle X-ray diffraction (WAXD) and small-angle X-ray scattering (SAXC) [39]. Fong and Reneker [53] studied the birefringence of the styrene-butadiene-styrene (SBS) triblock copolymer nanofibers with diameters around 100 nm under an optical microscope. The occurrence of birefringence reflects the molecular orientation. Jaeger et al. [47] visualized chain packing in electrospun PEO by AFM. These authors found that at the molecular level, the electrospun PEO fibers possessed a highly ordered surface layer. Molecular dynamics simulations can also provide detailed information about the configuration of macromolecules in a nanofiber, as the simulation

output can be parameterized in terms of order parameter, chain shape (e.g. acylindricity, asphericity) and other relevant metrics.

2.3.2. Modeling and simulation studies

Due to the extremely small diameter and other problems that are mentioned above, experimental characterization of the structural, thermal and mechanical properties of a single nanofiber is difficult with the current techniques. So, molecular scale simulations provide an alternative means to understand the macroscopic properties of a nanofiber. Molecular scale simulation of a system is aimed to determine macroscopic properties using a microscopic model which has been constructed to describe the main interactions between the particles which comprise the system. Such an approach has been widely used in polymer science and engineering to rationalize the molecular structure, function and interaction of the polymer material. As such simulations are based on atoms and molecules, many of the thermodynamic, structural and transport properties of the material can be quantified via well designed simulations.

Two of the most commonly used molecular simulation techniques include the purely stochastic Monte Carlo (MC) method, which randomly samples the configurational space and which generally leads to static properties and the deterministic molecular dynamics (MD) method, which produces trajectories in the configurational space and leads to both static and dynamic properties.

In a molecular dynamics simulation, the configurational space is sampled by simultaneous integration of the Newton's second law for all the atoms i of the system:

$$m_i \frac{d^2 r_i(t)}{dt^2} = F_i(t), i = 1,...N \tag{2.1}$$

where m_i is the mass of atom i, $r_i(t)$ is its position at time t, and $F_i(t)$ is the total force exerted on the atom i by the other N-1 atoms and external forces at time t. For each atom

i, the force F_i is calculated at time t as the negative gradient of the intermolecular potential function, i.e.,

$$F_i(t) = -\frac{dU(r_1, r_2, ..., r_n)}{dr_i} = -\nabla_i U(r_1, r_2, ..., r_n) \tag{2.2}$$

The time step used in numerical integration is the order of 1 fs (1 fs = 1 femtosecond = 10^{-15} s). The results of the calculation are the trajectories of the N atoms obtained at a set of n t_k values with $t_k = t_{k-1} + \Delta t$.

Molecular dynamics has been used widely for understanding the chemical and physical properties of various polymers on various length and time scales. Several levels of detail are possible while still maintaining the chemical identity of the chain. The first, an explicit atom (EA) model, treats all atoms including hydrogen as interaction sites (Figure 2.3). The second, a united atom (UA) model, reduces computation time by grouping each carbon with its bonded hydrogen atoms to form a united atom (Figure 2.3). The third, a coarse-grained (CG) model, reduces computation time even further by grouping a few united atoms, monomers, or even the whole chain as a single CG bead. There are some instances where EA modeling is required, for example, in the calculation of properties such as the vibrational density of states, methyl group rotation, and elastic constants of crystalline polymers. The UA representation is widely used because it is computationally efficient while providing results in reasonable agreement with available experimental data. For the same reason, CG models are becoming more common.

Various simulation techniques have been applied to investigate the confinement of polymeric systems in one or two dimensions. First, lattice Monte Carlo (MC) simulations of a melt-vacuum interface were performed by Madden using a film adsorbed on a solid surface [54] The film was shown to have a central region with bulk-like characteristics, sandwiched between two interfacial regions. The structural features at the interface were found not to scale with molecular weight.

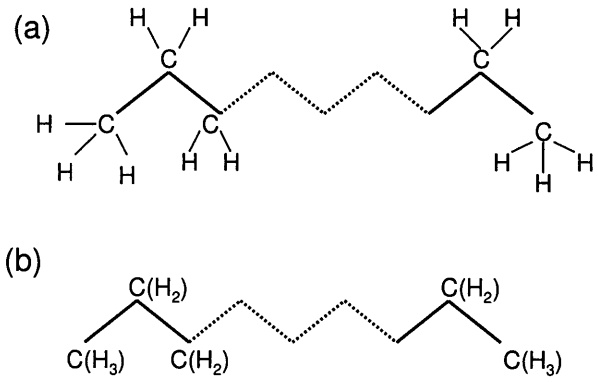

Figure 2.3 (a) Schematic representation of the explicit atom model for polyethylene. (b) Schematic representation of the united atom model for polyethylene. The hydrogen atoms are grouped with the carbon to form a united atom.

Using off-lattice atomistic simulation, Mansfield et al. identified regions of thickness 1.0 nm at the surfaces of a thin film of atactic polypropylene of thickness 6.1 nm, in which local structural features were different from the bulk [55]. Again, no dependence of structural properties on the molecular weight (MW) was found in the interfacial region, for the MW range 1068-3246 g/mol. Short time scale dynamics of the atactic polypropylene-vacuum interface were then studied using molecular dynamics (MD) simulations [56]. While the structural features were in agreement with molecular mechanics results [55], enhancements in the mean-squared displacement of the atoms relative to the chain center of mass were observed in the surface region, compared to the bulk polymer. Harris et al. [57] observed chain end segregation and flattening of chains at the liquid-vacuum interface in MD simulations of thin films comprising short-chain alkanes, and off-lattice MC simulations of thin films showed that chains exhibit predominantly bulk-like characteristics at the film center and are more collapsed at the vacuum surface [58]. MD simulations of thin films of poly-(1,4-cis-butadiene) showed that the sharp onset of orientation of the backbone bonds corresponds with the drop in mass density from its bulk value [59]. A thicker surface layer was found in MD simulations of amorphous polyethylene (PE) than in thin films of poly-(1, 4-cis-butadiene), which was attributed to the stiffer nature of the PE chains [48]. A dynamic MC simulation method on a high coordination lattice was subsequently introduced by

Mattice et al. [61], and used to determine equilibrium and dynamic properties of amorphous PE thin films [62, 63]. It was observed that the segregation of chain ends contributed to increased mobility at the free surface of PE thin films [64]. The decrease in radius of gyration of chains was more significant for free-standing PE thin films as the molecular weight increased [65].

While there have been numerous studies of nanometer-thick films by simulation, to our knowledge, only two studies of polymer nanofibers have been reported prior to this thesis research [66, 67]. Both of these reports employed the coarse-grained MC method on a high coordination lattice that was used previously for thin films [61-63] and nanoparticles [68]. Two PE nanofibers with diameters 5.6 and 7.6 nm were simulated [66] on a high coordination lattice, with interactions between occupied lattice sites designed to account for both short and long range interactions. It was found that the density profiles of these nanofibers could be fitted to a hyperbolic tangent profile, and there was significant segregation of end beads to the surface. Molecules were found to orient preferentially parallel to the surface, with the largest principal axis parallel to the surface. Diffusion coefficients of 5.6×10^{-6} nm^2/Monte Carlo step in the narrower nanofiber and 4.4×10^{-6} nm^2/Monte Carlo step for the thicker nanofiber were calculated for 1-D diffusion parallel to the fiber axis [67]. The mobility of the chains at the surface of the PE nanofiber was found to be greater than that of the chains at the center of the nanofiber. The overall chain mobility was found to increase as the fiber size decreased. Similar trends were observed for the free-standing thin films [63], implying that the curvature present in the fibers does not have a significant effect on the diffusion characteristics of the chain segments. The increased mobility in both the nanofibers and in the free-standing thin films was attributed to a region of lower mass density at the surface.

2.4. Modeling and characterization of the nonwoven mat

2.4.1. Experimental studies

Nanostructured fibrous materials have been made more readily available in large part owing to recent advances in electrospinning. The nonwoven structure has unique features, including interconnected pores and a very large surface-to-volume ratio, which enable nanofibrous scaffolds to have many biomedical and industrial applications. The chemical composition of the electrospun nonwoven network can be adjusted through the use of different polymers, polymer blends and nanocomposites made of organic or inorganic materials. In addition to the control of material composition, the processing flexibility in changing physical parameters and structures, such as fiber diameter, porosity, texture, and pattern formation, offers the capability to design electrospun scaffolds that can meet the demands of numerous practical applications. Here, the term nonwoven will be used interchangeably with the more explicit term "nonwoven material comprising fibers".

Geometrical properties of nonwoven mat such as fiber orientation can be characterized using SEM, TEM, FESEM and mercury porosimetry [46, 47]. Another geometric parameter is porosity. The porosity and pore size of nanofiber membranes are important for applications of filtration, tissue template, protective clothing and other potential applications [45, 69, 70]. The pore size measurement can be conducted by, for example, a capillary flow porometer [45, 69]. Schreuder-Gibson et. al. compared the pore sizes of membranes electrospun from Nylon 6,6, FBI (polybenzimidazole), and two polyurethanes, Estane® and Pellethane®. They found that Nylon 6,6 could be electrospun into a very fine membrane with extremely small pore throat sizes (with a mean flow pore diameter of 0.12 μm) which were much smaller than the average fiber diameters. FBI also exhibited pore sizes (0.20 μm) smaller than the electrospun fiber sizes. However Estane® and Pellethane® exhibited mean pore sizes which were significantly higher, with average flow pore diameters of 0.76 and 2.6 μm, respectively [69].

Surface chemical properties of nonwoven mats can be determined by X-ray photoelectron spectroscopy (XPS), water contact angle measurement, and FTIR-ATR analyses. Desimone and co-workers [71] measured the atomic percentage of fluorine in poly(methyl methacrylate) (PMMA)- tetrahydroperfluorooctyl acrylate (TAN) blend. It was shown that the atomic percentage of fluorine in the surface region of the electrospun fibers was about double the atomic percentage in a bulk polymer. Surface chemical properties of a nanofiber can also be evaluated by its hydrophilicity, which can be measured by the water contact angle analysis of the nanofiber membrane surface. Ma et.al. [72] has reported contact angle measurements on block copolymer poly(styrene-b-dimethylsiloxane) fibers with diameters in the range 150-400 nm. The measurements showed that the nonwoven fibrous mats are superhydrophobic, with a contact angle of 163^{o}.

Air and water transport properties of electrospun fibrous mats have been measured using an apparatus called dynamic moisture vapor permeation cell (DMPC) [73]. This device has been designed to measure both the moisture vapor transport and the air permeability (convective gas flow) of continuous films, fabrics, coated textiles and open foams and battings. Schreuder-Gibson and Gibson compared electrospun nanofibrous nonwoven of a thermoplastic polyurethane with corresponding meltblown nonwovens. Average pore size of the electrospun nonwovens was 4-100 times smaller than that of the meltblown nonwovens, resulting in an increase in air flow resistance by as much as 156 times. However, no significant difference has been found for the "breathability", or moisture vapor diffusion resistances of the two nonwovens. [74]. Crosslinking the fibers of the electrospun membrane significantly decreases liquid transport through the membrane.

Electrical transport properties of electrospun nanofibers were investigated by some researchers [75, 76]. Norris et al. measured the conductivity of electrospun nonwoven ultra-fine fiber mat of polyaniline doped with camphorsulfonic acid blended with PEO. As the nonwoven mat was highly porous and the "fill factor" of the fibers were less than that of a cast film, the measured conductivity seemed to be lower than that of the bulk

[75]. Wang et al. measured the conductivities of polyacrylonitrile (PAN) nanofibers before and after carbonization, using a digital electrometer with two neighboring contacts of 4 mm distance. The electrospinning was conducted carefully and briefly so that there was only one continuous fiber deposited across the two neighboring contacts. The PAN fiber (before carbonization) exhibited resistance which was beyond the upper limit of the electrometer, whereas the graphitization of the PAN nanofiber led to a sharp increase in conductivity [76].

The tensile properties of nanofibers and membranes can be evaluated with fiber membranes, bundles, aligned fibers, and single filaments. Because of the ease of sample preparation, fiber membranes have been mainly used as the samples for tensile tests. Although many tensile tests with fiber membranes have been presented so far in the literature, the validity of tensile tests with membranes for studying the tensile properties of electrospun fibers has not been made clear through explicit validation. The following polymer nonwoven mats have been analyzed under tensile loading: poly(D,L-lactide-co-glycolide) (PLGA) [44], poly(epsilon-caprolactone) (PCL) [77], poly(vinyl chloride) (PVC) [78], silk [79], blends of collagen and PEO [80], and blends of PLGA and poly(lactide-*co*-ethylene glycol) block copolymers. [81]. Aligned nonwoven mats have also been tested under tensile loading with PLA and were found to have different properties in different directions [82].

2.4.2. Modeling and simulation studies

Abdel-Ghani and Davies [83] proposed a model to simulate the nonwoven fabric geometry by assuming that the nonwoven fabric can be decomposed into layers, one above another (Figure 2.4b). Each layer was considered as a random network of fibers (Figure 2.4a). The areas formed between intersecting or overlapping fibers in a particular layer constituted the pores in the media. A Monte Carlo method was used to produce random line networks to represent a layer. Methods of describing the line network were reviewed in their work. A variation in diameters of fibers was considered in the simulation to represent practical fiber materials. There are several other studies that used

a nonwoven generation technique similar to that of Abdel-Ghani et al. [84-91]. These studies mainly aimed to characterize the permeability of nonwoven media. Termonia et al. [92] proposed a model in which a fibrous sheet is viewed as a pile of overlapping layers. Each layer was represented by a network of ribbon-like fiber strands connected on a two-dimensional x-y square lattice. Such an approach neglected the possibility of interweaving of the fibers among layers. The permeability of the sheet to diffusional flow was studied by a Monte Carlo process. In that process, the sheet was put in contact with a large external bath of small particles which diffuse through the structure by hopping between nearest-neighbor lattice sites [92].

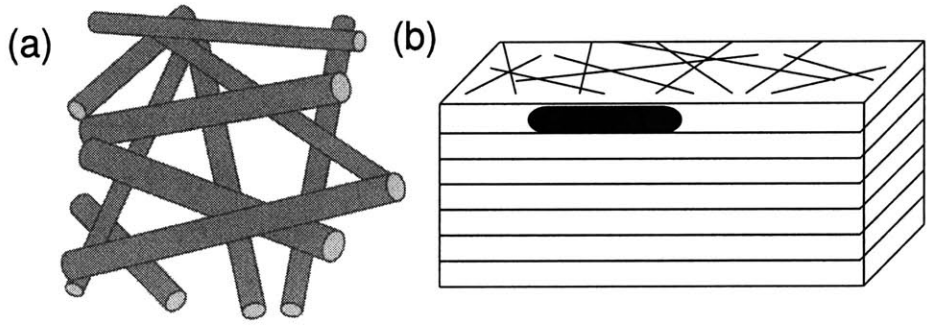

Figure 2.4 (a) Top-down perspective of a 2-D single layer of that consists of random network of fibers. (b) The nonwoven fabric can be decomposed into such layers (as shown in part a). Here, the thickness of each layer is equal to fiber diameter. (Black lines on top represent the random network of fibers)

Other previous approaches to modeling porous and fibrous media have focused exclusively on the pore interconnectivity (for porous media used, e.g., in catalysis or sorption studies) or the fiber arrangement (for fibrous media used, e.g., in mechanical studies). Typical of the former is the Dual Site Bond Model (DSBM) of Mayagoitia et al. [93-96], in which the porous material is represented as an idealized network of interconnected "sites" (the pore bodies) and "bonds" (throats and channels). The sites and bonds have their own size distributions. In general, size correlation arises owing to a natural constraint of entity size, which states: the size of each bond must be smaller than, or at most equal to, the size of the two sites that it connects. This statement is referred to as the Construction Principle. Monte Carlo methods have been used to generate

stochastic networks of such sites and bonds and to demonstrate changes in properties with porous network topology [97]. While distributions in both size and connectivity of sites and bonds are considered, the pore network does not appear to mimic accurately the shape anisotropy and pore network of connectivity of fibrous materials. A variant, the Corrugated Pore Structure model [98-99] was used to simulate capillary condensation-evaporation hysteresis. In this model, the pore structure was envisaged to be composed of a statistically large number N of independent (nonintersected) corrugated pores. A corrugated pore was assumed to be made of a series of interconnected cylindrical elements (pore segments) of equal length with randomly distributed diameters of mesopore size. A function, which was called "pore segment number intrinsic probability density function" was defined according to which pore segment diameter were randomly distributed. Given the type of the pore geometry, the respective pore volume and surface area distributions can be calculated. Each corrugated pore was assumed to be open at both ends and physically entered at some point on the external surface of an imaginary porous particle and exited at another point while along its course through the particle.

By contrast, fibrous networks are more commonly modeled as arrangements of rigid geometric objects, with attention paid to the contacts or interaction between these objects. In networks of rigid rods, the fiber length, width, linear density, porosity and areal density are characteristic of the network [100]. The "connected spheres" model proposed by Yamamoto et al. [101-103] to study dynamic simulation of rigid and flexible fibers in a flow field offers a step in the direction of non-rigid, interacting fibers. Fibers were represented as spheres that were lined up and bonded to each neighbor. Each pair of bonded spheres could stretch, bend and twist, by changing bond distance, bond angle, and torsion angle between spheres, respectively. The strength of bonding, or flexibility of the fiber model, was defined by three parameters of stretching, bending and twisting constants. By altering these parameters, the property of the fiber model could be changed to be rigid or flexible. The motion of a fiber was determined by solving the translational and rotational equations of motion for individual spheres under the hydrodynamic force and torque exerting on it. Another particle-level simulation method, that was similar to Yamamoto et al., was proposed by Ross and Klingenberg [104, 105]. This model was

employed to study the dynamics of suspensions of rigid and flexible fibers. Fibers were modeled as chains of prolate spheroids connected through ball and socket joints. The motion of a fiber was determined by solving the translational and rotational equations of motion for each spheroid. Different than Yamamoto, their model eliminated the need for iterative constraints to maintain fiber connectivity. Melrose and Ning [106] developed a numerical method for simulating mechanical behavior of flexible fibers. A circular crossed fiber was represented by a number of cylindrical segments linked by a spring dash-pot system. Computer simulations have been conducted to verify the model with elastic theory and agreements have been found between the simulation results and the theory for beam deflection under static loads, vibrating cantilevers, and dynamics of helical shaped fibers.

The mechanical performance of nonwoven mats is of interest in applications such as semi-permeable membranes, filters, protective clothing, and tissue engineering. For instance, the nanofiber scaffold template should be designed to be structurally biocompatible with the host tissue. This will be possible when the structure-property relationship of the scaffolds has been clearly understood. There are also challenges in incorporating the mechanical characterization into the modeling of the nonwoven mat. These include the determination of fiber orientation distributions in the nonwoven mats, the measurement of the coefficient of friction of the nanofibers, and the specification of the condition under which the fiber slippage occurs. Simulation of the mechanical properties of common textile nonwoven fabrics have been carried out mainly using finite element approach [107-112]. Dzenis and Wu [113] proposed a micromechanics model for the elasticity of planar fiber networks. The fiber network was created by random deposition of linearly elastic straight rods within a region. The rods were bonded rigidly at contacts. Under external in-plane loading, the fiber network deformation consisted of fiber bending, elongation and contraction. An effective constitutive relation for fiber network was developed by averaging the strain energy dissipated by all possible fiber deformations in all directions. Numerical calculations were performed to analyze the effects of fiber aspect ratio and fiber concentration on the effective stiffness of the planar random fiber network. Termonia et al. [114] used a discrete lattice model to study the

factors controlling the bending stiffness of nonwoven fabrics and found that nonwovens with a three-dimensional fiber orientation distribution have a much lower bending stiffness than those with a planar distribution.

REFERENCES

[1] Zhou F.; Gong R. *Polymer International* **2008**, *57*, 837-845.

[2] Dzenis Y., *Science* **2004**, *304*, 1917-1919.

[3] Morton W.J., US Patent 705,691, **1902**.

[4] Taylor G.I. *Proc. Roy. Soc. London* **1969**, *A313*, 453.

[5] Baumgarten PK. *J. Colloid Interface Sci.* **1971**, 36, 71.

[6] Larrondo L.; Mandley R. *J. Polym. Sci: Polymer Physics* **1981**, 909.

[7] Larrondo L.; Mandley R. *J. Polym. Sci: Polymer Physics* **1981**, 921.

[8] Hayati I.; Bailey A.I.; Tadros T.F. *J Colloid Interface Sci.* **1987**, *117*, 205.

[9] Doshi J.; Reneker D.H. *J Electrostatics* **1995**, *35*, 151.

[10] Schick C.; Donth E. *Pysica Scripta* **1991**, *43*, 423-429.

[11] Park J.Y.; McKenna G.B. *Physical Review B* **2000**, *61*, 6667-6676.

[12] Anastasiadis S.H.; Karatasos K.; Vlachos G.; Manias E.; Giannelis E.P. *Phys. Rev. Letters* **2000**, *84*, 915-918.

[13] Sasaki T.; Shimizu A.; Mourey T.H.; Thurau C.T.; Ediger M.D. *J. Chem. Phys.* **2003**, *119*, 8730-8735.

[14] Zong X.H.; Kim K.; Fang D.; Ran S.; Hsiao B.S.; Chu B. *Polymer* **2002**, *43*, 4403-4412.

[15] Kim J.S.; Lee D.S. *Polymer Journal* **2000**, *32*, 616-618.

[16] Deitzel J.M.; Kleinmeyer J.D.; Hirvonen J.K.; Beck Tan N.C. *Polymer* **2001**, *42*, 8163-8170.

[17] Wang M.; Jin H.J.; Kaplan D.L.; Rutledge G.C. *Macromolecules* **2004**, *37*, 6856-6864.

[18] Inai R.; Kotaki M.; Ramakrishna S. *Nanotechnology* **2005**, *16*, 208-213.

[19] Bellan L.M.; Kameoka J.; Craighead H.G. *Nanotechnology* **2005**, *16*, 1095-1099.

[20] Tan E.P.S.; Goh C.N.; Sow C.H.; Lim C.T. *Applied Physics Lett.* **2005**, *86*, 073115(1-3).

[21] Tan E.P.S.; Ng S.Y.; Lim C.T. *Biomaterials* **2005**, *26*, 1453-1456.

[22] Chew S.Y.; Hufnagel T.C.; Lim C.T.; Leong K.W. *Nanotechnology* **2006**, *17*, 3880-3891.

[23] Wong S.C.; Baji A.; Leng S. *Polymer* **2008**, *49*, 4713-4722.

[24] Li L.; Bellan L.M.; Craighead H.G.; Frey M.W. *Polymer* **2006**, *47*, 6208-6217.

[25] Shin M.K.; Kim S.I.; Kim S.J.; Kim S.K.; Lee H.; Spinks G.M. *Applied Physics Lett.* **2006**, *89*, 231929(1-3).

[26] Zussman E.; Burman M.; Yarin A.L.; Khalfin R.; Cohen Y. *J. of Poly. Sci. B Poly. Phys.* **2006**, *44*, 1482-1489.

[27] Arinstein A.; Burman M.; Gendelman O.; Zussman E. *Nature Nanotechnology* **2007**, *2*, 59-62.

[28] Ji Y.; Li B.; Ge S.; Sokolov J.C.; Rafailovich M.H. *Langmuir* **2006**, *22*, 1321-1328.

[29] Lee S.; Tekmen C.; Sigmund W.M. *Mater. Sci. Eng. A* **2005**, *398*, 77.

[30] Khalil K.; Kim H.Y.; Kim S.W.; Kim K.W. *Int. J. Appl. Ceram. Tech.* **2007**, *4*, 30.

[31] Ostermayer D.; Beyer F.L.; Dehmer P.G.; Klusewitze M.A. *Tech. Doc. Rep.* **2001**, 2605.

[32] Lee Y.S.; Wetzel E.D.; Egres R.G.; Wagner N.J. *Army Sciences Conf.* Orlando, **2002**.

[33] Ramaseshan R.; Sundarrajan S.; Jose R.; Ramakrishna S. *App. Phys. Rev.* **2007**, *102*, 111101.

[34] Wang Z.L.; Gao R.P.; Poncharal W.A.; Heer D.; Dai Z.R.; Pan Z.W. *Mater. Sci. Eng. C* **2001**, *16*, 3.

[35] Dikin D.A.; Chen X.; Ding W.; Wagner G.; Ruoff G.S. *J. Appl. Phys.* **2003**, *93*, 226.

[36] Silva E.E.C.M.; Tong L.; Yip S.; Van Vliet K.J. *Small* **2006**, *2*, 239.

[37] Wong E.W.; Sheehan P.E.; Lieber C.M. *Science* **1997**, *277*, 1971.

[38] Wu B.; Heidelberg A.; Boland J.J. *Nat. Mater.* **2005**, *4*, 525.

[39] Li X.D.; Gao H.S.; Murphy C.J., Caswell K.K *Nano Lett.* **2003**, *3*, 1495.

[40] Kis A.; Mihailovic M.; Remskar M.; Mrzel A.; Jesih A.; Piwonski I.; Kulik J.; Benoit W.; Forro L. *Adv. Mater.* **2003**, *15*, 733.

[41] Rafii-Tabar H. *Physics Reports* **2000**, *325*, 239.

[42] Zusmann E.; Rittel D.; Yarin A.L. *App. Phys. Letters* **2003**, *82*, 3958-3960.

[43] Demir M.M.; Yilgor I.; Yilgor E.; Erman B. *Polymer* **2002**, *43*, 3303-3309.

[44] Li W.J.; Laurencin C.T.; Caterson E.J.; Tuan R.S.; Ko F.K. *J. Biomedical Mater. Res.* **2002**, *60*, 613-621.

[45] Megelski S.; Stephens J.S.; Chase D.B.; Rabolt J.F. *Macromolecules* **2002**, *35*, 8456-8566.

[46] Srinivasan G.; Reneker D.H. *Polymer Inter.* **1995**, *36*, 195-201.

[47] Jaeger R.; Schonherr H.; Vancso G.J. *Macromolecules* **1996**, *29*, 7634-7636.

[48] Huang L.; McMillan R.A.; Apkarian R.P.; Pourdeyhimi B.; Conticello V.P.; Chaikof E.L. *Macromolecules* **2000**, *33*, 2989-2997.

[49] Huang L.; Apkarian R.P.; Chaikof E.L. *Scanning* **2001**, *23*, 372-375.

[50] Liu G.J.; Ding J.; Qiao L.; Guo A.; Dymov B.P.; Gleeson J.T.; Hashimoto T.; Saijo K. *Chemistry-a European Journal* **1999**, *5*, 2740-2749.

[51] Buchko C.J.; Chen L.C.; Shen Y.; Martin D.C. *Polymer* **1999**, *40*, 7397-7407.

[52] Chen Z.H.; Foster M.D.; Zhou W.; Fong H.; Reneker D.H.; Resendes R.; Manners I. *Macromolecules* **2001**, *34*, 6156-6158.

[53] Fong H.; Chun I.; Reneker D.H. *Polymer* **1999**, *40*, 4585-4592.

[54] Madden W.G. *J. Chem. Phys.* **1987**, *87*, 1405-1422.

[55] Mansfield K.F.; Theodorou D.N. *Macromolecules* **1990**, *23*, 4430-4445.

[56] Mansfield K.F.; Theodorou D.N. *Macromolecules* **1991**, *24*, 6283-6294.

[57] Harris J.G. *J. Phys. Chem.* **1992**, *96*, 5077-5086.

[58] Kumar S.K.; Russell T.P.; Hariharan A. *Chem. Eng. Sci.* **1994**, *49*, 2899-2906.

[59] Misra S.; Fleming P.D.; Mattice W.L. *J. Comput.-Aided Mater. Design* **1995**, *2*, 101.

[60] He D.Y.; Reneker D.H.; Mattice W.L. *Comput. Theor. Poly. Sci.* **1997**, *7*, 19-24.

[61] Rapold R.F.; Mattice W.L. *J. Chem. Soc. Faraday Trans.* **1995**, *91*, 2435-2441.

[62] Doruker P.; Mattice W.L. *Macromolecules* **1998**, *31*, 1418-1426.

[63] Doruker P.; Mattice W.L. *Macromolecules* **1999**, *32*, 194-198.

[64] Doruker P.; Mattice W.L. *J. Phys. Chem. B* **1999**, *103*, 178-183.

[65] Doruker P. *Polymer* **2002**, *43*, 425.

[66] Vao-soongnern V.; Doruker P.; Mattice W.L. *Macromol. Theory Sim.* **2000**, *9*, 1-13.

[67] Vao-soongnern V.; Mattice W.L. *Langmuir* **2000**, *16*, 6757-6758.

[68] Vao-soongnern V.; Ozisik R.; Mattice W.L. *Macromol. Theor. Sim.* **2001**, *10*, 553-563.

[69] Schreuder-Gibson H.; Gibson P.; Senecal K.; Sennett M.; Walker J.; Yeomans W.; Ziegler D. *J. Adv. Mater.* **2002**, *34*, 44-55.

[70] Zusmann E.; Yarin A.L.; Weihs D. *Experiments in Fluids* **2002**, *33*, 315-320.

[71] Deitzel J.M.; Kosik W.; McKnight S.H.; Beck Tan N.C.; DeSimone J.M.; Crette S. *Polymer* **2002**, *43*, 1025-1029.

[72] Ma M.L.; Hill R.M.; Lowery J.L.; Fridrikh S.V.; Rutledge G.C. *Langmuir* **2005**, *21*, 5549-5554.

[73] Gibson P.W.; Schreuser-Gibson H.L. ; Rivin D. *AICHE Journal* **1999**, *45*, 190-195.

[74] Schreuser-Gibson H.L.; Gibson P.W. *Int. Nonwoven J.* **2002**, *11*, 21-26.

[75] Norris I.D.; Shaker M.M.; Ko F.K.; MacDiarmid A.G. *Synthetic Metals* **2000**, *114*, 109-114.

[76] Wang Y.; Serrano S.; Santiago-Aviles J.J. *J. Mater. Sci. Letters* **2002**, *21*, 1055.

[77] Lee K.H.; Kim H.Y.; Khil M.S.; Ra Y.M.; Lee D.R. *Polymer* **2003**, *44*, 1287-1294.

[78] Lee K.H.; Kim H.Y.; La Y.M.; Lee D.R.; Sung N.H. *J. Poly. Sci. B Poly. Phys.* **2002**, *40*, 2259-2268.

[79] Ohgo K.; Zhao C.; Kobayashi M.; Asakura T. *Polymer* **2003**, *44*, 841-846.

[80] Huang L.; Nagapudi K.; Apkarian P.R.; Elliot C.L. *J. Biomater. Sci.-Poly. Ed.* **2001**, *12*, 979-993.

[81] Luu Y.K.; Kim K.; Hsiao B.S.; Chu B.; Hadjiargyrou M. *J. Controlled Release* **2003**, *89*, 341-353.

[82] Dersch R.; Liu T.; Schaper A.K.; Greiner A.; Wendorff J.H. *J. Poly. Sci. A Poly. Chem.* **2003**, *41*, 545-553.

[83] Abdeghani M.S.; Davies G.A. *Chem. Eng. Sci.* **1985**, *40*, 117-129.

[84] Uesaka T.; Qi D. *Proceed. Int. Pap. Phys. Conf.* **1995**, 65.

[85] Higdon J.J.L.; Ford G.D. *J. Fluid Mech.* **1996**, *308*, 341-361.

[86] Clague D.S.; Phillips R.J. *Phy. of Fluids* **1997**, *9*, 1562-1572.

[87] Chase G.G.; Beniwal V.; Venkatamaran C. *Chem. Eng. Sci.* **2000**, *55*, 2151-2160.

[88] Senoguz M.T.; Dungan F.D.; Sastry A.M.; Klamo J.T. *J. Composite Mater.* **2001**, *35*, 1285-1322.

[89] Tomadakis M.M.; Robertson T.J. *J. Composite Mater.* **2005**, *39*, 163-188.

[90] Koponen A.; Kandhai D.; Hellen E.; Alava M.; Hoekstra A.; Kataja M.; Niskanen K.; Sloot P.; Timonen J. *Phys. Rev. Letters* **1998**, *80*, 716-719.

[91] Mao N.; Russell S.J. *Textile Res. J.* **2003**, *73*, 939-944.

[92] Termonia Y. *Chem. Eng. Sci.* **1998**, *53*, 1203-1208.

[93] Cruz M.J.; Mayagoitia V.; Rojas F. *J. Chem. Soc. Faraday Trans. I* **1989**, *85*, 2079-2086.

[94] Mayagoitia V.; Cruz M.J.; Rojas F. *J. Chem. Soc. Faraday Trans. I* **1989**, *85*, 2071-2078.

[95] Mayagoitia V.; Rojas F.; Kornhauser I.; Aguilar H.P. *Langmuir* **1997,** *13*, 1327-1331.

[96] Mayagoitia V.; Rojas F.; Kornhauser I.; Zgrablich G.; Faccio R.J.; Golit B.; Guiglion C. *Langmuir* **1996**, *12*, 211-216.

[97] Ramirez-Cuesta A.J.; Cordero S.; Rojas F.; Faccio R.J.; Riccardo J.L. *J. Porous Mater.* **2001**, *8*, 61-76.

[98] Androutsopoulos G.P.; Salmas C.E. *Ind. Eng. Chem. Res.* **2000**, *39*, 3747-3763.

[99] Androutsopoulos G.P.; Salmas C.E. *Ind. Eng. Chem. Res.* **2000**, *39*, 3764-3777.

[100] Sampson W.W. *The Science of Papermaking,* Trans. XIIth Fund. Res. Symp. **2001**, 1205.

[101] Yamamoto S.; Matsuoka T. *Poly. Eng. Sci.* **1995**, *35*, 1022-1030.

[102] Yamamoto S.; Matsuoka T. *J. Chem. Phys.* **1995**, *102*, 2254-2260.

[103] Yamamoto S.; Matsuoka T. *J. Chem. Phys.* **1993**, *98*, 644-650.

[104] Ross R.F.; Klingenberg D.J. *J. Chem. Phys.* **1997**, *106*, 2949-2960.

[105] Skjetne P.; Ross R.F.; Klingenberg D.J. *J. Chem. Phys.* **1997**, *107*, 2108-2121.

[106] Ning Z.M.; Melrose J.R. *J. Chem. Phys.* **1999**, *111*, 10717-10726.

[107] Adanur S.; Liao T.Y. *Textile Res. J.* **1998**, *68*, 155-162.

[108] Adanur S.; Liao T.Y. *Textile Res. J.* **1999**, *69*, 816-824.

[109] Liao T.Y.; Adanur S. *Textile Res. J.* **1999**, *69*, 489-496.

[110] Liao T.Y.; Adanur S.; Drean J. *T. Textile Res. J.* **1997**, *67*, 753-760.

[111] Britton P.N.; Elliot C.F.; Graben H.W.; Gettys W.E. *Textile Res. J.* **1983**, *53*, 363-368.

[112] Britton P.N.; Gettys W.E. *Textile Res. J.* **1984**, *54*, 1-5.

[113] Wu X.F.; Dzenis Y.A. *J. Appl. Phys.* **2005**, *98*, 093501 (1-9).

[114] Termonia Y. *Textile Res. J.* **2003**, *73*, 74-78.

CHAPTER 3: MOLECULAR DYNAMICS SIMULATIONS OF SIZE-DEPENDENT STRUCTURAL AND THERMAL PROPERTIES OF POLYMER NANOFIBERS

Parts of the following study were published in 2007. [44]

3.1 Introduction

Various simulation techniques have been applied to investigate the confinement of polymeric systems in one or two dimensions. First, lattice Monte Carlo (MC) simulations of a melt-vacuum interface were performed by Madden using a film adsorbed on a solid surface [1]. The film was shown to have a central region with bulk-like characteristics, sandwiched between two interfacial regions. The structural features at the interface were found not to scale with molecular weight. Using off-lattice atomistic simulation, Mansfield et al. identified regions of thickness 1.0 nm at the surfaces of a thin film of atactic polypropylene of thickness 6.1 nm, in which local structural features were different from the bulk [2]. Again, no dependence of structural properties on the molecular weight (MW) was found in the interfacial region, for the MW range 1068-3246 g/mol. Short time scale dynamics of the atactic polypropylene-vacuum interface were then studied using molecular dynamics (MD) simulation [3]. While the structural features were in agreement with molecular mechanics results [2], enhancements in the mean-squared displacement of the atoms relative to the chain center of mass were observed in the surface region, compared to the bulk polymer. Harris [4] observed chain end segregation and flattening of chains at the liquid-vacuum interface in MD simulations of thin films comprising short-chain alkanes, and off-lattice MC simulations of thin films showed that chains exhibit predominantly bulk-like characteristics at the film center and are more collapsed at the vacuum surface [5]. MD simulations of thin films of poly-(1,4-cis-butadiene) showed that the sharp onset of orientation of the backbone bonds corresponds with the drop in mass density from its bulk value [6]. A thicker surface layer was found in MD simulations of amorphous polyethylene (PE) than in thin films of poly-(1,4-cis-butadiene), which was attributed to the stiffer nature of the PE chains [7]. A dynamic MC simulation method on a high coordination lattice was subsequently introduced by Mattice and co-workers [8] and used to determine equilibrium and dynamic properties of amorphous PE thin films [9, 10]. It was observed that the

segregation of chain ends contributed to increased mobility at the free surface of PE thin films [11]. The decrease in radius of gyration of chains was more significant for free-standing PE thin films as the molecular weight increased [12].

While there have been numerous studies of nanometer-thick films by simulation, to our knowledge, only two studies of polymer nanofibers have been reported to date [13-14]. Both of these employed the coarse-grained MC method on a high coordination lattice that was used previously for thin films [8-10] and nanoparticles [15]. Two PE nanofibers with diameters 5.6 and 7.6 nm were simulated [13] on a high coordination lattice, with interactions between occupied lattice sites designed to account for both short and long range interactions. It was found that the density profiles of these nanofibers could be fitted to a hyperbolic tangent profile, and there was significant segregation of end beads to the surface. Molecules were found to orient preferentially parallel to the surface, with the largest principal axis parallel to the surface. Diffusion coefficients of 5.6×10^{-6} nm^2/Monte Carlo step in the narrower nanofiber and 4.4×10^{-6} nm^2/Monte Carlo step for the thicker nanofiber were calculated for 1-D diffusion parallel to the fiber axis [14]. The mobility of the chains at the surface of the PE nanofiber was found to be greater than that of the chains at the center of the nanofiber. The overall chain mobility was found to increase as the fiber size decreased. Similar trends were observed for the free-standing thin films [10], implying that the curvature present in the fibers does not have a significant effect on the diffusion characteristics of the chain segments. The increased mobility in both the nanofibers and in the free-standing thin films was attributed to a region of lower mass density at the surface.

All of the above studies suggest that when polymers are confined in one or two dimensions, structural properties and dynamics show significant changes compared to those in bulk. These differences have implications for the properties of such materials confined on the nanometer length scale. For example, the glass transition temperature (T_g) of amorphous polymer thin films has been observed either to increase or decrease with decreasing film thickness [16-28], phenomena that have attracted great interest in recent years as part of a larger effort to understand the nature of the glass transition itself.

In this chapter, the effects of confinement and curvature on the structural and thermal properties of polyethylene nanofibers are investigated. Our aim is to evaluate these properties as a function of fiber diameter. In this way, we expect to develop a fundamental understanding of the extent and origin of fiber properties that emerge with decreasing diameter.

3.2 Simulation Methodology

3.2.1 Model

Molecular dynamics (MD) simulations of prototypical polyethylene (PE) nanofibers were performed using a large scale atomic/molecular massively parallel simulator (LAMMPS) [29]. LAMMPS is a classical MD code that efficiently model compliant materials such as polymers using a variety of force fields and boundary conditions. LAMMPS runs efficiently on single-processor machines but is designed for parallel computers, including Beowulf-style clusters. In the most general sense, LAMMPS integrates Newton's equations of motion for collections of atoms, molecules, or macroscopic particles that interact via short- or long-range forces with a variety of initial and/or boundary conditions. For computational efficiency LAMMPS uses neighbor lists to keep track of nearby particles. The lists are optimized for systems with particles that are repulsive at short distances, so that the local density of particles never becomes too large. On parallel machines, LAMMPS uses spatial-decomposition techniques to partition the simulation domain into small 3d sub-domains, one of which is assigned to each processor. Processors communicate and store "ghost" atom information for atoms that border their sub-domain.

In this work, a united atom force model for PE described originally by Paul et al. [30] and modified subsequently by Bolton et al. [31] and In't Veld et al. [32] was used. Since we implemented a united atom force field, the prototypical PE nanofibers were composed of methyl and methylene groups only, wherein the hydrogen atoms are lumped together with the carbon atoms. This force field has been shown to give an accurate description of

PE melts, as well as reasonable crystallization and melting transitions for n-alkenes [33-34]. The force field potential can be represented as follows:

$$\Phi = k_b (l - l_0)^2 + k_a (\theta - \theta_0)^2 + \sum_{i=1}^{3} \frac{1}{2} k_i [1 - \cos i\phi] + 4\varepsilon \left[\left(\frac{\sigma}{r} \right)^{12} - \left(\frac{\sigma}{r} \right)^{6} \right] \qquad (3.1)$$

In the equation above, the first term is the harmonic bond stretching potential where k_b = 1464.4 kJ/mol Å^2 and l_0=1.53 Å is the equilibrium C-C bond length. The second term is the harmonic bond angle bending potential where k_a=251.04 J/mol deg^2 is the angle bending parameter and θ_0=109.5° is the equilibrium C-C-C bond angle. The third term is the bond torsion potential, which accounts for all intramolecular interactions between atoms separated by three bonds. The parameters for this term are: k_1= 6.77 kJ/mol; k_2= -3.627 kJ/mol; k_3= 13.556 kJ/mol. The last term is the Lennard-Jones (LJ) potential, which is used to compute the nonbonded interactions between all united atom pairs that are on different chains or that are separated by four or more bonds on the same chain. The nonbonded potential parameters are: $\varepsilon(CH_2\text{-}\ CH_2)$ = 0.391 kJ/mol; $\varepsilon(CH_3\text{-}\ CH_3)$ = 0.948 kJ/mol, $\varepsilon(CH_2\text{-}\ CH_3)$ = 0.606 kJ/mol; σ = 4.01 Å (for all united atom types). The nonbonded interactions were truncated at a distance of 1 nm and were calculated between all united atom pairs that were located on two different molecular chains or that were separated by four or more bonds on the same chain.

In these MD simulations, the prototypical chain-like molecule consists of 50 to 300 carbon atoms (C50-C300). The simulation box length in the fiber axis direction, L_z, was chosen just short enough to suppress the growth of Rayleigh instabilities on the time scale of the simulation, typically $L_z < 2\pi R_{fiber}$, where R_{fiber} is the expected fiber radius. The initial bulk density for all systems was 0.75 g/cm^3 at 495 K. A time step of 1 fs was used. The simulations were run for durations 5 to 25 ns to characterize the relaxation times for different polymer chain lengths and to obtain equilibrated structures at the end of each stage of simulation (bulk and fiber). The total size of the systems varied between 200 and 150,000 carbons.

3.2.2 Simulation procedure

The nanofiber was constructed by the following method. First a simulation of desired size N (number of united atom groups) and cubic volume ($V=L_xL_yL_z$) was created, with periodic boundary conditions employed in all three Cartesian directions, such that the density was 0.75 g/cm^3. This system, which corresponds to the "bulk state", was simulated using LAMMPS. After equilibration in the bulk state, the box dimensions L_x and L_y were increased simultaneously by a factor of 3 to 4, such that the molecules no longer interacted with their images in these expanded directions. The system then interacts with its images only in one dimension; under these conditions, a cylindrically symmetric free surface spontaneously formed upon further equilibration, resulting in a section of a nanofiber. If the nanofiber is considered to be a cylinder, the z-direction along which the simulation box is still periodic, becomes the "fiber axis" or the "axial" direction of the fiber. The other two orthogonal directions, x and y, or any linear combination of these, become "radial" directions, which were confirmed to be indistinguishable during simulation. Figure 3.1 shows two perspectives of a typical nanofiber generated in this way. The fiber nomenclature reflects the number and length of chains within this representative volume element, or box: 20xC50 indicates 20 chains, each comprising 50 carbon atoms.

For the investigation of static properties, every system was simulated in an NVT ensemble at 495 K, which is well above the melting temperature of PE.

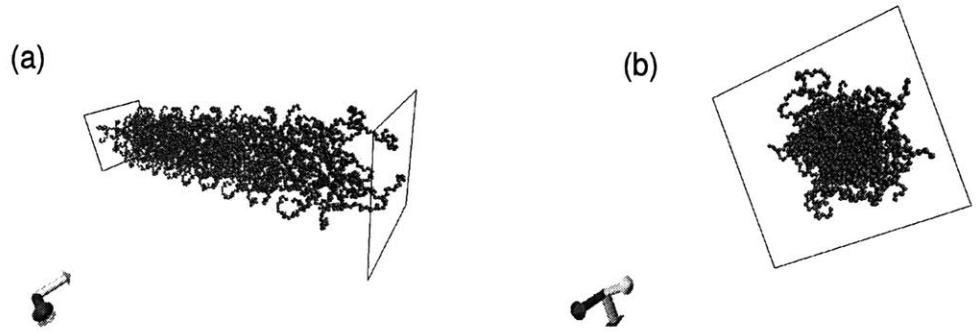

Figure 3.1 20xC50 polyethylene nanofiber at 495 K. The representative volume element includes 20 chains, each comprising 50 carbon-carbon atoms. (a) Inclined to fiber longitudinal axis; five periodic images in the axial direction are included for clarity. (b) Fiber cross-section. The fiber diameter is 3.54 nm.

3.3 Results

3.3.1 Radial density profile

The density profile is important in defining the surface and bulk regions of the fiber. For this analysis, the fiber was divided into cylindrically symmetric bins, or shells, starting from the center of the fiber. The number of atoms that fall into each shell was counted and normalized by the shell volume. This procedure was carried out for each snapshot and the ensemble averaged number density profile was calculated. This value was then converted to mass density of the fiber. The results for several systems are shown in Figure 3.2. As Figure 3.2 shows, the density within the core of the fiber spontaneously assumes the bulk density of the polymer. The increased fluctuation in density near r=0 is a consequence of poorer statistical sampling for bins of small radius and not significant. The mass density profiles for systems with the same total number of carbons are nearly identical, indicating that this result is insensitive to chain length.

The fiber diameter was determined using the Gibbs dividing surface method (GDS). The common definition of the Gibbs dividing surface was adopted, wherein the integral of the mass density profile equals the integral of the step function that takes the values of bulk

mass density or vacuum on either side of the GDS; this amounts to the conservation of mass. Hence, the interface mass density

$$2\pi\int_0^\infty \left(\rho(r) - \rho^{step}\left(r \mid r_{GDS}\right)\right) \cdot r dr = 0 \tag{3.2}$$

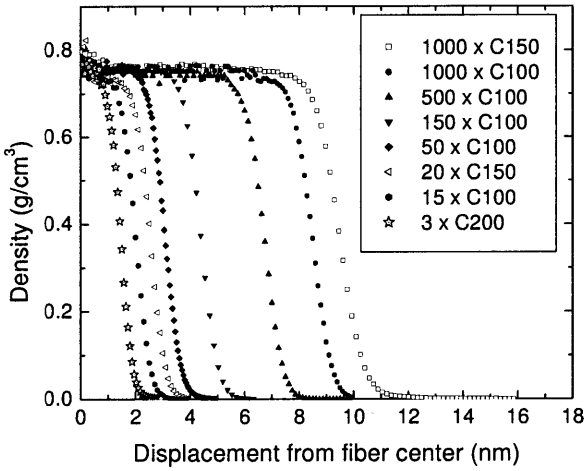

Figure 3.2 Density profiles extending from the fiber center provide a means to determine effective fiber diameter via the Gibbs dividing surface method. Here, fiber diameter can be varied via the number or molecular weight of the individual PE chains.

vanishes for this particular definition of the dividing surface, whose location is r_{GDS}. For the fibers simulated in this work, the diameters $2r_{GDS}$ obtained by this method range from 2.02 nm to 22.95 nm. These values were averaged over the entire simulation; analyses of diameter vs time did not reveal any low frequency "breathing" modes. The "90-10 interfacial thickness", which can be defined as the distance over which the mass density of the fiber decreases from 90% to 10% of the corresponding bulk value, is between 0.78 and 1.39 nm for all fibers studied at 495 K, and increases slightly with increasing fiber diameter. Table 1 summarizes these properties for various systems at 495 K.

N_{total}	System	D_{fiber}(nm)	L_z (nm)
200	4 x C50	2.02	1.8
300	2 x C150	2.38	2.1
300	3 x C100	2.38	2.1
400	4 x C100	2.52	2.3
500	10 x C50	2.79	2.4
600	12 x C50	2.96	2.6
600	6 x C100	2.9	2.6
600	4 x C150	2.92	2.6
600	3 x C200	2.91	2.6
600	2 x C300	2.92	2.6
900	18 x C50	3.52	3.1
900	9 x C100	3.44	3.1
900	6 x C150	3.41	3.1
1000	20 x C50	3.54	3.2
1500	15 x C100	4.11	3.6
1500	10 x C150	4.1	3.6
2000	40 x C50	4.63	4
3000	60 x C50	5.23	4.5
3000	30 x C100	5.2	4.5
3000	20 x C150	5.22	4.5
3000	15 x C200	5.18	4.5
4500	90 x C50	6.1	4.9
4500	30 x C150	6.15	4.9
5000	50 x C100	6.2	5.4
15000	150 x C100	8.9	7.9
50000	500 x C100	13.53	11.4
100000	1000 x C100	17.05	14.6
150000	1000 x C150	22.95	16.7

Table 3.1 Simulation system details and diameter values for simulated PE nanofibers at 495 K. (N_{total}: Total number of atoms, D_{fiber}: Fiber diameter, L_z: Length of the simulation box along z direction).

3.3.2 Energy density profile and Interfacial energy

The interfacial excess energy of the fibers can affect wetting and inter-fiber interactions. The enthalpic contribution to this quantity can be determined from the potential energy density, which is calculated by considering all interactions (bond stretching, angle bending, torsion, Lennard Jones) and apportioning the energy for each interaction equally among the particles involved. Figure 3.3 shows the energy density profiles for several systems. In order to define interfacial energy, the true energy profile is replaced by a step

function, where the step is located at the position r_{GDS} determined previously from the mass density profile. In general, the energy and mass density profiles do not coincide, and there is an excess energy at the interface that can be calculated as follows:

$$E_{\text{int}} = \left[E_{total} - E_{fiber} \right] / \left[2\pi r_{GDS} L \right] \tag{3.3}$$

where E_{int} is the interfacial excess energy and E_{fiber} is the energy of the fiber in the macroscopic limit, as defined below. L is an arbitrary length of the fiber. E_{fiber} and E_{total} are calculated from the following formulas:

$$E_{total} = 2\pi L \int_0^{\infty} E(r) r dr \tag{3.4}$$

$$E_{fiber} = E_{core} \pi r_{GDS}^2 L \tag{3.5}$$

where E_{core} is the energy density spontaneously adopted at the center or core of the fiber. E_{core} obtains a value of 580 J/cm^3 for fibers with $R_{\text{fiber}} > 2.0$ nm, equal to the bulk energy density determined from bulk simulations. For fibers with $R_{\text{fiber}} < 2.0$nm, E_{core} increases by 10% (580 J/cm^3 to 640 J/cm^3) as fiber radius decreases. The increase of E_{core} is mainly due to the loss of attractive LJ interactions in fibers with $R_{\text{fiber}} < 2.0$ nm. Figure 3.4 shows E_{core} as a function of fiber radius.

The excess interfacial energy was calculated to be ~ 0.022±0.002 J/m^2 and does not depend on the fiber radius. This value is similar to 0.02 J/m^2 (at 400 K) previously estimated by Mattice et al. for a thin film of PE, using their 2NND lattice model [35] and to 0.0254 J/m^2 (at 473 K) reported from experiments [36]. The temperature dependence of surface tension for PE melts is weak and has been determined empirically to be -0.057 * 10^{-3} J/m^2/K [36], implying a surface tension of 0.02414 J/m^2 at 495 K, which agrees within the margin of simulation uncertainty. However, the simulated values are internal energies, rather than free energies.

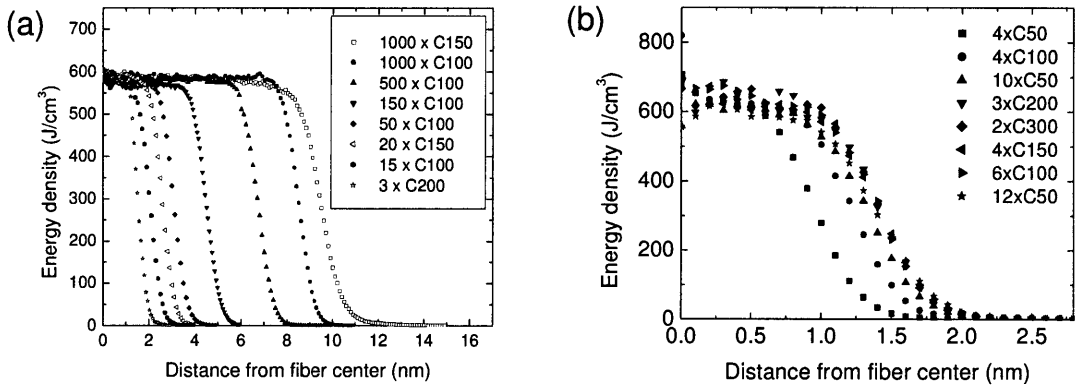

Figure 3.3 Energy density profiles extending from the fiber center to the surface enables the calculation of excess interfacial excess energy as a function of fiber size and molecular weight. a) Fibers with $R_{fiber} > 2.0$ nm, b) Fibers with $R_{fiber} < 2.0$ nm.

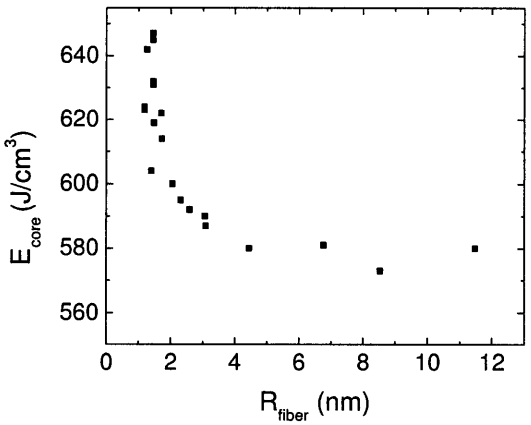

Figure 3.4 Energy at the fiber core E_{core} depends on fiber radius. This is illustrated for a simulation temperature of 495K.

3.3.3 Center of mass distribution and segregation of chain ends

The spatial distribution of chain centers of mass, shown in Figure 3.5, characterizes the structure at the level of entire chain. The center of mass profiles of the chains are expressed as the number of chains per volume of bin. For the same total system size (i.e., N_{total}), as the molecular weight decreases, number of center of mass of the chains per

volume increases. For the systems given in Figure 3.5, chain centers of mass are located mostly towards the middle of the fiber (i.e., 1.3 nm from the center of the fiber) and the position of the chains are independent of the number of chains in the system.

Figure 3.6 gives the relative density profile of the end (k=0 or k=99) and middle carbon atoms (k=50) across a fiber of R_{fiber} = 8.9 nm. The relative density profile was calculated by normalizing the end and middle bead densities by the total bead density in that bin, so that the segregation at the surface can be observed clearly. This segregation is typical in the sense that the end beads become more abundant closer to the vacuum. The behavior of the end beads distribution is determined mainly by entropic effects, contrary to the enrichment of centers of mass in the interface layer which is dependent on the energetic situation. This finding is in accordance with earlier results for the case of thin film [9,10] and nanofiber simulations [13].

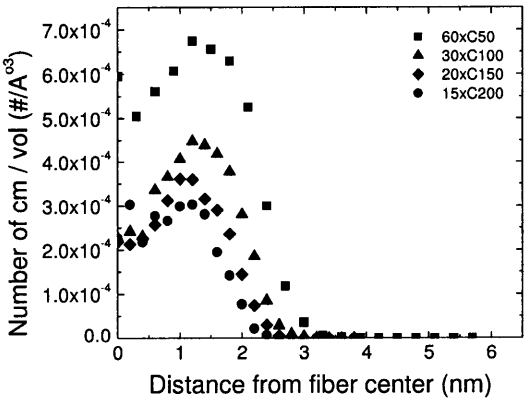

Figure 3.5 The center of mass distribution as a function of radial displacement from the fiber axis.

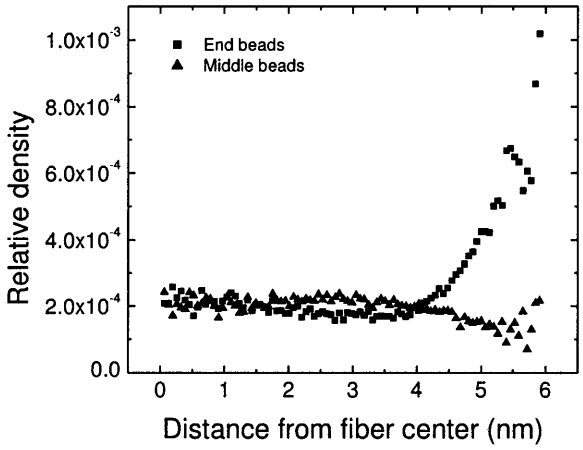

Figure 3.6 Relative density of middle and end beads as a function of radial displacement from the fiber center

3.3.4 Molecular conformations

Results from density and interfacial energy calculations show that surface properties can differ significantly from the properties at the center of the fiber. This may be attributed to perturbed conformations that the molecules take at the surface, under the influence of curvature and/or confinement. For this reason, the global equilibrium radius of gyration (R_g) values of chains within the fibers were calculated from the following formula:

$$\left\langle R_g^2 \right\rangle = \frac{1}{N_{chain}} \sum_{j=1}^{N_{chain}} \sum_{i=1}^{N_{segment}} \left(r_i - r_{cm,j} \right)^2 \tag{3.6}$$

Figure 3.7 shows radius of gyration values normalized by bulk radius of gyration ($R_g/R_{g,bulk}$) for each molecular weight as a function of fiber radius, also normalized by the corresponding bulk radius of gyration ($R_{fiber}/R_{g,bulk}$). In this way, the primary effect of chain length is removed. $R_{g,bulk}$ is calculated from the conformations of chains equilibrated in the melt phase. The deviation of $R_g/R_{g,bulk}$ from unity as $R_{fiber}/R_{g,bulk}$ decreases is a signature of the effects of confinement on chain conformation.

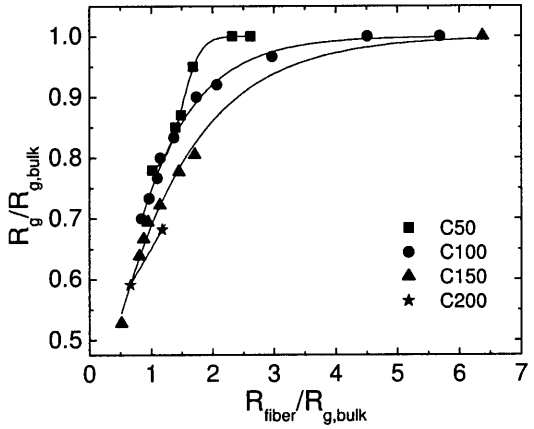

Figure 3.7 Normalized radius of gyration as a function of normalized fiber radius (at 495 K) shows significant confinement of the chains with increasing molecular weight and decreasing fiber size. Solid lines are intended to guide the eye.

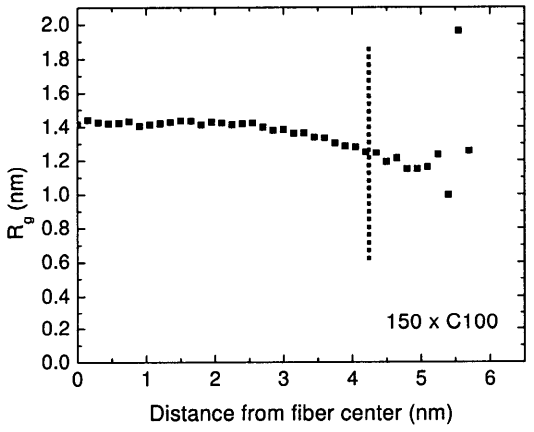

Figure 3.8 R_g vs distance from the fiber center shows that the confinement of chains penetrates over a distance approximately one R_g from the Gibbs Dividing Surface (GDS) to the fiber center. Vertical line represents the location of GDS.

The confinement of chains is clearly indicated: for smaller nanofibers, there is significant deviation from $R_g/R_{g,bulk}$, which is more pronounced for longer chains. As the fiber size

increases, the chains eventually acquire their $R_{g,bulk}$ values. It appears that chains confined within fibers having diameter less than 2 (for C50) to 4 (for C100) times the bulk radius of gyration are perturbed from their bulk state.

The R_g of the chains as a function of the distance from the fiber center (Figure 3.8) was also calculated. These results suggest that the confinement of the chains penetrates from the free surface, over a distance ~ R_g from the GDS towards the fiber center.

3.3.5 Local Orientation

Local orientation tendencies of chords (from carbon atom i to carbon atom i+2) across the fiber is examined in Figure 3.9. The chord order parameter is defined as

$$S_{local} = \frac{1}{2}\left\langle 3\left(\cos^2\theta\right) - 1 \right\rangle \tag{3.7}$$

where θ is the angle formed between a chord and the fiber axis. < > is indicative of an ensemble average within the cylindrical bin. The chord order parameter S_{local} would assume a value of -0.5, 0.0 or 1.0 respectively, for chords characterized by perfectly perpendicular, random and parallel orientation with respect to the fiber axis.

In Figure 3.9, the order parameter of the chords is plotted as a function of radial displacement from the fiber center. The line labeled "all" represents the orientation of all the chords. The other two lines are calculated for chords at the ends and middle of the chains. With reference to the fiber axis, there is no preference for the chord orientation in the bulk region of the fiber as indicated by $S_{local} = 0$ for random orientation. Toward the surface, the middle chords seem to prefer parallel orientation, whereas the end beads tend to stick out to the vacuum by normal orientation to the surface. These two opposite effects are averaged in the orientation of all chords.

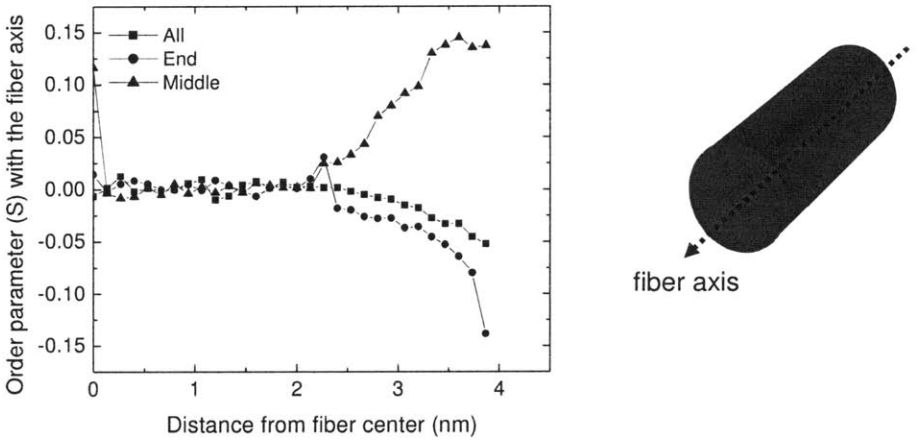

Figure 3.9 The orientation of chords (mid-,end- and all)

3.3.6 Glass transition temperature

3.3.6.1 Method

For the investigation of the glass transition temperature T_g of the fiber, the bulk structure was first cooled to 100K in the NPT ensemble, with an effective cooling rate of 1.97×10^{10} K/s, and the configurations at a series of temperatures were saved. Previous simulation studies [37] have shown that comparable cooling rates provide an estimate of the glass transition temperature that is ~30 K higher than the accepted experimental value; however, this offset should not significantly affect any trends in T_g. These configurations were then used as the initial configurations of the nanofiber at each temperature and the nanofibers were re-equilibrated in the NVT ensemble at each temperature. Only the axial dimension of the fiber is affected by the choice of ensemble; in all cases, the fiber radius is free to expand or contract, regardless of box size.

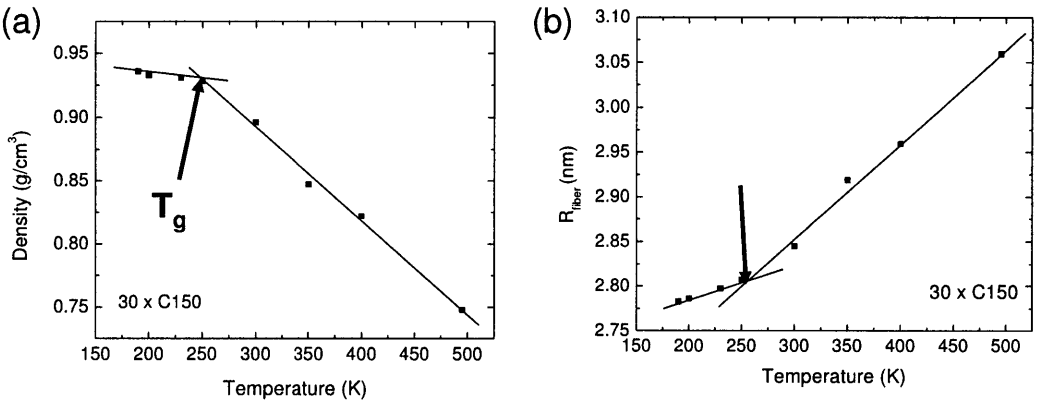

Figure 3.10 (a) Density at the center of the fiber as a function of temperature (b) R_{fiber} as a function of temperature.

3.3.6.2 T_g as a function of fiber size and layer model

To determine the T_g of nanofibers, a method that is commonly used in both experiments and simulations was employed. The mass density, which is related directly to the fiber radius, was monitored as a function of temperature. Since the liquid and the glassy states have different thermal expansion coefficients, R_{fiber} (T) changes slope upon crossing T_g. The T_g is determined as the intersection point of linear extrapolations from the liquid and glass sides; an illustration of this procedure is shown in Figure 3.10.

Figure 3.11 shows the T_g as a function of the fiber radius. As shown clearly in Figure 3.11, the T_g of the nanofibers are depressed with decreasing radius. The thickness-dependent depression in T_g has been demonstrated experimentally and computationally [16, 28] for a range of amorphous polymer thin films. Here, a similar behavior is observed for polymer nanofibers.

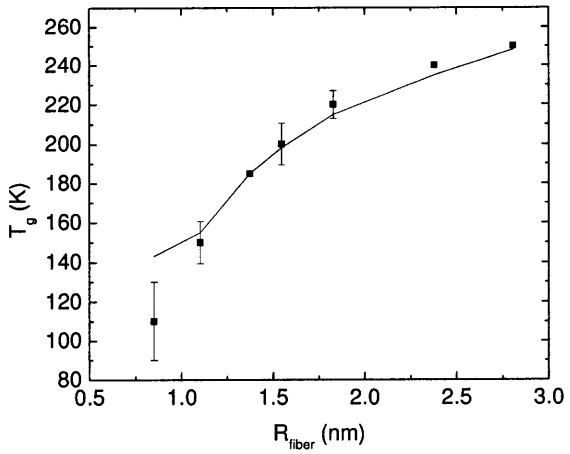

Figure 3.11 T_g as a function of R_{fiber} (at $T = T_g$) for nanofiber shows the depression of T_g with decreasing fiber radius. Solid lines are least squares regression to data.

To provide a physical interpretation for the depression of T_g in these nanofibers, a layer model similar to that proposed by Forrest and Mattson for low molecular weight free-standing thin films [27] can be used. The model can be applied to other geometries such as cylinder, sphere and ellipsoid. (See Appendix) This volume-averaged T_g formulation assumes a region near the free surface with enhanced mobility and depressed T_g ($T_{g,surf} < T_{g,bulk}$). For simplicity, $T_{g,surf}$ is assumed to be constant throughout the surface layer, although mobility may in fact vary within this layer. The thickness of this surface region is thought to be the same as the temperature-dependent length scale of cooperative motion for the glass transition dynamics, ξ(T). Assuming a single T_g equal to the bulk value for the fiber core, the average T_g value of the free-standing fiber is written as follows:

$$T_g = T_{g,bulk} - \left[\frac{2\xi(T_g)}{R} - \left(\frac{\xi(T_g)}{R} \right)^2 \right] \left(T_{g,bulk} - T_{g,surf} \right) \tag{3.8}$$

The factor of 2 in the linear term arises due to the 2-dimensional nature of confinement in case of the nanofibers. (See Appendix) A relation that accounts for the increase in the cooperativity length scale ξ(T) with decreasing temperature is given by:

$$\xi(T) = \xi(T_{ref}) + \sigma(T_{ref} - T)^{\gamma} \tag{3.9}$$

where σ and γ are empirical constants. A natural choice for T_{ref} was shown to be $T_{g,bulk}$, since the data can only be used to describe ξ(T) for $T < T_{g,bulk}$ [15]. The value $T_{g,bulk}$ = 280 K is used, reported previously for the simulated bulk amorphous polyethylene (C768) using the same force field [37].

Using equations 3.8 and 3.9 to obtain a least squares best fit to the simulation results in Figure 3.11, the following variables were calculated $T_{g,surf}$ =150±7 K, $\xi(T_{g,bulk})$ = 0.35±0.2 nm, σ=0.4±0.1 and γ=0.5±0.2 for the nanofibers. The solid lines in Figure 3.11 represent the best fit T_g data using these constants.

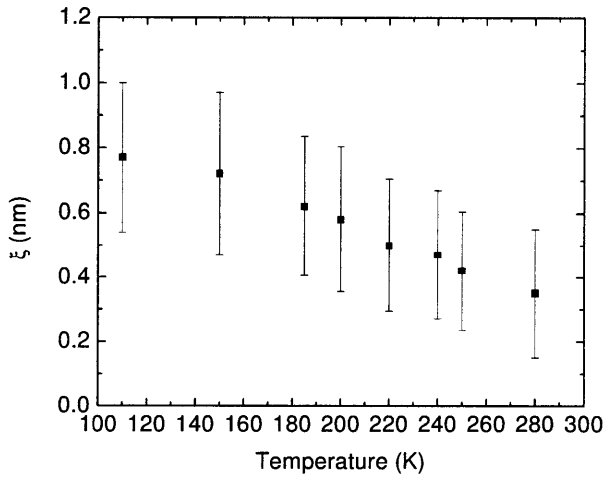

Figure 3.12 Cooperativity length scale ξ(T) as a function of temperature for the nanofibers.

Figure 3.12 shows ξ(T) calculated from these parameters. The layer theory predicts a cooperativity length for nanofibers, which is $\xi(T_{g,bulk})$ ~ 0.4 nm. This value is consistent with estimates for the size of the Cooperatively Rearranging Region (CRR) by Solunov

[38] for bulk polyethylene. Based on Solunov's estimate of 3.16 CH_2 units in the CRR and a bulk density of 0.75 g/cm^3, an independent estimate for $\xi(T_{g,bulk}) = \sqrt[3]{V_{CRR}}$ =0.46 nm can be obtained.

Experiments in amorphous thin films indicate that the depression of T_g is not a strong function of molecular weight for polymers of low to moderate molecular weight. The effect of molecular weight on the depression of T_g for PE nanofibers was also considered. Figure 3.13 shows T_g as a function of fiber radius for three different molecular weights, 700 g/mol (C50), 1400g/mol (C100) and 2100g/mol (C150). Clearly, a significant dependence of the T_g on the molecular weight of the polymer for the molecular weights within the simulated range is not observed. This observation also justifies application of the layer model to the simulation results, since this model was developed specifically to explain experimental data for thin films in the range of low molecular weights where T_g depression is observed to be molecular weight-independent.

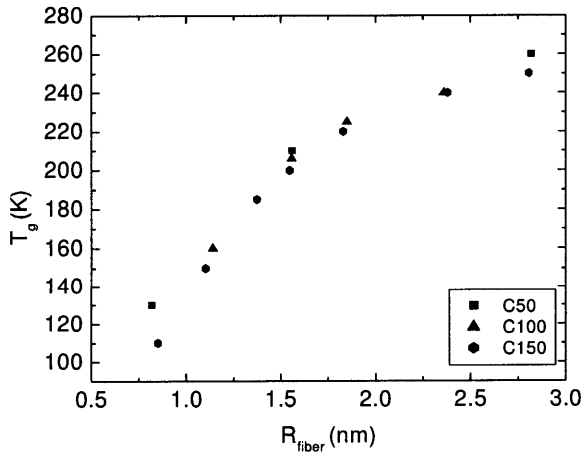

Figure 3.13 T_g as a function of R_{fiber} for molecular weights ranging from 700 g/mol (C50) to 2100 g/mol (C150) shows no significant dependence of T_g on molecular weight.

3.3.6.3 Comparison with experiments

To our knowledge, no studies on the experimental measurement of T_g on the free-standing amorphous polymer nanofibers have been reported in the literature. However, several groups investigated the T_g behavior of amorphous polymer thin films [16-28]. The first systematic study of the dependence of the T_g on film thickness in thin polymer films was performed by Keddie et al. using ellipsometry [17]. A series of polystyrene (PS) films of thicknesses between 10 nm and 200 nm were prepared on silicon wafers and reductions in T_g for films with thickness less than 40 nm were measured. Results obtained for PS films on a variety of substrates using numerous experimental techniques such as ellipsometry [17, 18], dielectric spectroscopy [19, 20], X-ray reflectivity [21], local thermal analysis [22] and probe fluorescence intensity measurements [23, 24] show a consistent decrease in T_g with decreasing film thickness, which is in agreement with our simulation results.

Numerous simulation studies have been conducted to reveal the underlying mechanism of the glass transition in spatially confined polymers. Torres et al. have demonstrated in MD simulations that the diffusivity of polymer segments is highly heterogeneous in polymer thin films, and that it is strongly correlated with deviations of T_g from the bulk [39]. An unentangled polymer melt confined between two repulsive walls was studied using MD simulations, and the reduction in T_g upon decreasing film thickness was explained by the faster chain dynamics due to the presence of the smooth walls [40-42]. Yoshimoto et al. [43] employed nonequilibrium MD simulations using a coarse grained polymer model, showing that mechanically soft layers are formed near the free surfaces of glassy thin films and that T_g also decreased as the film thickness decreased, which is also in agreement with our results.

3.4 Conclusions

We used MD methods to investigate the size-dependent properties of nanofibers for the prototypical polymer, polyethylene. The diameter of the largest fiber was ~23.0 nm,

which is comparable to diameters of nanofibers that can be prepared by electrospinning. In general, our results show that the fibers exhibit bulk-like structure and physical properties at the core of the fiber. Near the free surface, significant confinement of the molecules extends approximately one R_g from the GDS towards the fiber core. The interfacial excess energy is 0.022±0.002 J/m^2 and is not dependent on fiber diameter. The T_g of the amorphous PE nanofibers decreases by 50% as R_{fiber} decreases from 2.81 nm to 0.87 nm, and is not a function of molecular weight over the range considered. Application of a volume averaged layer model for T_g shows that the cooperativity length scale $\xi(T)$ compares well with previous estimates for polyethylene, but cannot explain the greater T_g depression of nanofibers compared to free-standing thin films of comparable thickness. This radius-dependent T_g depression can be attributed at least in part to the increase in the core energy of very small nanofibers ($R_{fiber} < 2.0$ nm). These results show that the physical properties of amorphous polymer nanofibers differ significantly from bulk and their thin film counterparts.

Chapter 4 addresses the emergent elastic and plastic deformation behavior of polymer nanofibers as a function of fiber diameter. This dependence (or lack thereof) is critical in potential applications of electrospun nonwoven mats, for which functional performance correlates strongly to mechanical stiffness of individual nanofibers.

REFERENCES

[1] Madden, W. G. *Journal of Chemical Physics* **1987**, *87*, 1405-1422.

[2] Mansfield, K. F.; Theodorou, D. N. *Macromolecules* **1990**, *23*, 4430-4445.

[3] Mansfield, K. F.; Theodorou, D. N. *Macromolecules* **1991**, *24*, 6283-6294.

[4] Harris, J. G. *Journal of Physical Chemistry* **1992**, *96*, 5077-5086.

[5] Kumar, S. K.; Russell, T. P.; Hariharan, A. *Chemical Engineering Science* **1994**, *49*, 2899-2906.

[6] Misra, S.; Fleming, P. D.; Mattice, W. L. Journal *of Computer-Aided Materials Design* **1995**, *2*, 101.

[7] He, D. Y.; Reneker, D. H.; Mattice, W. L. *Computational and Theoretical Polymer Science* **1997**, *7*, 19-24.

[8] Rapold, R. F.; Mattice, W. L. *Journal of the Chemical Society-Faraday Transactions* **1995**, *91*, 2435-2441.

[9] Doruker, P.; Mattice, W. L. *Macromolecules* **1998**, *31*, 1418-1426

[10] Doruker, P.; Mattice, W. L. *Macromolecules* **1999**, *32*, 194-198.

[11] Doruker, P.; Mattice, W. L. *Journal of Physical Chemistry B* **1999**, *103*, 178-183.

[12] Doruker, P. *Polymer* **2002**, *43*, 425.

[13] Vao-soongnern, V.; Doruker, P.; Mattice, W. L. *Macromolecular Theory and Simulations* **2000**, *9*, 1-13.

[14] Vao-Soongnern, V.; Mattice, W. L. *Langmuir* **2000**, *16*, 6757-6758.

[15] Vao-soongnern, V.; Ozisik, R.; Mattice, W. L. *Macromolecular Theory and Simulations* **2001**, *10*, 553-563.

[16] Keddie, J. L.; Jones, R. A. L.; Cory, R. A. *Europhysics Letters* **1994**, *27*, 59-64.

[17] Keddie, J. L.; Jones, R. A. L. *Israel Journal of Chemistry* **1995**, *35*, 21-26.

[18] Fukao, K.; Miyamoto, Y. *Physical Review E* **2000**, *61*, 1743-1754.

[19] Fukao, K.; Miyamoto, Y. *Europhysics Letters* **1999**, *46*, 649-654.

[20] Tsui, O. K. C.; Russell, T. P.; Hawker, C. J. *Macromolecules* **2001**, *34*, 5535-5539.

[21] Fryer, D. S.; Nealey, P. F.; de Pablo, J. J. *Journal of Vacuum Science & Technology B* **2000**, *18*, 3376-3380.

[22] Ellison, C. J.; Torkelson, J. M. *Nature Materials* **2003**, *2*, 695-700.

[23] Ellison, C. J.; Torkelson, J. M. *Journal of Polymer Science Part B-Polymer Physics* **2002**, *40*, 2745-2758.

[24] Keddie, J. L.; Jones, R. A. L.; Cory, R. A. *Faraday Discussions* **1994**, *98*, 219-230.

[25] Forrest, J. A.; DalnokiVeress, K.; Stevens, J. R.; Dutcher, J. R. *Physical Review Letters* **1996**, *77*, 2002-2005.

[26] Forrest, J. A.; DalnokiVeress, K.; Dutcher, J. R. *Physical Review E* **1997**, *56*, 5705-5716.

[27] Forrest, J. A.; Mattsson, J. *Physical Review E* **2000**, *61*, R53-R56.

[28] Dalnoki-Veress, E.; Forrest, J. A.; Murray, C.; Gigault, C.; Dutcher, J. R. *Physical Review E* **2001**, *3*, 6303.

[29] Plimpton S. *J. Comput. Phys.* **1995**, *117* (1), 1-19.

[30] Paul W.; Yoon D.Y.; Smith G.D. *J. Chem. Phys.* **1995**, *103*, 1702-1709.

[31] Bolton K.; Bosio S.B.M.; Hase W.L.; Schneider W.F.; Hass K.C. *J Chem Phys B* **1999**, *103*, 3885.

[32] In't Veld P.J.; Rutledge G.C. *Macromolecules* **2003**, *36*, 7358-7365.

[33] Waheed N.; Lavine M.S.; Rutledge G.C. *J. Chem. Phys.* **2002**, *116*, 2301-2309.

[34] Harmandaris V.A.; Mavrantzas V.G.; Theodorou D.N. *Macromolecules* **1998**, *31*, 7934-7943.

[35] He D.Y.; Reneker D.H.; Mattice W.L. *Comput. Theor. Polym. Sci.* **1997**, *7(1)*, 19-24.

[36] Brandrup J.; Immergut E.H.; Grulke E.A.; Abe A.; Bloch D.R. In *Polymer handbook*, 4th ed.; John Wiley & Sons: New York, 1999.

[37] Capaldi F.M., Boyce M.C., Rutledge G.C., *Polymer* **2004**, *45(4),* 1391-1399.

[38] Solunov C.A *Eur. Poly. J.* **1999**, *35*, 1543-1556.

[39] Torres, J. A.; Nealey, P. F.; de Pablo, J. J. *Physical Review Letters* **2000**, *85*, 3221-3224.

[40] Varnik, F.; Binder, K.; Baschnagel, J. *International Journal of Modern Physics C* **2002**, *13*, 799-804.

[41] Varnik, F.; Baschnagel, J.; Binder, K. *Physical Review E* **2002**, *65*, 2.

[42] Varnik, F.; Baschnagel, J.; Binder, K. *Journal of Non-Crystalline Solids* **2002**, *307*, 524-531.

[43] Yoshimoto, K.; Jain, T. S.; Nealey, P. F.; de Pablo, J. J. *Journal of Chemical Physics* **2005**, *122*, 14).

[44] Curgul S.; Van Vliet K.J.; Rutledge G.C. *Macromolecules* **2007**, *40*, 8483.

CHAPTER 4: MODELING AND MECHANICAL CHARACTERIZATION OF ISOLATED POLYETHYLENE NANOFIBERS

Parts of the following study were published in 2009. [1]

4.1 Introduction

Mechanical properties of polymeric nanostructures are of critical importance in a wide variety of technological applications. Such applied forces and resulting displacements may result in permanent deformation and eventually mechanical failure of individual nanofibers. The properties of the nonwoven materials are convoluted functions of the inherent properties of these fibers, as well as the organization of and interactions among fibers within the nonwoven material. Therefore, it is desirable to determine independently the mechanical properties of single nanofibers.

In recent years, various attempts have been made to quantify the elastic properties of isolated polymer fibers of diameter $d < 1$ μm via direct experimental measurements [7-18]. Mechanical characterization techniques that have been developed to test individual polymer fibers include uniaxial tensile loading, as well as bending and indentation of individual fibers using atomic force microscopy (AFM) cantilevered probes to impose deformation. The details of these studies as well as a summary of the findings from these studies can be found in Chapter 2.3.1.

Although these experimental methods can provide information on the Young's elastic modulus, E, yield strength, σ_y, and fracture strength, σ_f of nanofibers, several challenges exist that limit the precision and accuracy of these mechanical property measurements. These challenges include the required force resolution, the difficulty of preparing, isolating, and manipulating such small fibers without compromising them, and the dearth of suitable modes of imaging or displacement measurements that do not damage the fibers. Due to these difficulties, to the best of our knowledge, experimental data are not available for the elastic or plastic properties of polymer nanofibers with diameters less than 50 nm. Therefore, it is not yet clear if the stiffening and strengthening effects described in Chapter 2 are peculiar to fibers in the range of diameters from ~70-500 nm,

or if these trends would persist to even smaller length scales. Molecular scale simulations can provide valuable insights to help predict and understand the mechanical behavior of such small-scale structures, and to identify any emergent behavior that is a consequence of their nanoscale dimensions.

Previous computational simulations of amorphous (glassy) polymeric, prismatic cantilevered plates adhered to a substrate have shown that the overall bending modulus of the plate remains comparable to bulk materials, until the width of the plates approaches a critical value of 20σ; where σ is the diameter of the coarse-grained polymer segments [19, 20]. Below the critical plate width, the bending modulus decreases with decreasing width and can be significantly smaller than that of the bulk polymer. Workum et al. [20] showed that the material in the surface region comprises a significant fraction of the entire width of the plate, so that deviations from bulk behavior can be significant. Nonequilibrium molecular dynamics simulations using a coarse grained polymer model showed that compliant layers form near the free surfaces of glassy thin films [21]. These authors also calculated that the ratio of the surface layer thickness increased to more than half of the entire film thickness as the temperature approached the T_g of the bulk polymer [21]. Although two studies of the structural and physical properties of simulated, glassy polymer nanofibers have been reported to date, mechanical properties of such fibers have not been calculated [22, 23]. However, experimental studies of amorphous polymer thin films suggest that the stiffnesses of polystyrene (PS) or poly(methylmethacrylate) (PMMA) thin films of thickness <40 nm on poly(dimethylsiloxane) (PDMS) substrates, as inferred from elastic buckling of the adhered films, are significantly less than those of bulk counterparts [24, 25]. This behavior was explained by applying a composite model that consisted of a compliant surface layer of reduced elastic modulus and a bulk-like region at the film center [25]. Wafer curvature experiments have also indicated that the biaxial elastic modulus of PS thin films of 10 nm thickness is an order of magnitude smaller than that of the corresponding, bulk PS [26].

Experiments and simulations therefore suggest that mechanical properties of polymer nanostructures (i.e., free-standing or adherent thin films of nanoscale thickness and fibers

of nanoscale diameter) can deviate significantly from that of the bulk polymer counterparts, but with very different trends. Whereas the properties of adherent thin films depend strongly on the substrate to which the film is adhered, free-standing films and fibers might be expected to behave more similarly. Given these discrepancies, the fundamental questions addressed in this chapter are (1) whether the elastic and plastic properties of simulated, amorphous polymer nanofibers are indeed different from those of the bulk material or thin film counterparts; and (2) if these properties in fact differ from bulk predictions, how this deviation depends on the fiber dimensions for fiber radii < 10 nm. The discussion in this chapter includes the effect of surface tension on the axial force-elongation response of nanofibers at low strain, elastic properties as a function of fiber radius R_{fiber} and temperature, and the characterization of σ_y and post-yield behavior as functions of nanofiber radius and temperature.

4.2 Method

Free standing PE nanofibers were prepared in a two-step molecular dynamics (MD) scheme as explained in more detail in Section 3.2.1. To determine the mechanical properties of solid PE nanofibers, bulk structures were cooled down from 495 K to 100 K with an effective cooling rate of 1.97×10^{10} K/s. We used an *NPT* ensemble with a constant, isotropic pressure of $P=10^5$ Pa during cooling. We saved configurations at three different temperatures (100 K, 150 K and 200 K) for determination of bulk mechanical properties, and subsequently used these configurations to construct nanofibers. In this second step, the simulation box dimensions were increased simultaneously in two directions (i.e., x and y) without rescaling coordinates, such that the system no longer interacted with its images in these directions. The box dimension was unchanged in the third direction (i.e., z). Upon subsequent relaxation in the NVT ensemble for 10 ns at the desired temperature, the system reduced its total energy by forming a cylindrically symmetric free surface concentric with the z-axis of the box. The resulting nanofiber was fully amorphous and periodic along the z-direction. The bulk configurations at 100 K, 150 K and 200 K were also equilibrated in the NPT ensemble with the usual periodic boundary conditions in x, y, and z, before deformation to determine the bulk mechanical properties.

Deformation of fibers was simulated by controlling the displacement of the z dimension of the simulation box to induce uniaxial deformation parallel to the fiber axis; the free surfaces of the fibers were unconstrained. Deformation of the bulk configurations was simulated by rescaling one dimension of the simulation cell, while allowing the other two orthogonal dimensions to fluctuate in response to the barostat, as described in detail in Capaldi et. al. [27]. The resulting strain rate for all temperatures ranged from 2.5×10^8 s^{-1} to 10^{10} s^{-1}. For the fibers, results are presented initially in the form of applied force versus strain, since converting force to stress requires an assumption regarding the cross-sectional area of the fibers. As argued previously [28], defining the cross-sectional area requires a subjective decision, the effect of which becomes significant when the material dimensions are reduced to a length scale comparable to the size of the atoms themselves (~1 nm); different methods for defining the diameter of a fiber can thus lead to significant differences in the value of stress obtained. Samples were deformed in both compression and tension up to a strain $\varepsilon = \pm 0.05$, which is in the linear elastic deformation range at temperatures of 100 K and 150 K, as confirmed by the linearity of the computed force-strain response over this range. In the case of 200 K simulations, the force-strain response was linear only up to a strain $\varepsilon = 0.02$. To improve the signal-to-noise ratio in the computed virial equation for forces acting on the fiber (for small systems), four different initial configurations were simulated under identical conditions, and the resulting force-strain curves were averaged. Where necessary to compute stress, the Gibbs dividing surface (GDS) was invoked to define the diameter of the fibers, as described previously in Section 3.3.1. Young's elastic modulus was calculated from the slope of the stress-strain response in the linear elastic regime. The plastic deformation behavior of both bulk and nanofibers was also studied by continuing deformation up to a total strain $\varepsilon = 0.2$ at 100 K and 150 K with a constant strain rate of 10^9 s^{-1}. In order to analyze if the fibers were plastically deformed at the end of this simulation (after the system was uniaxially elongated to a total strain $\varepsilon = 0.2$ along the fiber axis), an NPT ensemble MD simulation was carried out. In this simulation, the box dimension along the fiber axis was allowed to fluctuate in response to the barostat. Permanent deformation of the fibers, which was observed at the end of this simulation, was recognized as the signature of plastic

deformation. For each simulation, data for force versus strain during plastic deformation were averaged over a strain interval of 0.002. The axial force on the fiber at yield was calculated from the intersection of two lines, the first being fit to the force-strain curve in the low strain, elastic deformation region and the second being fit to the force-strain curve in the plastic deformation region; yield stress was thus computed as the force at yield (intersection of these piecewise linear fits) normalized by the GDS-defined cross-sectional area of the fiber.

4.3 Results

4.3.1 Effect of surface tension on stress

Table 4.1 summarizes the simulated systems to calculate mechanical properties.

Table 4.1 Chain length and radius values, determined via the GDS method, for simulated PE nanofibers at 100 K and 150 K.

N_{total}	L@100 K(nm)	R_{fiber} @100 K(nm)	L@150 K(nm)	R_{fiber} @150 K(nm)
15xC100	3.39	1.848	3.40	1.875
30xC100	4.27	2.312	4.29	2.371
30xC150	4.88	2.762	4.90	2.794
150xC100	7.29	4.1	7.33	4.148
500xC100	10.92	6.15	10.98	6.2
1000xC100	13.75	7.71	13.79	7.75
1500xC150	15.75	8.84	15.80	8.94

Figure 4.1 shows the force-strain response of a nanofiber that was deformed uniaxially at 100 K. A closer inspection of this figure reveals that the force does not decrease to zero at zero applied strain. This is a feature of the nanofibers that is also suggested by continuum mechanics to be a consequence of surface tension [29]. Simulations of bulk systems (i.e., periodic boundary conditions in x, y, and z with no free surfaces) confirm that the force-strain responses indeed passes through the origin in this case.

To investigate the finite force that is observed in the force-strain response, we calculated the instantaneous force tensor for equilibrated nanofibers (i.e., no elongation/compression) from the virial tensor W as

$$f = -\frac{1}{L_{fiber}}\left[\sum_{i}^{N_{bond}} W_{bond,ij} + \sum_{i=}^{N_{angle}} W_{angle,i} + \sum_{i=1}^{N_{dihed}} W_{dihed,i} + \sum_{i=1}^{N_{atom-1}}\sum_{j=i+1}^{N_{atom}} W_{LJ,ij} + \sum_{i}^{N_{atom}} W_{kinetic}\right] \quad (4.1)$$

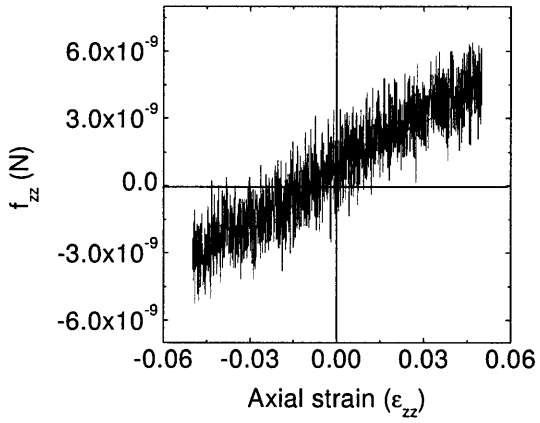

Figure 4.1 Force along the axial direction (f_{zz}) as a function of axial strain (ε_{zz}) in the elastic regime for a nanofiber with N/L= 2057.61 united atoms per nm of fiber length (R_{fiber} = 4.1 nm by the GDS method) at 100 K.

where L_{fiber} is the length of the fiber. Equation 4.1 is the summation of all contributions due to bond stretching, bond angle bending, bond torsion, Lennard-Jones interactions and kinetic contributions. The explicit expressions of the virial contributions can be found elsewhere [30, 31]. We calculated the force tensor in cylindrical coordinates, appropriate to the geometry of the fibers. Figure 4.2 shows the radial force f_{rr} as a function of distance from the fiber center. For this analysis, the fiber was divided into concentric cylindrical shells, starting from the fiber axis. The virial contributions were summed for the atoms that belonged to the same cylindrical shell. To translate the results for f_{rr} into radial stress σ_{rr}, we define R_{fiber} according to the GDS method. The radial stress is given by

$$\sigma_{rr} = \frac{f_{rr}}{\pi R_{fiber}^2} \tag{4.2}$$

The surface tension can be calculated by integrating the radial stress σ_{rr} as follows:

$$\gamma = \int_0^\infty \sigma_{rr} dr \tag{4.3}$$

Figure 4.3 shows the magnitude of surface tension calculated from equation 4.3 as a function of fiber radius. The error bars represent the standard deviation for the four different configurations simulated.

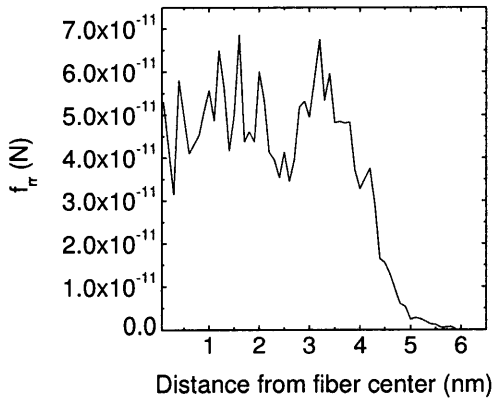

Figure 4.2 Radial force profile extending from the fiber core to the free surface enables the calculation of radial stress. (R_{fiber} = 4.1 nm by the GDS method at 100 K.)

Here, we can also explore the validity of the continuum theory and Young-Laplace equation for small diameter fibers [29]. This equation can be written as follows for a cylinder:

$$\sigma_{zz} = \frac{\gamma}{R_{fiber}} \tag{4.4}$$

where γ is surface tension and R_{fiber} is the fiber radius. This relation suggests that there is a finite stress on the nanofibers due to the contribution of surface tension, even in the absence of elongation or applied force. The relative contribution of this finite stress term naturally increases as the fiber radius decreases.

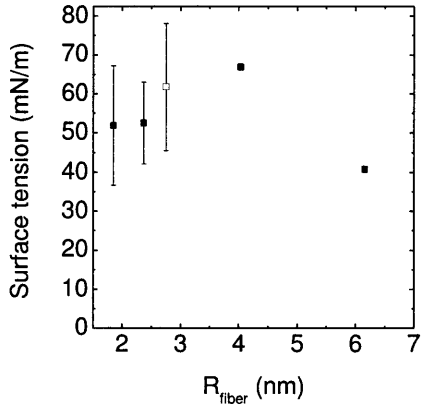

Figure 4.3 Surface tension as a function of R_{fiber}, as calculated from the radial component of the stress tensor at 100 K. Solid squares represent systems with chain length C100; open squares represent systems with chain length C150.

Since we calculated both σ_{rr} and σ_{zz} directly from the virial equation of atomistic interactions as detailed above, we can calculate a second estimate of the surface tension γ, subject to the validity of equation 4.4. Estimates of γ using equation 4.3 and equation 4.4 agree within 1 mN/m. These estimates from computational simulations also compare well with an experimental estimate of 44.7 mN/m for amorphous polyethylene at 100 K, obtained by extrapolation from the experimentally measured surface tension of a polyethylene melt between 423 and 473 K [32]. These results confirm that the source of the finite stress at zero elongation is the surface tension, and that the continuum theory is capable of accounting for this phenomenon even at these very small length scales.

4.3.2 Elastic deformation and the layer model

From the slope of force versus strain (f_{zz}–ε response) in the elastic regime (Figure 4.1), under uniaxial tension and compression parallel to the fiber long-axis, we compute the quantity F, which has units of force and is related to the elastic modulus through the cross-sectional area, $F=EA$.

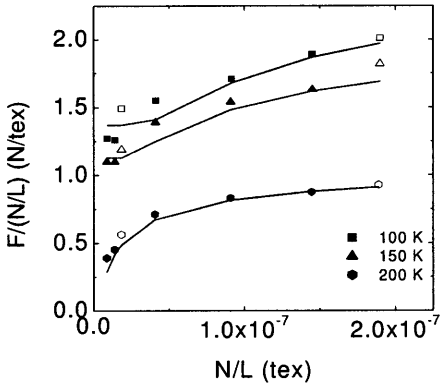

Figure 4.4 Dependence of *F/(N/L)* on fiber parameter *N/L* at three different temperatures: 100 K, 150 K and 200 K and at a strain rate of $2.5\text{x}10^{8}$ s^{-1}. See text for details. Solid symbols represent systems with chain length C100; open symbols represent systems with chain length C150.

Figure 4.4 shows the quantity *F/(N/L)* as a function of *N/L* at 100, 150 and 200 K. N is the number of atoms in the simulation and L is the length of the simulation box along the z direction (the fiber axis) Thus, *N/L* is proportional to the linear density (mass per unit length) of the fiber, which is conventionally expressed in units of tex in the fiber industry; tex is the mass in g of 1 km of fiber. *F/(N/L)* is proportional to the specific modulus of the fiber (E/ρ where ρ is the density of the fiber) and is conventionally expressed in units of *N*/tex. The use of fiber industry units here avoids the need to introduce a definition for fiber radius in order to characterize the fiber deformation behavior. All three temperatures are below the glass transition of bulk PE (280±30 K [27]), and were chosen to bracket the glass transition temperature estimated for the surface of these fibers (150 K). As can be seen from this figure, the specific modulus *F/(N/L)* decreases with

decreasing *N/L* for all temperatures considered. The specific moduli for fibers of various sizes at 150 K are slightly lower than those at 100 K; between 150 K and 200 K, the specific modulus drops significantly. This is an indication of the increased compliance of the surface layer within this temperature range, which contributes noticeably in nanofibers of diameter $d < 40$ nm.

In order to interpret these results for deformation of nanofibers in terms of deviation from bulk-like behavior, it is necessary to compute the Young's modulus, E. For this purpose, we re-introduce R_{fiber}, defined using the GDS method. Figure 4.5 shows E as a function of R_{fiber}. By simulation, we determined the Young's modulus of the bulk PE E_{bulk} to be 2360, 1838 and 900 MPa at 100, 150 and 200 K, respectively, under an applied strain rate of $2.5\text{x}10^{8}$ s^{-1}. At a strain rate of 1×10^{10} s^{-1}, E_{bulk} was found to increase to 2758, 2490 and 1800 MPa at the same three temperatures, respectively. This strain rate dependence of E for simulated bulk PE below the glass transition has been noted previously [33]. It is likely that some relaxation mechanisms in the glassy state are suppressed at the higher strain rate. Nevertheless, the main finding – that decreasing fiber size results in increasing compliance – is relatively insensitive to strain rate, so we report further results only for the lower simulated strain rate. For all three temperatures, the Young's moduli of the fibers are lower than that of the corresponding bulk configurations.

To explain the dependence of Young's modulus on the fiber radius, we make use of composite material theory. We assume that the core of the fiber consists of bulk-like material with a Young's modulus equal to that of the bulk E_{bulk}, and a surface region that is more compliant, with $E_{\text{surf}} < E_{\text{bulk}}$. Assuming uniform strain throughout the fiber (i.e., the Voigt limit for material composites), we have:

$$E = E_{bulk} f_{bulk} + E_{surf} f_{surf} \tag{4.5}$$

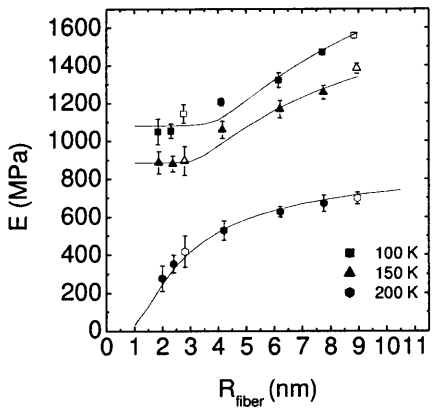

Figure 4.5 E vs. R_{fiber} at 100K, 150 K and 200 K and at a strain rate of $2.5\text{x}10^{8}$ s^{-1}. The data points represent simulation data; the solid lines show the best fit to the composite model described in the text. Symbols are the same as in Figure 4.4. The reasonable fit of the data at larger R_{fiber} indicates that the mechanical behavior is well-described by a mechanically effective surface layer of constant thickness.

where E is the calculated elastic modulus of the fiber, f_{bulk} is the volume fraction of the bulk-like core and $f_{surf} = 1 - f_{bulk}$ is the volume fraction of the surface layer. The core volume fraction f_{bulk} can be written as:

$$f_{bulk} = \left(1 - \frac{\xi}{R_{fiber}}\right)^2 \tag{4.6}$$

where ξ is the thickness of the mechanically effective surface layer; this parameter characterizes the length scale over which the elastic response of the fiber varies. ξ was further assumed to depend only on temperature; for fibers of radius less than ξ, we set $\xi = R_{\text{fiber}}$.

We used best fits of equations 4.5 and 4.6 to our simulated results to determine values for both ξ and E_{surf} at each temperature, as shown in Figure 4.6. According to equations 4.5

and 4.6, the effective Young's modulus of the fibers should approach E_{surf} for fibers with small radii, on the order of ξ or less, and should asymptotically approach to E_{bulk} for fibers much larger than ξ. For the range of fiber radii simulated, the approach to E_{surf} around $R_{fiber}=\xi$ is accurately captured at 100 and 150 K, while the approach to E_{bulk} at large R_{fiber} is observed at 200 K. Figure 4.6 indicates the dependence of ξ on R_{fiber} at all temperatures. From the fit to the two-layer composite model, we obtain values for E_{surf} of 1050, 890 and 30 MPa at temperatures of 100, 150 and 200 K, respectively. For ξ, we obtain values (at sufficiently large fiber radius R_{fiber}) of 3.4, 2.8 and 1.0 nm at temperatures of 100, 150 and 200 K, respectively. In other words, both the modulus and the thickness of the mechanically effective surface layer decrease as the temperature increases from below to above the glass temperature of the surface layer.

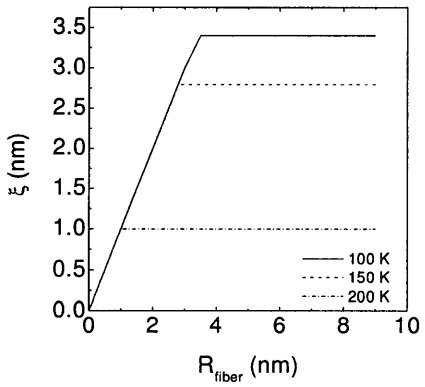

Figure 4.6. ξ vs. R_{fiber} at 100, 150 and 200 K suggests that the mechanically effective surface layer thickness decreases with increasing temperature.

Enhanced surface mobility of glassy polymer thin films and nanostructures has been demonstrated by several experiments [34, 35] and simulations [20, 36]. As the dimensions of the nanostructures decrease, the surface to volume ratio increases, and thus the amount of material at the surface becomes a more significant volume fraction of the entire structure, and is reflected in the overall properties. The increased mobility at the surface can cause significant stress relaxations in the mechanically effective surface layer

quantified by ξ. According to our model (Figure 4.6), the distance over which these relaxations occur can be as large as twice the radius of gyration of the chain ($R_{g,bulk}$ = 1.6 nm for C100) at 100K. The thickness of this layer decreases to 2.8 nm at 150K and 1.0 nm at 200K. For amorphous polymer thin films of PS or PMMA on PDMS substrates, Stafford et al. [24] estimated a surface layer of thickness 2 nm with an elastic modulus lower than that of the corresponding bulk polymer. Sharp et al. [37] suggested the existence of a liquid-like surface layer with thickness of 3-4 nm, from studies of 10 nm- and 20 nm-diameter gold spheres embedded into a PS surface. They also estimated the thickness of this layer to be 5±1 nm from ellipsometry measurements [37]. These estimates compare favorably with our results for ξ of simulated amorphous PE.

The decrease in the thickness of the mechanically effective surface layer with increasing temperature is similar to the behavior that we noted previously for the cooperatively rearranging region (CRR), which we used to explain trends in the glass transition temperature as a function of PE nanofiber diameter. It is well established that structural relaxation in amorphous polymers occurs through cooperative rearrangements that involve larger domains of material as the temperature is reduced through the glass transition [38]. Similar behavior can be expected for ξ. However, the ξ determined here for the mechanically effective surface layer are larger than those of the CRR for thermal relaxations, for which we previously calculated values of 1.0, 0.75 and 0.58 nm at 100, 150 and 200 K, respectively. To the best of our knowledge, there is no study in the literature that compares the thickness ξ of the mechanically effective surface layer with that of the CRR. Our results show that cooperative mechanical displacement occurs over a larger distance (ξ) than thermal rearrangements (CRR), requiring the involvement of more repeat units. Although mechanical loads can be transmitted along an appreciable fraction of the entire chain length, thermal relaxations take place over a smaller number of repeat units, resulting in smaller surface layer thickness. Although the two-layer composite model appears to be a reasonable approximation to explain deviations in T_g and in E from bulk material, this model is nevertheless simplistic, and its estimates are certainly approximate. More complex models may need to be devised in order to

rationalize quantitatively the complex physics underlying thermal and mechanical properties of nanofibers with those of the bulk and thin films.

4.3.3 Poisson's ratio as a function of fiber diameter

The Poisson's ratio ν of the PE nanofibers as a function of fiber size and temperature was also calculated directly from the ratio of radial and axial strains. As Figure 4.7 shows, ν decreases from 0.3 nm to 0.1 nm as R_{fiber} decreases from 8.8 nm to 1.8 nm. The Poisson's ratio of large fibers is comparable to the Poisson's ratio of a typical glassy polymer of ~0.3. The small nanofibers exhibited Poisson's ratios similar to porous composite materials such as cork (ν~0) and concrete (ν~0.2). The low Poisson's ratio and reduced lateral contraction of the smallest glassy fibers may be partially attributable to the increased volume fraction of the comparatively mobile, mechanically effective surface layer in these nanoscale fibers.

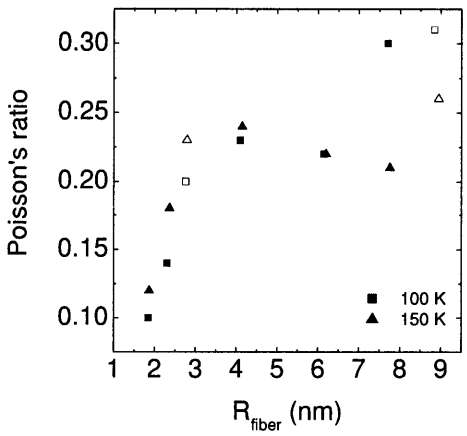

Figure 4.7. Poisson's ratio increases as the fiber radius increases at 100 K and 150 K. Symbols are the same as in Fig. 4.4. Solid symbols represent systems with chain length C100; open symbols represent systems with chain length C150.

4.3.4 Plastic deformation as a function of fiber diameter

Plastic deformation (e.g., yielding and subsequent fracture) of the nanofibers may have important consequences for the mechanical performance of the individual nanofibers, as well as the nonwoven mats comprising such fibers. For this reason, we investigated the large-strain behavior of several nanofibers under uniaxial tension to determine the yield stress and its possible dependence on temperature and fiber diameter.

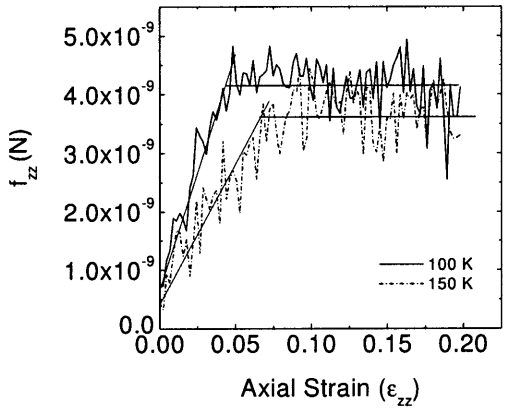

Figure 4.8. Averaged axial force vs. axial strain response for plastic deformation of a fiber (R_{fiber}=4.1 nm at 100K) at 100 K and 150 K at a strain rate of 10^9 s^{-1}.

Figure 4.8 shows such a force-strain response, up to and beyond the onset of plastic deformation. Although the signal-to-noise ratio of the force and strain data points is inevitably low, the applied yield force f_y can be estimated. Yield force is then normalized by the cross-sectional area to compute yield stress σ_y. Figure 4.9 shows yield stress σ_y as a function of fiber radius ranging 40-72 MPa, at 100 and 150 K and a strain rate of 10^9 s^{-1}. For a more direct comparison, we determined σ_y by simulation for an amorphous bulk PE undergoing tensile deformation at a strain rate of 10^9 s^{-1}, and obtained σ_y = 150 and 120 MPa at 100 and 150 K, respectively. This tensile yield stress is approximately 25% lower than that reported by Capaldi et al. for simulated compressive yield strength, using the same force field and comparable strain rates [27]. Vorselaars et al. have also reported

about 25% lower yield stress in tension than in compression for their simulations of a bulk polystyrene glass [41]. Thus, the yield stress for these fibers ranges from one-third to one-half that of the corresponding bulk values; this suggests that the surface layer plays a significant role in facilitating plastic deformation. Finally, although our simulations indicate that the average yield stress increases mildly with increasing fiber radius and decreasing temperature, the error bars associated with identification of the yield point in simulated force-strain responses, particularly for fibers of radii less than 4 nm, preclude identification of size-dependent trends in strength over this range of fiber radii.

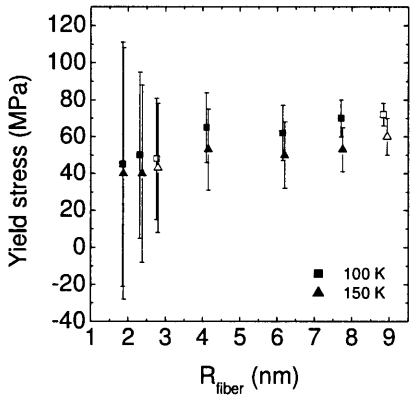

Figure 4.9. Yield stress as a function of fiber radius at 100 K and 150 K determined at a strain rate of 10^9 s^{-1}.

4.3.5 Comparison with experiments

Young's moduli of amorphous PE nanofibers are found to decrease with decreasing fiber radius, which is counter to experimental results available for semi-crystalline and amorphous polymer fibers [7, 18]. However, the experimental fiber diameters for which an increase in E with decreasing fiber diameter has been reported are much larger (e.g., 700 nm for PCL [14]) than the simulated nanofibers (3.7 nm < d < 17.7 nm) presented in

this work. More importantly, to our knowledge, all the nanofibers that were tested experimentally are semi-crystalline, with the notable exception of PS [18], while all our simulated nanofibers are completely amorphous. In one study of PCL nanofibers, crystallinity and molecular orientation were found to increase with decreasing fiber diameter, based on wide angle x-ray scattering experiments and draw ratio calculations, which was correlated in turn with the increase in stiffness of PCL nanofibers with decreasing radius [14]. In contrast, Arinstein et al. reported that crystallinity and orientation in nylon 6,6 nanofibers showed only a modest, monotonic increase [17] that could not be correlated with the dramatic increase in Young's modulus observed with decreasing fiber diameter; the authors concluded that confinement on a supramolecular length scale must be responsible for this increase [17]. In the case of amorphous PS fibers in the range 410 nm < d < 4 μm, the increase in shear elastic modulus was attributed to molecular chain alignment arising from the extensional flow of the electrospinning process itself [18]; as mentioned earlier, our simulated nanofibers do not exhibit any significant molecular level orientation. Thus, while we cannot account for the roles of crystallinity and molecular orientation in the experimental fiber studies, we can infer from our results that the primary consequence of diameter reduction in the smallest fibers (ca. 5-20 nm diameter) is a reduction of elastic modulus, Poisson's ratio and yield stress of these fibers as compared to the bulk counterparts, all of which we attribute to an intrinsically mobile surface layer. Significantly, our results for decreasing stiffness with decreasing fiber diameter are consistent with simulations of nanoscale cantilevered free-standing film [19] and adhered thin film simulations [21] as well as with experiments on adhered thin films of amorphous glassy polymers [25, 26] of comparable (<50 nm) physical dimensions.

Experimentally available measurements of yield strength for PE range between 9.6 MPa and 33.0 MPa at room temperature [39]. However, these measurements are invariably for semicrystalline PE, in which the yield is predominantly due to crystallographic slip along the {100)<001> slip system [40], which is activated at lower stress rather than yield within the amorphous component. Thus, our results are not necessarily inconsistent with the experimental data.

4.4 Conclusions

In Chapter 4, the results of direct MD simulations of the uniaxial loading response for amorphous PE nanofibers are presented. Elastic and plastic properties of individual fibers as a function of fiber radius and temperature were calculated. For a given temperature, the Young's elastic modulus E is found to decrease with fiber radius and can be as much as 52% lower than that of the corresponding bulk material. Poisson's ratio ν of the polymer comprising these nanofibers was found to decrease from a value of 0.3 to 0.1 with decreasing fiber radius. A small but finite stress exists on the simulated nanofibers prior to elongation, attributable to surface tension. When strained uniaxially up to a strain of $\varepsilon = 0.2$ over the range of strain rates and temperatures considered, the nanofibers exhibit a yield stress σ_y between 40 and 72 MPa, which is not strongly dependent on fiber radius; this plastic property is as much as 80% lower than that of the same polyethylene simulated in the amorphous bulk.

Physical and functional properties of nonwoven mats and other fiber-like materials depend strongly on the properties of individual fibers as well as the interactions among adjacent fibers. While Chapters 3 and 4 investigated the structural, thermal and mechanical properties of individual nanofibers as a function of fiber diameter, Chapter 5 deals with the molecular dynamics studies of the interfiber interactions, in order to develop a fiber-fiber interaction model that can be employed in nonwoven mat models.

REFERENCES

[1] Buell S.; Van Vliet K.J.; Rutledge G.C. *Macromolecules* **2009**, *42*, 4887.

[2] Barhate R.S.; Ramakrishna S. *Journal of Membrane Science* **2007**, *296*, 1-8.

[3] Martins A.; Araujo J.V.; Reis R.L.; Neves N.M. *Nanomedicine* **2007**, *2*, 929-942.

[4] Liang D.; Hsiao B.; Chu B. *Advanced drug delivery reviews* **2007**, *59*, 1392-1412.

[5] Yeo L.Y.; Friend J.R. *Journal of experimental nanoscience* **2006**, *1*, 177-209.

[6] Burger C.; Hsiao B.; Chu B. *Annual Review of Materials Research* **2006**, *36*, 333-368.

[7] Wang M.; Jin H.J.; Kaplan D.L.; Rutledge G.C. *Macromolecules* **2004**, *37*, 6856-6864.

[8] Inai R.; Kotaki M.; Ramakrishna S. *Nanotechnology* **2005**, *16*, 208-213.

[9] Bellan L.M.; Kameoka J.; Craighead H.G. *Nanotechnology* **2005**, *16*, 1095-1099.

[10] Tan E.P.S.; Goh C.N.; Sow C.H.; Lim C.T. *Applied Physics Lett.* **2005**, *86*, 073115(1-3).

[11] Tan E.P.S.; Ng S.Y.; Lim C.T. *Biomaterials* **2005**, *26*, 1453-1456.

[12] Chew S.Y.; Hufnagel T.C.; Lim C.T.; Leong K.W. *Nanotechnology* **2006**, *17*, 3880-3891.

[13] Wong S.C.; Baji A.; Leng S. *Polymer* **2008**, *49*, 4713-4722.

[14] Li L.; Bellan L.M.; Craighead H.G.; Frey M.W. *Polymer* **2006**, *47*, 6208-6217.

[15] Shin M.K.; Kim S.I.; Kim S.J.; Kim S.K.; Lee H.; Spinks G.M. *Applied Physics Lett.* **2006**, *89*, 231929(1-3).

[16] Zussman E.; Burman M.; Yarin A.L.; Khalfin R.; Cohen Y. *J. of Poly. Sci. B Poly. Phys.* **2006**, *44*, 1482-1489.

[17] Arinstein A.; Burman M.; Gendelman O.; Zussman E. *Nature Nanotechnology* **2007**, *2*, 59-62.

[18] Ji Y.; Li B.; Ge S.; Sokolov J.C.; Rafailovich M.H. *Langmuir* **2006**, *22*, 1321-1328.

[19] Bohme T.R.; de Pablo J.J. *J. of Chem. Phys.* **2002**, *116*, 9939-9951.

[20] Van Workum K.; de Pablo J.J. *Nano Letters* **2003**, *3*, 1405-1410.

[21] Yoshimoto K.; Jain T.S.; Nealey P.F.; de Pablo J.J. *J. of Chem. Phys.* **2005**, *122*, 144712(1-6).

[22] Vao-soongnern V.; Doruker P.; Mattice W.L. *Macromol. Theory Simul.* **2000**, *9*, 1-13.

[23] Vao-soongnern V.; Mattice W.L *Langmuir* **2000**, *16*, 6757-6758.

[24] Stafford C.M.; Harrison C.; Beers K.L.; Karim A.; Amis E.J.; VanLandingham M.R.; Kim H.C.; Volksen W.; Miller R.D.; Simonyi E.E. *Nature Materials* **2004**, *3*, 545-550.

[25] Stafford C.M.; Vogt B.D.; Harrison C.; Julthongpiput D.; Huang R. *Macromolecules* **2006**, *39*, 5095-5099.

[26] Zhao J.H.; Kiene M.; Hu C.; Ho P.S. *Appl. Phys. Lett.* **2000**, *77*, 2843-2845.

[27] Capaldi F.M.; Boyce M.C.; Rutledge G.C., *Polymer* **2004**, *45(4),* 1391-1399.

[28] Manevitch O.L.; Rutledge G.C. *J.Phys. Chem B.* **2004**, 108, 1428-1435.

[29] Adamson A.W. In *Physical Chemistry of Surfaces,* 3rd ed.; Wiley and Sons: New York, 1976 (Ch 1).

[30] In't Veld P.J.; Rutledge G.C. *Macromolecules* **2003**, *36*, 7358-7365.

[31] In't Veld P.J.; Hutter M.; Rutledge G.C. *Macromolecules* **2006**, *39*, 439-447.

[32] Brandrup J.; Immergut E.H.; Grulke E.A.; Abe A.; Bloch D.R. In *Polymer handbook*, 4th ed.; John Wiley & Sons: New York, 1999.

[33] Capaldi F.M.; Boyce M.C.; Rutledge GC. *Phys. Rev. Lett.* **2002**, *89*, 175505(1-4).

[34] Forrest J.A.; Mattsson J. *Phys. Rev. E* **2000**, *61*, R53-R56.

[35] Fakhraai Z.; Forrest JA. *Science* **2008**, *319*, 600-604.

[36] Peter S.; Meyer H.; Baschnagel J. *J. Phys: Cond. Matter* **2007**, *19*, 2051159 (11pp).

[37] Sharp J.S.; Teichroeb J.H.; Forrest J.A. *Eur. Phys. J. E.* **2004**, *15*, 473-487

[38] Del Gado E.; Ilg P.; Kroeger M.; Oettinger H.C. *Phys. Rev. Lett.* **2008**, *101*, 095501(4 pp).

[39] Avallone E.A.; Baumeister T. III In *Mark's Standard Handbook for Mechanical Engineers,* 10th ed.; McGraw-Hill, 1996.

[40] Kazmierczak T.; Galeski A.; Argon A.S. *Polymer* **2005**, *46*, 8926-8936.

[41] Vorselaars B.; Lyulin A.V.; Michels M.A.J. The *J. of Chem. Phys.* **2009**, *130*, 074905 (14 pp)

CHAPTER 5: DERIVATION OF AN INTERFIBER INTERACTION POTENTIAL

5.1 Introduction

As electrospun nonwoven materials exhibit a particularly high number of fiber-fiber junctions, this interfiber interaction is especially important in determining the macroscopic mechanical properties of such mats. For example, it has been shown that interfiber bonding can be enhanced by controlling the electrospinning process [6] or by post-spinning treatments [7-10] and that this enhancement can improve macroscopic tensile strength and failure strain considerably [8]. Choi et al. showed that the thermal treatment of electrospun poly(etherimide) (PEI) fiber mats leads to interfiber bonding and improved tensile strength [10]. Similarly, the presence of residual solvent in the electrospun polymeric nanofibers may facilitate adhesion between nanofibers in contact and thereby change the mechanical properties of the mat [11-13]. Kidoaki et al. showed that the Young's modulus of segmented polyurethane (SPU) meshes increased with increasing N,N-dimethylacrylamide (DMF) content, when electrospun from a mixed solvent system of tetrahydrofuran (THF) and DMF [13]. These authors attributed the increased mesh stiffness to a higher degree of interfiber bonding, reasoning that the residual content of the slower-evaporating DMF may facilitate entanglement of chains from different fibers at contact points.

One of the challenges in the macroscopic modeling of nonwoven materials is the accurate representation of the fiber-fiber contact interactions. Since the 1950s, several models have been developed, each based on various assumptions of fiber-fiber contact configurations and deformation mechanisms [14-19]. For example, Pan et al. included the effect of interfiber friction and sliding on the mechanical response of fiber assemblies and modeled the compression hysteresis behavior of these assemblies. This model was found to be in reasonable agreement with uniaxial compression experiments of textile treatment wool [14]. Wang et al. showed that simple Euler-Bernoulli beam elements connected by torsion springs at the fiber-fiber junctions can represent the mechanical properties of

fibrous networks successfully [17]. In one effective medium model, the fibers were assumed to be rigidly bonded at each fiber-fiber crossing [18]; in this model, when the network is deformed, the angles between crossing fibers remain constant, and elastic strain is borne entirely in the fiber segments between the crossings. The application of this theory to two-dimensional random fiber networks was found to agree well with results from numerical simulations [18]. In another study, a planar fiber network was represented by a micromechanical model in which the linearly elastic straight rods were bonded rigidly at fiber-fiber contacts [19]. The authors compared the model predictions at several fiber volume fractions with finite element analysis, and found the two to be in good agreement. Chatterjee introduced an energy penalty for rupturing an existing fiber-fiber contact, to calculate the tensile and shear elastic moduli of three dimensional fiber networks [20]. He estimated the strains at the elastic limits under tensile and shear deformation, but did not compare his results with experiments.

Although these models compared favorably against available experiments and/or numerical simulations, the constraints on the fiber-fiber junction interactions were assumed without confirmation by direct experimental measurements or finer-scale simulations. Direct experimental measurements of fiber-fiber interactions are very challenging, particularly for polymeric fibers of sub-micrometer diameter, due to the difficulty of isolating and handling fiber-fiber couples and the uncertainties involved in measuring forces and energies at this scale. Such experimental challenges are not unique to electrospun fiber networks, but arise also in a broad range of systems, including protein filament networks of cytoskeletons in connective tissues and biological cells. To our knowledge, neither theoretical calculation of fiber-fiber interactions nor experimental measurements of such interactions for electrospun materials have been reported previously.

In this chapter, we report a simulation-based analysis of interfiber interactions among nanoscale polymeric fibers, in order to develop fiber-fiber interaction model that can be employed in network calculations.

5.2 Simulation Method

To create polymeric fibers of nanoscale diameter with atomistic detail, we employed MD simulations using a large scale atomic/molecular massively parallel simulator (LAMMPS) [21]. The united atom (UA) force field used in these simulations combines the hydrogen atoms with the carbon to which they are attached into a single "bead"; this model was parameterized by Paul et al. [22] for polyethylene (PE), and later modified by Bolton et al. [23] and In't Veld et al [24]. This is the same force field that we have used previously to characterize the structural, thermal [25] and mechanical [26] properties of individual nanofibers. The details of the functional form and parameters can be found elsewhere [25-26].

A single, free-standing nanofiber was prepared using a two step MD method as we have described previously [25-26]. First, a cubic simulation box containing 30 chains of 100 UA beads (designated C100) was created (total number of monomers N = 3000) and equilibrated in the NVT ensemble at 495 K, such that the polymer density was 0.75 g/cm^3. Then the simulation box was cooled to 100 K through a succession of NPT ensembles with a constant, isotropic pressure of P=10^5 Pa. This temperature is lower than both the glass transition temperature (T_g) of the same material (united atom C100) in the bulk state, which has been estimated to be 280 K [27], and the T_g of the surface layer of a single C100 nanofiber, which we have previously estimated to be 150 K [25]. Next, the box dimensions were increased simultaneously in two perpendicular directions (i.e., x and y), such that the molecules can no longer interact with their images in these directions. Thus, the periodic boundary condition applied only in one direction, the z-direction, which was then parallel by definition to the fiber axis. This simulation cell was then equilibrated in an NVT ensemble at 100 K, resulting in spontaneous formation of a cylindrically symmetric object, representing a repeating segment of an amorphous nanofiber of infinite length. The radius of the nanofiber thus created was calculated to be R_{fiber} = 2.3 nm, using the Gibbs dividing surface method [25]. For the purposes of this study, only a single fiber radius was considered so that multiple simulation approaches and parameters could be compared.

Two distinct approaches, MD and MS (also called "energy minimization"), were then considered to construct interfiber interaction energy functionals $U[s]$ over a range of separation distances, s. For both simulation approaches, the total potential energy of the system was calculated by addition of bond, angle, torsional and Lennard-Jones energies between united atoms. Note that here we reserve U for interaction energy and E for total potential energy.

To characterize interfiber interactions via MD, we constructed a system comprising two C100 nanofibers, each prepared as described above and then placed in the same simulation box such that the axes of the fibers were parallel and separated by a prescribed distance, s (Figure 5.1a). Here $s=s(r_1^{3N}, r_2^{3N})$ is defined by the distance between the centers of mass (COM) of the two fibers, which in turn are computed from the 3N coordinates of the united atoms initially assigned to each fiber; we considered ten different interfiber distances over the range 1 nm < s < 11 nm. Figure 5.1b shows the initial configuration of the simulated system at a separation distance of s = 7 nm. To maintain each interfiber distance constant, the momentum of the COM of each nanofiber was fixed via the "fix momentum" command in LAMMPS. While this method does not affect the relative motion of the atoms within either nanofiber, it ensures that the COM's of the two nanofibers remain at the initial separation distance throughout the entire simulation duration. The system was then equilibrated in the NVT ensemble at 100K for 300 ns. These MD simulations thus provide estimates of $E(t)$, $E[s]$, and $U[s]$ for conditions under which thermally activated motion is sampled over sufficient time to permit reconfiguration of chains within and between fibers.

In addition, we also performed MS or energy minimizations of the same two-fiber system, with the same constraint on separation distance s. The purpose of the interfiber MS simulations was to establish $U[s]$ in a manner that did not impose constraints on the fiber positions, but also minimized thermally activated interactions. The same two-fiber simulation box setup was used as in the MD interfiber simulations, with nanofibers positioned parallel to the long axis at an interfiber distance that ranged 1 nm < s < 11 nm.

The energy minimization algorithm iteratively adjusted atomic coordinates to lower the system energy, and iterations were terminated when the configuration attained a local potential energy minimum of magnitude and tolerance within 0.01 J/mol UA. In order to sample more two-fiber systems and thus obtain better statistics on calculated energies, several initial configurations were generated by rotating one of the fibers about its z-axis by 10^{o} increments.

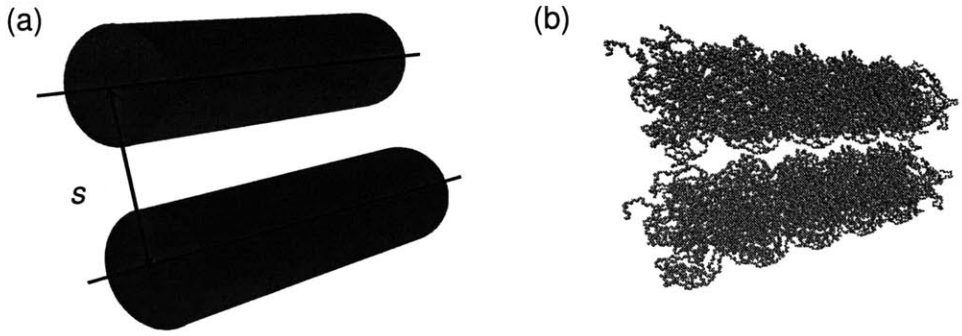

Figure 5.1 (a) Schematic representation of the fiber-fiber simulation system. (b) Visual Molecular Dynamics (VMD) image of the fiber-fiber simulation setup at interfiber distance s = 7 nm. Five periodic images in the axial direction are connected for clarity (R_{fiber} = 2.3 nm at 100 K).

5.3 Results from Molecular Dynamics Simulations

5.3.1 Potential energy profiles at different separation distances

The total potential energy E(s) of the fiber-pair systems was used to calculate the interaction energy between the nanofibers as a function of separation distance U(s). Figures 5.2a and 5.2b show the change in total potential energy as a function of time, $E(t)$, for the MD simulations at s = 2, 5, 7, and 9 nm. Potential energy profiles at s = 3, 4, 6 and 8 nm follow trends similar to those shown in Figure 5.2a, and are omitted for clarity. Potential energy profiles at s =10 nm superpose the data obtained at s = 9 nm in Figure 5.2b.

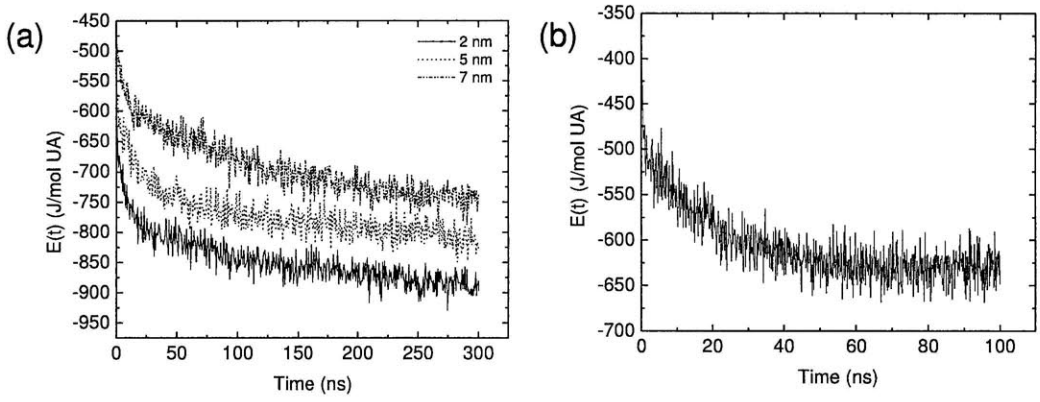

Figure 5.2 MD simulations of system potential energy for two-fiber equilibration trajectories at 100 K. (a) Potential energy vs. time for separation distances of s = 2, 5, and 7 nm indicate an initial fast decay followed by a slower decay that persists for hundreds of ns. (b) Potential energy vs. time for s = 9 nm indicates equilibration within 100 ns.

During a typical MD trajectory, the potential energy $E(t)$ initially decreases rapidly due to fast rectification of unfavorable contacts, and then continues to decline more slowly. Once a local or global equilibrium is attained, $E(t)$ fluctuates around an average, constant value. As Figure 5.2a shows, the potential energy of the nanofibers at 1 nm < s < 9 nm continued to decrease very slowly over the entire course of the 300 ns MD simulation. For $s \geq$ 9nm, the systems reached equilibrium within approximately t ~ 50 ns, after which potential energy fluctuates less than 12% around an average value of -627 J/mol UA. The time it takes for an MD simulation of such polymeric systems to equilibrate depends on several factors, including molecular weight and temperature; however, these fiber-fiber simulations were run under identical molecular weight and temperature conditions. The separation distance determines the degree of interaction between the fibers at early times, and can affect the time required for the fiber-fiber system to reach a local energetic minimum [28]. Since the fiber radius (as defined by the Gibbs dividing surface) is 2.3 nm, the fibers overlap significantly at s = 2, 3, and 4 nm. Furthermore, the surfaces of nanofibers are finite in thickness; the interfacial thickness, defined here as the distance over which the density of the fiber decreases from 90% to 10% of the bulk value, is 1.4 nm, so that the density of polymer segments is significant out to a distance from the fiber core of ~3.0 nm. Even so, the position of individual segments of chains may fluctuate to

distances even further from the fiber axis, due to thermal motion. Due to these fluctuations, fibers can communicate even for values of s as large as 8 nm, which presumably accounts for the long equilibration times. For $s > 9$ nm, no interaction between the fibers was observed (as defined by molecular overlap between chains from distinct fibers over the simulated trajectories) and the system reached a local energetic minimum within 50 ns.

5.3.2 Radial density and cross-sectional shape profiles

We calculated the radial density profiles (details of this calculation can be found elsewhere [25]) of one fiber within our MD simulations at different s, in order to analyze structural changes of the fiber at the molecular level (Figure 5.3a). The density profile of a single, separately equilibrated fiber is also given in Figure 5.3a, as a reference point to emphasize the differences in density profiles due to interfiber interactions.

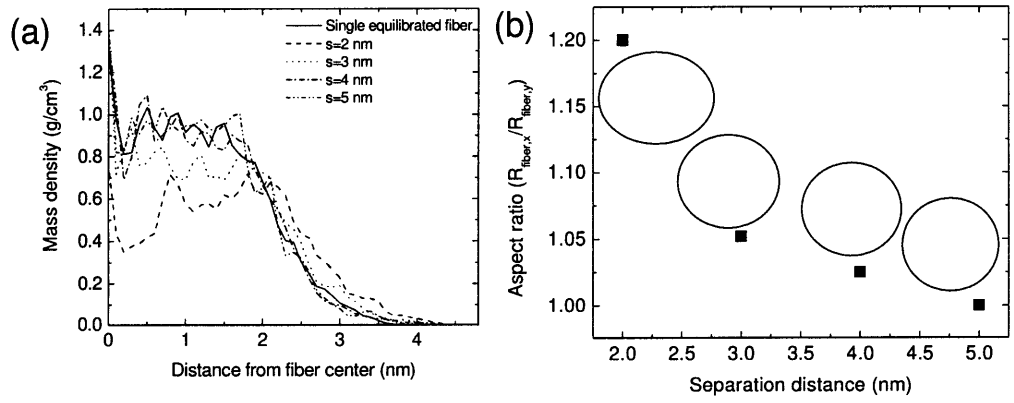

Figure 5.3 (a) Mass density profile of an equilibrated single nanofiber, as compared with the mass density profile of one of the fibers in fiber-fiber MD simulations at different separation distances s. (b) Aspect ratio for one of the fibers in MD simulations at 100 K vs. separation distance shows that the cylindrical symmetry is distorted when a second fiber is placed adjacent to an initially cylindrical nanofiber. The ellipses are representative of simple cross-sections corresponding to the aspect ratio of each datum.

In the case of a single, isolated fiber, the density is constant and highest within the core of the fiber and equal to ~0.9 g/cm^3. In contrast, in the case of two fibers at a separation distance s = 2 nm, the region of highest density is displaced towards the surface of the fibers. Furthermore, this density is lower than in the case of the isolated fiber, at ~0.6 g/cm^3; a similar trend is observed at s = 3 nm. At s = 4 and 5 nm, the mass density profiles are similar to that of an isolated single fiber. The distortion of the density profiles at s=2 and 3 nm are indicative of significant overlap of the two fibers, which necessitates displacement of the chains, on average, away from the COM of each fiber. The cylindrical symmetry of each fiber is disrupted.

Figure 5.3b shows the ratio of major and minor axes ($R_{\text{fiber,x}}$ and $R_{\text{fiber,y}}$, respectively) for the cross-section of one fiber, called the aspect ratio as a function of separation distance, s. Fiber cross-sections become increasingly elliptical for decreasing separation distances. This change in fiber shape is also demonstrated graphically in Figure 5.3b, where ellipses are drawn to scale to represent the aspect ratio at each separation distance. The aspect ratio is the largest (~1.2) at s = 2 nm, where distortion of the mass density profile is greatest.

The changes in both the density and shape profiles suggest that the macromolecular chains tend to intermix from one fiber to another, leading to a constrained coalescence (because s is fixed to be nonzero) of the two fibers. Since the chains are chemically and structurally "identical" in the two fibers, this coalescence can be understood as a consequence of the tendency to reduce the total the surface energy of the system, in a manner analogous to particle sintering and microstructural coarsening in nonpolymeric materials [29].

The change in cross-sectional profile is also demonstrated in Figure 5.4a, which shows a contour plot of mass density for this fiber-pair in cross-section for s = 2 nm. Figure 5.4b compares the radial mass density profile of one of the initial, single nanofibers (R = 2.3 nm) to that of the larger fiber formed by partial coalescence of two such nanofibers. This radial mass density illustrates that the density of macromolecular chains at both the

single-fiber and fiber-pair cores are comparable within 300 ns of simulation; however, the distance from the core over which this high density extends is naturally greater for the larger, partially coalesced fiber-pair. Although this coalesced fiber-pair is not cylindrical in cross-section, an estimate of the effective radius obtained by the GDS method is 3.4 nm. This estimate will assist in comparison of the limits of interaction energy in the model discussed below.

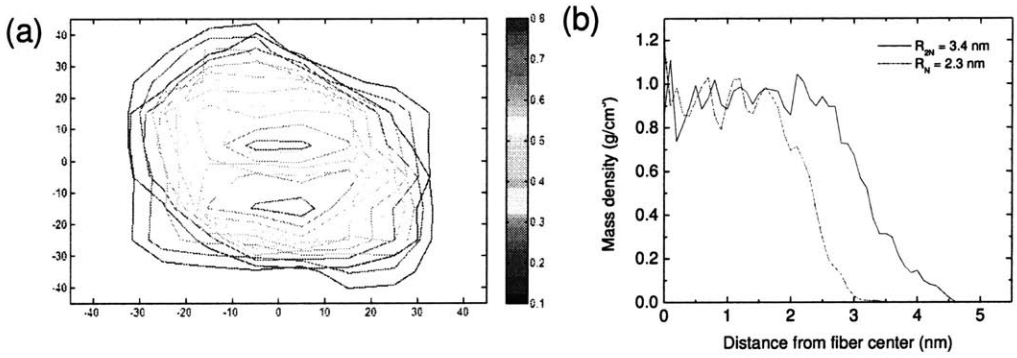

Figure 5.4 (a) Contour plot of mass density for this fiber-pair in cross-section for s = 2 nm, obtained from averaged trajectories over 300 ns of MD simulation. (b) Radial mass density profile of one of the partially coalesced fiber-pair extends over greater distances from the core than that of a fiber in the isolated state (R = 2.3 nm).

At this point, it is worth remarking on the slow decay of energy over a period of 100's of nanoseconds observed in Fig 5.2a, for cases where $s < 9$ nm. The energy $E(t)$ at any time t is higher for systems with larger s, since the constraint on the separation distance between the fiber COM's implies a final equilibrium configuration that is increasingly distorted from being circular in cross-section, and thus higher in surface energy; only a system in which the constraint on s is completely released could the system completely rearrange to form a single, larger fiber. Nevertheless, it seems remarkable that such a decay is observed at all on the time scale of these simulations, in light of the fact that the temperature of simulation (100 K) was chosen to lie well below not only the glass transition of the core of the fiber (280 K), but also that previously determined to be characteristic of the surface of the fiber (150 K) [25].

We interpret this relaxation as evidence for a small but more mobile fraction of material at the outer periphery of the fibers, which remains highly dynamic, even at very low temperature. To view the differences between the dynamics of bulk and interfacial regions, we calculated the residence times of individual atoms. (Figure 5.5b) The fibers are divided into cylindrical shells (i.e. bins) of 0.5 nm width, starting from the center of the fiber. (Figure 5.5a) The circular grids in this figure, which are numbered from 2 to 7 (bin 1 is the black circle in the middle), represent the bins; color coded same as the data that is plotted in Figure 5.5b. Only 10% to 15 % of the atoms starting out in bin 1 (the bulk region) move out of their original at s=2, 6 and 9 nm. A similar trend is observed at other separation distances (data not shown). In contrast, the percentage of atoms that moves out of bin 6 is significantly larger at s=6 and 9 nm than at s = 2 nm. This might be due in part to most of the surface being an interface with the other fiber at s = 2 nm. On the other hand, at s = 6 and 9 nm, the atom positions fluctuate sufficiently to exit and re-enter this surface region.

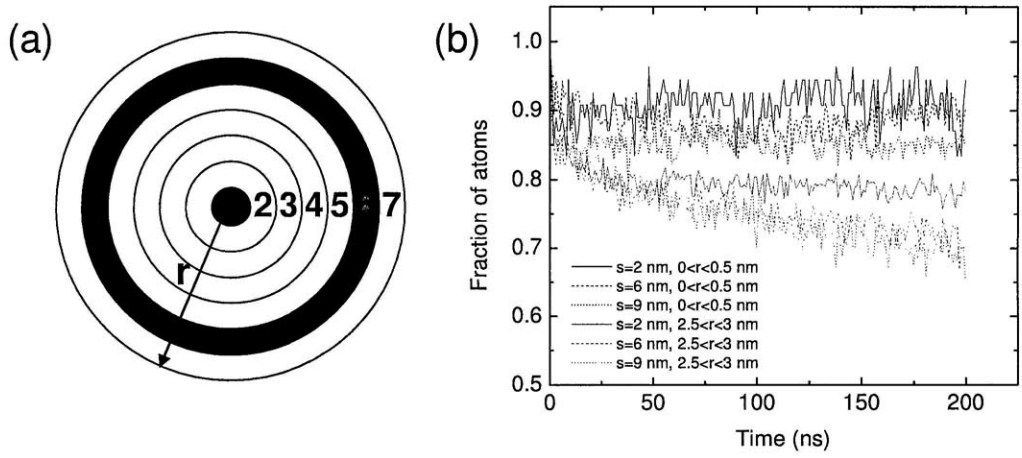

Figure 5.5 (a) Circular grids, which are numbered from 2 to, 7 represent the bins. (b)Fraction of atoms which stay in their original bin, as a function of time and the separation distance s. Black lines correspond to bin 1 ($0< r <0.5$ nm) and red lines correspond to bin 6 ($2.5< r <3$ nm).

Taken together, this data indicates that the degree of molecular mobility is the highest at the fiber surface compared to the fiber core. This is consistent with our previous studies on these fibers describing effective T_g in terms of a simplified layer model with a surface region of higher molecular mobility [25]. Also, as the bin number increases, the residence time of atoms in their original bin decreases. This merely serves as a reminder that the fiber surface is actually a gradient material, with dynamical behavior that varies throughout its width from that of a vitrified solid to that of a low density melt. As the size scale of the material (e.g. a fiber) is reduced to the nanoscale, this more mobile surface fraction becomes increasingly important. Even for these 4.6 nm diameter fibers, however, complete relaxation of the fiber-pair system mediated by this molten surface fraction is too slow to follow to completion, requiring times in excess of 3 months of simulation on a single 2.66 GHz dual-quad core in LAMMPS.

5.3.3 Interaction model for MD results

From these MD simulations, we can summarize the interaction between two fibers by comparing the energies of the two-fiber system to that of single, isolated fibers. Figure 5.6a shows the potential energy per mole of united atom (mol UA) as a function of $s^* = s/2R$, the separation distance normalized by the diameter of the fibers, $2R$ = 4.6 nm. For any given snapshot of simulation time longer than about 50 ns (the single fiber equilibration time), this potential energy varies smoothly between that of an isolated fiber with R = 2.3 nm (the upper bound marked E_N, where the linear density N/L=3000/4.3 nm, or 1.6×10^{-8} tex) at large distances and that of an isolated fiber with R=3.4 nm, having twice this linear density (the lower bound marked E_{2N}). With increasing simulation time, these potential energy data shift downward, with little change in shape of the variation between E_N and E_{2N} (*c.f.* the data in Figure 5.6 at t = 200 ns and 300 ns). To obtain the interaction energy $U(s^*)$, we subtract E_N from the total potential energy of the fiber-pair system at each s^* (Figure 5.6b).

On the basis of these observations, we construct a mathematical function that describes the interaction $U(s^*)$ between two nanofibers as a function of their normalized separation distance. The form of the interaction is well-described by the logistic function:

$$U\left(s^*\right)=U_0+\left(U_\infty-U_0\right)\left[1+\exp\left(-\frac{s^*-s_0^*}{\sigma}\right)\right]^{-1} \tag{5.1}$$

where s^*_0 and σ serve to translate and rescale, respectively, the independent variable s^*, while U_0 and $(U_\infty - U_0)$ serve to translate and rescale, respectively, the dependent variable $U(s^*)$. Here, energy tends to U_0 as s^* tends to 0 (full coalescence) and to U_∞ as s^* goes to $+\infty$ (distant, non-interacting fibers). The inflection point of this interaction energy is located at s^*_0, while σ is sometimes called the "steepness parameter". The form of this function predicts that within a certain (small) distance of approach, two fibers will experience a force driving them into contact, with a work of adhesion on the order of $(U_\infty - U_0)$. However, here we do not report fitted parameters of the fit from our MD simulation data, as Fig. 5.6b makes clear that the system has not yet attained the equilibrium state which this function aims to describe; that state would span the physical limits U_0 and U_∞ over these simulation timescales.

These limiting energetic values are not arbitrary results of fits to MD simulations of fiber-pairs, but in fact can be related directly to the surface energy. We have previously shown that the energy of an isolated fiber, even at such small diameters, is well-described by the following equation:

$$E_N = E_{bulk} + \gamma\left(2\pi R_N L\right)N_A/N \tag{5.2}$$

where N/L is the number of UA per unit length L of fiber, R_N is the radius of the fiber, E_{bulk} is the molar energy density of UA in the bulk amorphous phase 102 J/cm^3 at 100 K and γ is the surface energy (~45 mJ/m^2 [25]), which is more or less independent of fiber radius. This surface energy is also in agreement with an experimental estimate of 44.7

mJ/m^2 for amorphous PE at 100 K [30]. When two fibers of radius R_N merge completely to form a single, larger fiber of radius R_{2N}, the change in energy is predicted by continuum mechanics to be:

$$\Delta E = E_{2N} - E_N = \frac{\pi L N_A \gamma}{N}\left(R_{2N} - 2R_N\right) \tag{5.3}$$

Substituting the values reported above for N/L, γ, R_{2N} and R_N, we obtained ΔE=-290 J/mol UA, which is about similar in magnitude to $(U_\infty - U_0)$ = -273 J/mol UA. Thus, the work of adhesion for fiber-fiber contacts by this approach is consistent with the change in energy due to a reduction in total surface area.

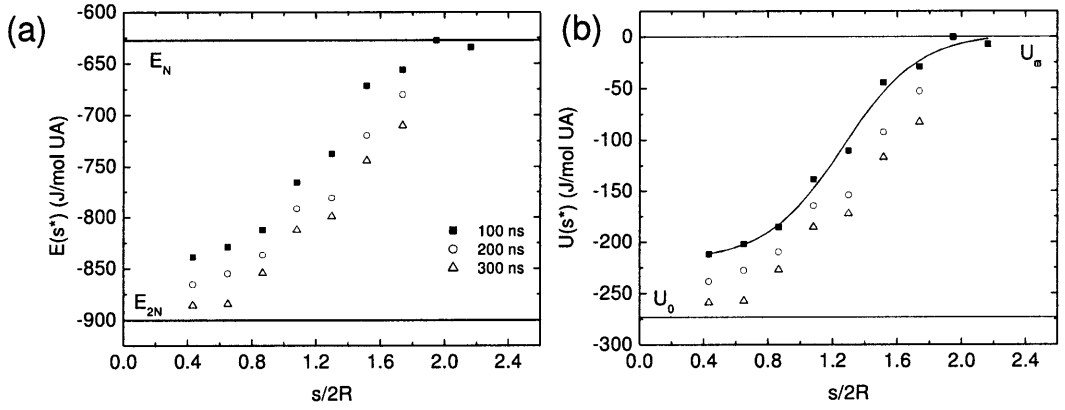

Figure 5.6 (a) Potential energy per mole of united atoms for the fiber-pair system as a function of separation distance s, normalized by the diameter of the fibers $2R$. Each data symbol corresponds to the energy $E(t)$ extracted from the simulations at different times: 100 ns (filled squares), 200 ns (open circles), 300 ns (open triangles) . The upper and lower horizontal lines are limits for isolated fibers of radius R_N and R_{2N}, respectively. (b) Interaction energy per mole of UA as a function of s^*, where $E_N(t)$ is subtracted from $E(t)$. Symbols indicate the same time points as in (a). The solid curve illustrates the best fit of the sigmoidal form given by Eq. (5.1) to the simulation data at 100 ns; see text for details.

5.4 Results from molecular statics (MS) simulations

5.4.1 Interaction model for MS simulations

We have used a conjugate gradient method [21] to run energy minimizations (MS) of the same fiber-pair systems as those discussed above for MD simulations. Figure 5.7a shows the potential energy as a function of separation distance, averaged over an ensemble of 36 systems at each s^*. For all separation distances $s \geq 7$ nm, the potential energy is approximately equal to the total energy of two non-interacting fibers, and can be taken as E_∞ for this set of calculations. Subtracting E_∞ from the total potential energy, we obtain the static interaction energy, $U(s^*)$, for static fibers (Figure 5.7b). At $s = 6$ nm, there is an attractive energy well depth of approximately 26.5 J/mol UA; for $s < 6$ nm, the force of interaction between static fibers is repulsive, in stark contrast to the results for dynamic fibers from MD simulations. Interestingly, $s = 6$ nm corresponds to a separation distance slightly larger than s^*_0, where the density of polymer segments is still significant. The range of attractive interaction is narrow (extending ~1 nm), indicating a short-range attraction between nanoscale fibers.

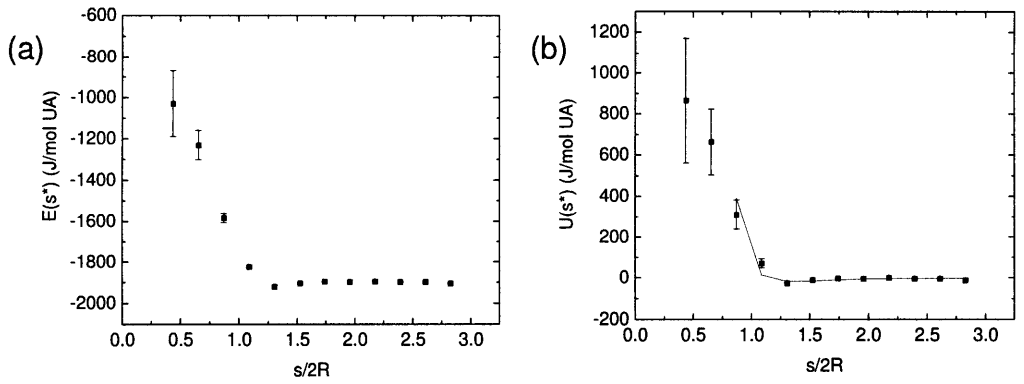

Figure 5.7 (a) Total potential energy as a function of separation distance $E(s^*)$ calculated from energy minimizations. (b) Net interaction energy as a function of separation distance $U(s^*)$, obtained by subtracting the energy for two non-interacting fibers, E_∞, from $E(s^*)$ (see text for details). Data points represent the simulation results and the solid line is the best fit to the simulation data using eq (4).

In contrast to the MD simulations of fiber-pairs, the interaction energy as a function of separation distance obtained by molecular statics is reminiscent of classical pair potentials between particles. We considered several such forms, and found best agreement with the data using a Mie type interaction potential with (n,m) = (8,4):

$$U(s^*) = A(s^*)^{-8} - B(s^*)^{-4} \tag{5.4}$$

For the data in Figure 5.7b, A = 200 J/mol UA and B = 125 J/mol UA. As Figure 5.7b shows, equation 5.4 can successfully predict the interaction energy of fibers for s > 3 nm. At s = 2 and 3 nm, this model overpredicts the repulsion energy at s/2R < 0.7 by two orders of magnitude, and thus is not shown in Fig. 5.7b. (Many variations of the Mie potential, as well as other forms such as piecewise exponential decays, were considered; none of those other forms better captured both the trends at small s and the depth and curvature of the energy minimum at s ~ 6 nm.) The form of Eq. (5.4) thus summarizes the interaction potential between two fibers up to the point at which the fiber radii defined by the GDS begin to intersect (here, for s < 4 nm). Physically, this corresponds to separation distances of significant overlap between the chains in adjacent nanofibers that extend beyond the GDS.

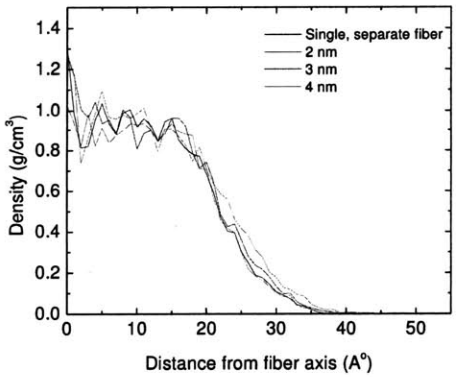

Figure 5.8 Mass density profile of an equilibrated single nanofiber, as compared with the mass density profile of one of the fibers in fiber-fiber MS simulations at different separation distances s.

Similar to Figure 5.3.a, we also calculated the radial density profiles of one fiber within our MS simulations at different s, in order to analyze structural changes of the fiber. The density profile of a single, separately equilibrated fiber is also given in Figure 5.8, as a reference point. As it can be seen from this figure, the density profiles of the fibers do not change significantly during the MS simulations and resemble the density profile of a single, separately equilibrated fiber.

5.5 Discussion

Both MD simulations and MS calculations indicate that there exists a short-ranged attractive interaction between fibers that extend out to a distance s of $3R$ to $4R$. However, where MD predicts an eventual coalescence of the nanofibers with a significant work of adhesion, energy minimization results predict that the interaction between fibers becomes repulsive for smaller separation distances. The difference between these two results can be understood to result from the action of dynamical relaxation processes on the MD time scale in the dynamic simulations. There is both a simulation-specific rationale and a physical parallel for these differing perspectives. While MD approach enables exploration of dynamics, energy minimization emphasizes configuration-based energetics. Yin and Boyd have previously estimated that the time scale of the γ relaxation below T_g for a UA model of C768 in the bulk state is on the order of 32 μs [32], far longer than our MD simulations here. However, a mobile surface fraction of PE-like chains may relax much faster; estimates of the Rouse time for a UA model of C100 above its T_g are on the order of 2.5 ns [33], well within the timescale of these simulations.

In physical experiments involving electrospun polymeric fibers, each simulation perspective can be realized. If the fibers are in contact with each other and their surfaces are sufficiently mobile (analogous to the MD simulations), they will tend to coalesce. This is in agreement with the experimental results of interfiber "welding" when electrospun nonwoven materials are laid down "wet" or annealed at high temperature or in the presence of a plasticizing agent or solvent: the role of temperature or solvent in this

case is to increase the mobile surface fraction so that a significant consolidation of the fibers at the point of contact can be achieved [7-10]. In contrast, the molecular statics results are representative of the more conventional case where the contacts between fibers are strictly "solid-like". In such cases, there is a weak, short-ranged attractive interaction between fibers. As the diameter of fibers in contact is reduced, the relevance of the mobile surface fraction, with its shorter time scale of relaxation, becomes more important, and one anticipates that a transition from the static, solid-like contact picture to the dynamic, cohesive contact picture may be observed. While the fiber size and simulation times are necessarily very short, compared to most electrospun fibers and experimental observations, we think that this may motivate further studies to explore the size-dependent nature of fiber-fiber interactions in nonwoven materials.

5.6 Conclusions

Previous studies of nonwoven materials modeling [14-19] have employed several different forms of interfiber interactions, without measuring or predicting these interactions at the molecular level. Here we have studied the interfiber interactions by two distinct simulation methods, in order to develop a quantitative understanding and prediction of interfiber interaction energies. We propose two interfiber potentials constructed directly from atomistic simulations of individual nanofiber pairs. The resulting formulae capture trends from MD simulations (eq 5.1) and energy minimization simulations (eq 5.4) for nanoscale polymer fibers. Both perspectives find reasonable analogy with specific experimental conditions that have been realized for electrospun polymer nanofiber-based materials, and point toward future experiments and models that will exploit these interactions. These equations can now be used to represent the interfiber interactions accurately in nonwoven material models. Further, the comparison among these approaches suggests the need for new experiments and models to explore the critical timescales of interfiber interactions in polymeric systems at the nanoscale.

REFERENCES

[1] Barhate, R.S.; Ramakrishna, S. *Journal of Membrane Science* **2007**, *296*, 1.

[2] Martins, A.; Araujo, J.V.; Reis, R.L.; Neves, N.M. *Nanomedicine* **2007**, *2*, 929.

[3] Liang, D.; Hsiao, B.; Chu, B. *Advanced drug delivery reviews* **2007**, *59*, 1392.

[4] Yeo, L.Y.; Friend, JR. *Journal of experimental nanoscience* **2006**, *1*, 177-209.

[5] Burger, C.; Hsiao, B.; Chu, B. *Annual Review of Materials Research* **2006**, *36*, 333.

[6] Zong, X.; Ran, S.; Fang. D.; Hsiao, B.S.; Chu, B. *Polymer* **2003**, *44*, 4959.

[7] Choi, S.S.; Lee, S.G.; Joo, C.W.; Im, S.S.; Kim, S.H. *J. Mater Sci.* **2004**, *39*, 1511.

[8] Young, Y.; Lee, S.W.; Lee, S.J.; Park, W.H. *Materials Lett.* **2006**, *60*, 1331.

[9] Lee, S.J.; Oh, S.H.; Liu, J.; Soker, S.; Atala, A.; Yoo, J.J. *Bimaterials* **2008**, *39*, 1422.

[10] Choi, S.; Lee, S.G.; Joo, C.W.; Im, S.S.; Kim, S.H. *J. of Materials Sci.* **2004**, *39*, 1511.

[11] Lee, K.H.; Kim, H.Y.; La, Y.M.; Lee, D.R.; Sung, N.H. *J Poly. Sci. Poly. Phys.* **2002**, *40*, 2259.

[12] Krishnappa, R.V.N.; Desai, K.; Sung, C. *J. Mater. Sci.* **2003**, *38*, 2357.

[13] Kidoaki, S.; Kwon, K.; Matsuda, T. *J. Biomed. Mater. Res. Part B: App. Biomater.* **2005**, *76B*, 219.

[14] Pan, N.; Carnaby, G.A. *Textile Research Journal* **1989**, *59*, 285.

[15] Komori, T.; Itoh, M. *Textile Research Journal* **1991**, *61*, 420.

[16] Narter, M.A.; Batra, S.K ; Buchanan, D.R. *Proc. R. Soc. A.* **1999**, *455*, 3543.

[17] Wang, C.W.; Berhan, L.; Sastry, A.M. *J Eng. Mater. Tech.* **2000**, *122*, 450.

[18] Astrom, J.A.; Makinen, J.P.; Alava, M.J.; Timonen, J. *Phys Rev E* **2000**, *61*, 5550.

[19] Wu, X.F.; Dzenis, Y.A. *J. Appl. Phys* **2005**, *98*, 093501(1-9).

[20] Chatterjee, A.P. *J Appl. Phys* **2006**, *100*, 054302(1-8)

[21] Plimpton, S. *J. Comput. Phys.* **1995**, *117*, 1.

[22] Paul, W.; Yoon, D.Y.; Smith, G.D. *J Chem Phys.* **1995**, *103*, 1702.

[23] Bolton, K.; Bosio, S.B.M.; Hase, W.L.; Schneider, W.F.; Hass, K.C. *J Chem Phys B* **1999**, *103*, 3885.

[24] In't Veld, P.J.; Rutledge, G.C. *Macromolecules* **2003**, *36*, 7358.

[25] Curgul, S.; Van Vliet, K.J.; Rutledge, G.C. *Macromolecules* **2007**, *40*, 8483.

[26] Buell, S.; Van Vliet, K.J.; Rutledge, G.C. *Macromolecules* **2009**, *42*, 4887.

[27] Capaldi, F.M.; Boyce, M.C.; Rutledge, G.C. *Polymer* **2004**, *45*, 1391.

[28] Walton E.B.; Van Vliet K.J. *Phys. Rev. E* **2006**, *74*, 061901(1-8).

[29] Pan J.Z. *Int. Mater. Rev.* **2003**, *48*, 69.

[30] Brandup J.; Immergut EH; Grulke EA; Abe A; Bloch DR In *Polymer Handbook*, 4th ed.; John Wiley & Sons: New York, **1999**.

[31] Nocedal J.; Wright S.J. In *Numerical Optimization*, 2nd ed.; Springer-Verlag: New York, **2006**.

[32] Jin Y.; Boyd R.H. *J. Chem. Phys.* **1998**, *108*, 9912.

[33] Harmandaris V.A.; Mavrantzas V.G.; Theodorou D.N. *Macromolecules* **1998**, 31, 7934.

CHAPTER 6: MODELING OF NONWOVEN MATS

6.1 Introduction

Nanostructured fibrous materials have been made more readily available in large part owing to recent advances in electrospinning. When deposited as a nonwoven mat, the resulting fabrics are highly porous; they have a large interconnected void volume in the range of 50% to even greater than 90% and possess one of the highest surface-to-volume ratios among all cohesive porous materials. The entangled fibrous geometry has a pseudo-bicontinuous structure; the pore volume is essentially continuous and interconnected. Due to these topological features of the porous space, electrospun nanofibrous materials have gained rapid popularity in many applications [1-5]. Hence, to obtain detailed information on the properties of these fibrous networks is extremely important and has been the subject of many studies [6-23]. Many of these previous studies of modeling porous and fibrous media have focused exclusively on the pore interconnectivity (for porous media used, e.g., in catalysis or sorption studies) or the fiber arrangement (for fibrous media used, e.g., in mechanical studies).

On the other hand, fibrous networks are more commonly modeled as arrangements of rigid geometric objects, with attention paid to the contacts or interaction between these objects in studies that have investigated fiber modeling for other purposes such as fiber flocculation or fiber behavior in flow [24-30]. For example, Melrose and Ning [30] developed a numerical method for simulating mechanical behavior of flexible fibers. A circular crossed fiber is represented by a number of cylindrical segments linked by a spring dash-pot systems. Segments are lined up and bonded to each neighbor. They do not consider interactions between non-neighboring segments. Computer simulation has been conducted to verify the single fiber model with elastic theory and excellent agreements have been found between the simulation results and the theory in various situations such as beam deflection under static loads, vibrating cantilevers, and dynamics of helical shaped fibers.

In this chapter a model that is similar to that used by Melrose and Ning [30] is employed to generate a range of nonwoven structures, with different fiber orientation distributions. Our aim is to lay the groundwork for generating nonwoven mats whose important characteristics (e.g. fiber orientation, porosity, fiber diameter) match the electrospun mats that are prepared in the lab.

6.2 Monte Carlo (MC) simulation methodology

6.2.1 Model

In our model, the fibers were represented by a number of cylindrical segments. (Figure 6.1) Here R is the radius of each cylindrical segment, d_0 is the initial length of each cylindrical segment and L is the total length of the fiber. These segments were lined up and bonded to each neighbor at the ends, which is denoted as junctions in Figure 6.1. Each bond can be stretched or compressed by changing the bond distance. Bending deflection and twist movement occured respectively by changing the bending and torsion angles. The flexibility was obtained by changing the material and geometrical properties of the segments in stretching, bending and twisting. This modeling way is analogous to that of molecular dynamics method in respect that a molecule is constructed from atoms by bonding each other.

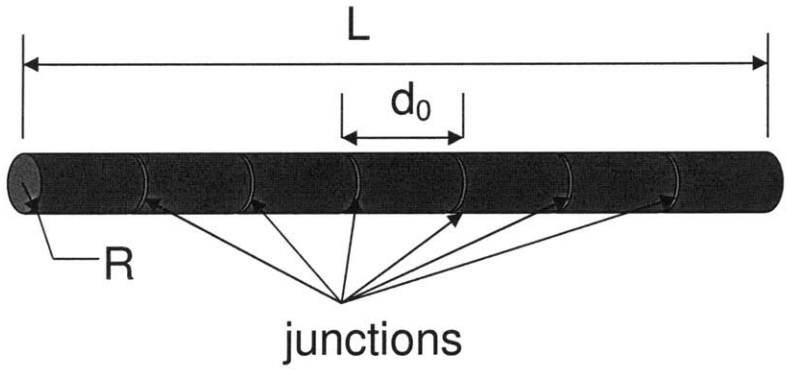

Figure 6.1 Schematic representation of a single, straight fiber

We assumed the elastic beam theory to represent the energy change associated with different types of movement. According to the elastic beam theory, the energy of an elastically stretched (or compressed) beam is equal to

$$\Delta U_{stretch/compress} = \frac{EA}{2d_0}(d - d_0)^2 \tag{6.1}$$

where E is the Young's modulus of each of the cylindrical segments, A is the cross-sectional area and d is length of the cylindrical segment after stretching (or compression). Similarly, the energy of an elastically bent and twisted beam can respectively be written as

$$\Delta U_{bend} = \frac{EI}{2d_0}(\theta - \theta_0)^2 \tag{6.2}$$

$$\Delta U_{twist} = \frac{GI_p}{2d_0}(\phi - \phi_0)^2 \tag{6.3}$$

where $I = \pi R^4/4$ is the moment of inertia, $\theta_0 = 0$ is the equilibrium angle between 2 cylinders, θ is the angle after the cylindrical segments are bent, G is the shear modulus, $I_p = \pi R^4/2$ is the polar moment of inertia, $\Phi_0 = 0$ is the equilibrium twist angle and Φ is the twisting angle after the segments are twisted.

Since we were working on the interfiber interaction potential derivation using MD simulations (Chapter 5) and the MC model simultaneously, we did not have the results for a more accurate description of the fiber pair interactions. Thus, as a first estimation, the interactions between individual fibers were represented by a hard cylinder potential, which can be written as,

$$\Delta U_{inter}(r) = \begin{cases} +\infty, & s < 2R \\ 0, & s > 2R \end{cases} \tag{6.4}$$

where s is the separation distance between the centers of the cylinders. This type of interaction prevents the fibers from physically crossing each other (therefore avoids unphysical overlaps) but does not define a specific interaction (e.g. attractive, repulsive) for fibers with $s > 2R$. The results given below were obtained by using equation 6.4. However, the model is flexible in the sense that other interfiber interaction potential functions, including the ones suggested by the MD simulations (as described in more detail in Chapter 5), can be incorporated.

We used dimensionless quantities where all parameters are scaled either by the length scale R (radius of each cylindrical segment in m) and the energy scale ER^3 (E is the modulus of each cylindrical segment in N/m^2). The dimensionless total energy change of a single cylindrical segment can then be represented as

$$\Delta U^*_{segment} = \frac{\frac{EA}{2d_0}(d-d_0)^2 + \frac{EI}{2d_0}(\theta-\theta_0)^2 + \frac{GI_p}{2d_0}(\phi-\phi_0)^2 + \Delta U_{inter}}{ER^3} \tag{6.5}$$

Similarly, we can write down the dimensionless total energy change of the whole system by plugging in A, I and I_p and dividing by ER^3

$$\Delta U^* = N \cdot \frac{L}{d_0} \cdot \left\{ \frac{\pi}{2} \frac{(d-d_0)^2}{d_0 R} + \frac{\pi(\theta-\theta_0^2)}{8} \frac{R}{d_0} + \frac{\pi(\phi-\phi_0^2)}{4} \frac{G}{E} \frac{R}{d_0} \right\} \tag{6.6}$$

where N is the total number of fibers in a simulation box and L/d_0 is the number of cylindrical segments per fiber (i.e. aspect ratio of the fiber).

6.2.2 Simulation procedure

We used Monte Carlo simulations to generate the nonwoven structures. In general, the MC method is a stochastic method which generates configurations of a given system within a particular ensemble. It provides no information on the trajectories and velocities

of particles. In an atomistic Monte Carlo simulation, for a NVT ensemble, the probability of accepting an event is given by

$$p_i = \exp(-\Delta U/kT) \tag{6.7}$$

where ΔU is the energy change associated with that event and kT is the thermal energy, which is the energy scale that determines the possibility of molecular events.

However, in our MC algorithm, the thermal energy was not the relevant energy scale since our goal was to simulate continuum objects rather than molecules. Therefore, we defined a dimensionless stochastic energy, T^*, which can be calculated from

$$T^* = S/ER^3 \tag{6.8}$$

where S is a parameter (a "pseudo-energy") with units of J. By using T^*, in case of the continuum MC model, the probability of an event is proportional to the following exponential function

$$P_i \propto \exp(-\Delta U^*/T^*) \tag{6.9}$$

where ΔU^* is the non-dimensional total energy change that is calculated from Equation 6.6. According to this formulation, at low "temperature", the ensemble will be dominated by random arrangements of essentially rigid fibers; at higher "temperature", the ensemble will be enriched by contributions from flexible, coiling fibers.

All the simulations were run in NVT ensemble (where the volume of the simulation box and the number of fibers were kept constant) and for durations of $1x10^5$ MC cycles. The Monte Carlo moves employed include site translation, end rotation and reptation. In the site translation move, the coordinates of a junction were changed by a random displacement such that the total length change (d-d_0) and/or the total angle change (θ-θ_0)

did not exceed 1%, which is within the elastic deformation limit of polymeric materials. In the end rotation move, the twisting angle Φ at a randomly selected fiber end was perturbed by a random amount within a range whose maximum was set to 1%. In the reptation move, a junction was removed from one end of a chain and appended to the other end of the same chain, while keeping d and θ constant. The new twisting angle Φ was perturbed from the old one by a random value whose maximum was set to 1%.

4 different fiber volume fractions, 5%, 10%, 15% and 20% were simulated since the electrospun nonwoven mats that are prepared in the lab are 80% to 95% porous.

6.3 Results

6.3.1 Nonwoven mats from flexible and rod-like nanofibers

When we look at equation 6.6, we can see that the aspect ratio of the fiber (L/d_0), aspect ratio of each cylindrical segment (d_0/R) and the ratio of shear modulus to Young's modulus (G/E) are the important variables that determine the energy change of the system. A systematic study of these variables is required to explore the limits of the MC model. However, in an attempt to investigate the model behavior, we simulated the nonwoven systems with the parameters given in Table 6.1. As d_0/R gets smaller, the number of energy calculations increases, requiring longer simulation times. On the other hand, as d_0/R gets larger, the fiber aspect ratio becomes closer to d_0/R, resulting in a coarser calculation of the fiber configurations. Therefore, as a first approximation, we set d_0/R to 2 and L/d_0 to 49, which provided a reasonable number of configurations in a practical amount of simulation time. Also, we set the shear modulus G to $0.3\times E$ assuming a Poisson's ratio of 0.3 which is typical of an amorphous polymer. Figures 6.2, 6.3 and 6.4 show the results from these simulations. In these figures, the volume fraction of the fibers in the simulation box is 15%, R is equal to 1×10^{-6} m and the system has been simulated using 3 different values of E: 10^4, 10^6, and 10^8 N/m^2 (while S is kept constant) respectively. Similar results were obtained for other volume fractions, which are not shown here.

Variable	Non-dimensional value
N	100
d_0/R	2
L/d_0	49
G/E	0.3
T*	10, 10^{-1}, 10^{-3}

Table 6.1 Representation of a nonwoven system in dimensionless quantities

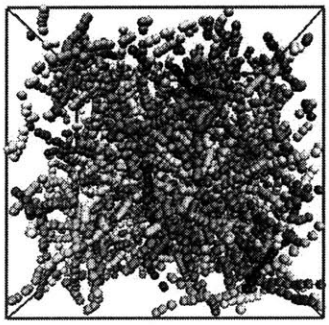

Figure 6.2 Representation of the nonwoven system with $T^* = 10$

As it can be seen from these figures, by using the MC model and the parameters given in Table 6.1, we can generate nonwoven mat structures with different fiber structures (i.e., flexible or rod-like) and orientations (i.e., random vs. aligned). While Figures 6.2-6.4 represent the type of nonwoven structures that can be generated by using this method, several other structures can be created by changing the parameters in Table 6.1. Indeed, a thorough study of the variables is required to help us understand the strength of the analogy between the MC generated mats and experimentally prepared mats.

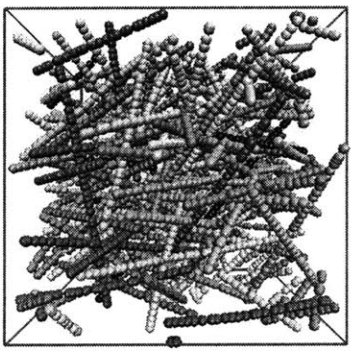

Figure 6.3 Representation of the nonwoven system with $T^* = 0.1$

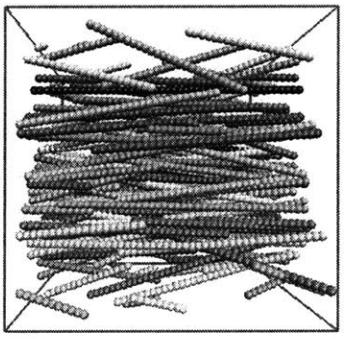

Figure 6.4 Representation of the nonwoven system with $T^* = 0.001$

6.3.2 Parametric analysis example: Effect of T^* on the fiber orientation of nonwoven mats

The importance of the several dimensionless parameters (i.e. L/d_0, R/d_0 and G/E) has been discussed in the previous section. T^* is another dimensionless parameter that directly affects the acceptance criteria of the MC moves. Therefore, in this section, we investigate the effect of T^* on the fiber orientation of nonwoven mats in order to illustrate parametric analysis.

To quantify the fiber orientation, we calculate the order parameter tensor from

$$T_{ij} = \left\langle v_i v_j - \frac{1}{3}\delta_{ij} \right\rangle \tag{6.10}$$

where v_i (i=1, 2 and 3) denote the Cartesian coordinates of unit vector that lies in the direction of the vector connecting junction i-1 to i+1 and the averaging is performed over all the fibers. T_{ij} matrix can be diagonalized and its eigenvalues are $2/3\eta$, $-1/3\eta$ and $-1/3\eta$. "η" is the order parameter and equivalent to the second Legendre polynomial coefficient P_2, which is equal to 1 when the fibers are aligned along a certain direction and equal to 0 when the fibers do not have preferred orientations.

Figure 6.5a shows the effect of T^* on the order parameter for different volume fractions of nonwoven mats. These mats were simulated using the parameters given in Table 6.1. As it can be seen from this figure, we observe randomly distributed straight, rod-like fibers when $T^* > 0.1$. For $T^* < 0.1$, the orientation parameter starts to increase, which is an indication of fiber alignment. The order parameter is close to 1 and the fibers are aligned along a certain direction for $T^* < 0.005$. Figure 6.5b is the semi-log plot of Figure 6.5a and was plotted in order to show the effect of volume fraction on the order parameter more clearly. As it can be seen from Figure 6.5b, the mats with higher fiber volume concentration start to align at slightly larger T^* values.

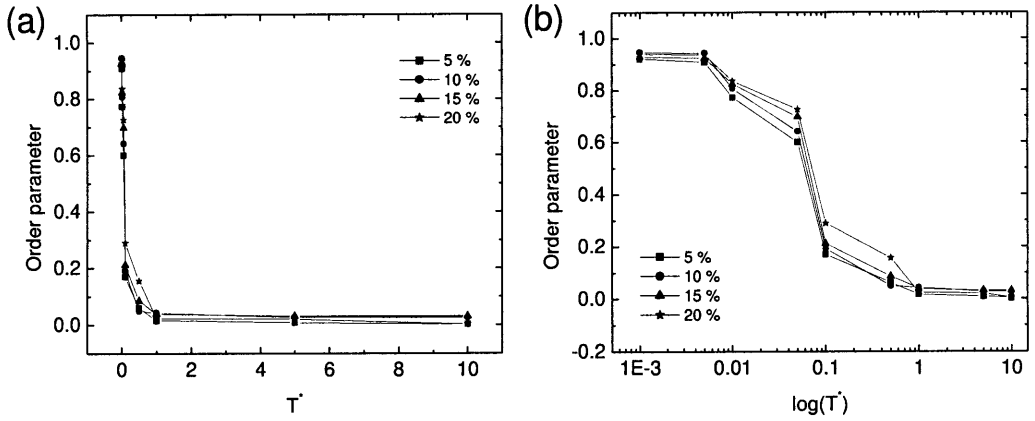

Figure 6.5 (a) Order parameter vs. T^* for the nonwoven system simulated with parameters given in Table 6.1. (b) Order parameter vs. log(T^*) plot for the same nonwoven system.

6.4 SEM image analysis

6.4.1 Image analysis algorithm

To analyze the scanning electron microscope (SEM) images of the electrospun nonwoven mats, we employed an algorithm based on the orientation of simple neighborhoods proposed by Jahne [31]. This algorithm enabled us to quantify fiber orientation distributions of the experimentally prepared nonwoven mats. The algorithm was implemented in a Matlab code by Dimitrios Tzeranis from the So Bioinstrumentation Lab at MIT. In summary, the algorithm calculates a structure tensor, J_{pq}, which is a first order representation of a local neighbourhood and can be written as

$$J_{pq}(x) = \int_{-\infty}^{+\infty} w(x-x') \left(\frac{\partial g(x')}{\partial x'_p} \frac{\partial g(x')}{\partial x'_q} \right) d^W x' \tag{6.11}$$

where w is a window function that determines the size and shape of the neighborhood around a point x in which the orientation is averaged and g is the gradient vector that represents the gray value changes in the image. Analytical solution to equation 6.11 in two dimensions results in an eigenvalue problem, which can be shown as

$$Je_w = \lambda_w e_w \tag{6.12}$$

An eigenvector e_w of the matrix J is thus a vector that is not turned in direction by multiplication with the matrix J but is only multiplied by a scalar factor, the eigenvalue λ_w. This implies that the structure tensor becomes diagonal in a coordinate system that is spanned by the eigenvectors. According to the maximization problem formulated here, the eigenvector to the maximum eigenvalue gives the orientation of the local neighborhood. The solution to equation 6.12 yields the orientation angle as

$$\tan 2\theta = \frac{2J_{12}}{J_{22} - J_{11}} \tag{6.13}$$

The algorithm also calculates cohesion, which is given as

$$c = \frac{\sqrt{(J_{22} - J_{11})^2 + 4J_{12}^2}}{J_{11} + J_{22}} \tag{6.14}$$

Cohesion is a measure which is used to distinguish between a constant gray area (i.e. oriented structures but maybe the window size is too small) and an isotropic gray value structure without preferred orientation. While a cohesion value equal to 1 represents ideal local orientation, a cohesion value of 0 represents isotropic gray value structure. The details of this digital image processing algorithm can be found elsewhere [31].

6.4.2 Orientation distribution from Nylon6(3) nonwoven mats

The algorithm, which is described above, was used to analyze the fiber orientation distributions from SEM images that are similar to the ones shown in Figures 6.6a, 6.7a, 6.8a and 6.9a. There are two user inputs to this algorithm: The "block size", which sets the size of the window function and "gamma", which controls the visibility of the image. Or in other words, gamma is a parameter which adjusts the intensity values in grayscale image. A block size of 2 pixels was used for SEM images with a magnification of x1000 and 4 pixels was used for SEM images with a magnification of x2000. These values were chosen such that the cohesion value (which is explained above) is close to 1 which enabled us to calculate local orientation and indicated that the window size is correct for the magnification of the image. (i.e. We did not zoom into the image too much to miss the local orientation). A gamma value (which can range from 0 to 1) of 0.7 was used for all images since same adjustment for the intensity of the grayscale image was desired.

The fiber orientation histograms (Figures 6.6b, 6.7b, 6.8b and 6.9b) were then calculated by averaging several SEM images taken from different samples. The electrospun mats that are shown in these images were electrospun from a solution of 35 wt% Nylon6(3)t/DMF by Chia-ling Pai from Rutledge group at MIT. In the aligned samples, the fibers were aligned by collecting the fibers on a rotating drum during electrospinning. The average diameter of Nylon6(3) nanofibers was measured to be ~ 0.5×10^{-6} m [32]. Young's modulus of a single Nylon6(3) nanofiber was measured to be 4 GPa [32]. The porosity of the these electrospun Nylon6(3) mats were calculated to be ~10-12% [32].

As it can be seen from fiber orientation histograms, even though the SEM images do not show it clearly, the nanofibers are oriented at the desired angles. For the random Nylon6(3) mats, which is shown is Figure 6.9, even though some alignments seem to be more probable than the others, this can be an artifact of the larger magnification of the SEM samples (the magnification for random mat data is x2000 while it's x1000 for aligned mat data) as well as the insufficient number of SEM samples analyzed. Even though we used a larger window size to compensate for the larger magnification of this

set of images, the number of fibers (analyzed for orientation) in images with x2000 magnification was significantly smaller than the number of fibers in images with x1000 magnification. Thus, the statistics was not as good as the x1000 data to demonstrate the overall randomness of the mats.

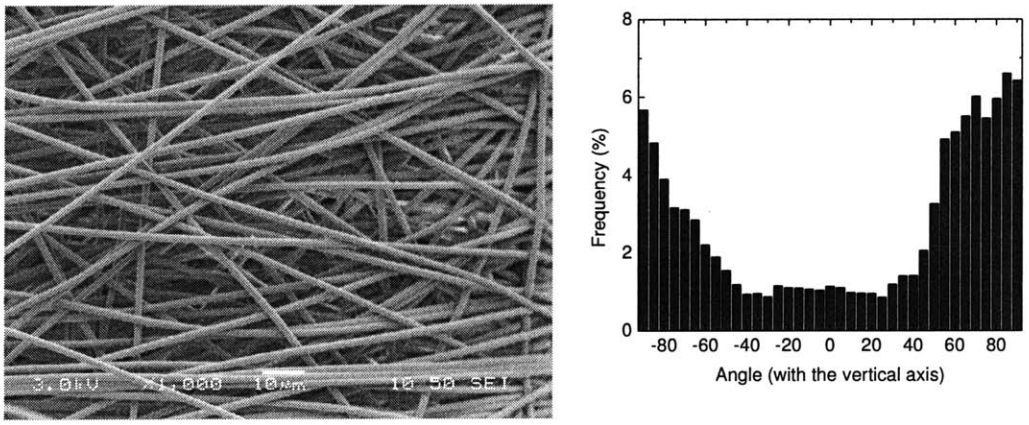

Figure 6.6 a)SEM image of horizontally aligned Nylon6(3) nanofibers. b) Fiber orientation histogram of horizontally aligned Nylon6(3) nanofibers, which is calculated by averaging 15 SEM images that are similar to the one in part a.

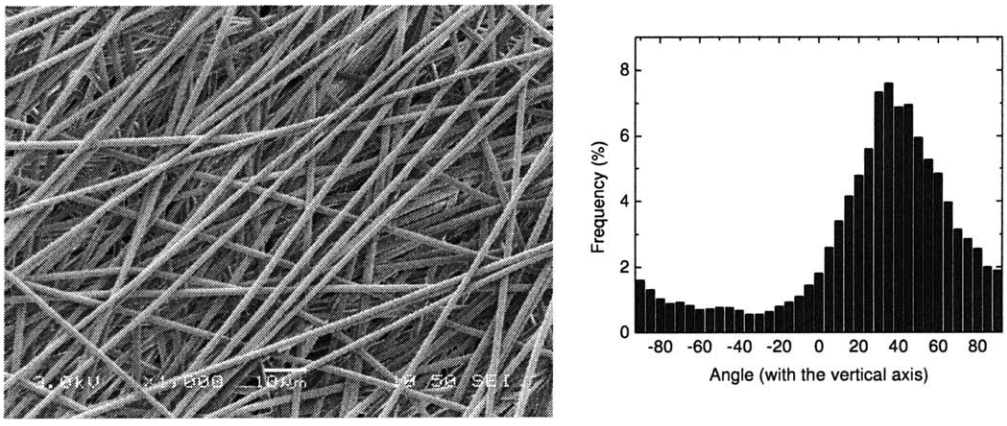

Figure 6.7 a)SEM image of Nylon6(3) nanofibers that are aligned 45° to horizontal direction. b) Fiber orientation histogram of 45° aligned Nylon6(3) nanofibers, which is calculated by averaging 17 SEM images that are similar to the one in part a.

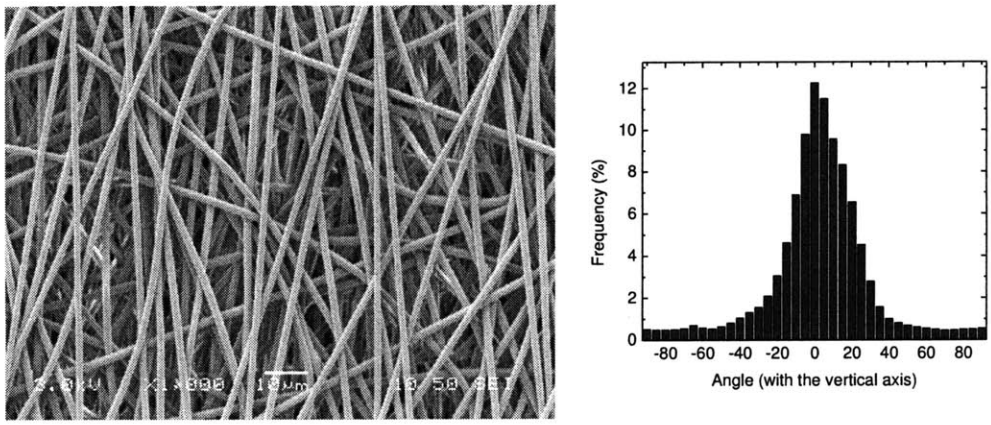

Figure 6.8 a)SEM image of vertically aligned Nylon6(3) nanofibers. b) Fiber orientation histogram of vertically aligned Nylon6(3) nanofibers, which is calculated by averaging 14 SEM images that are similar to the one in part a.

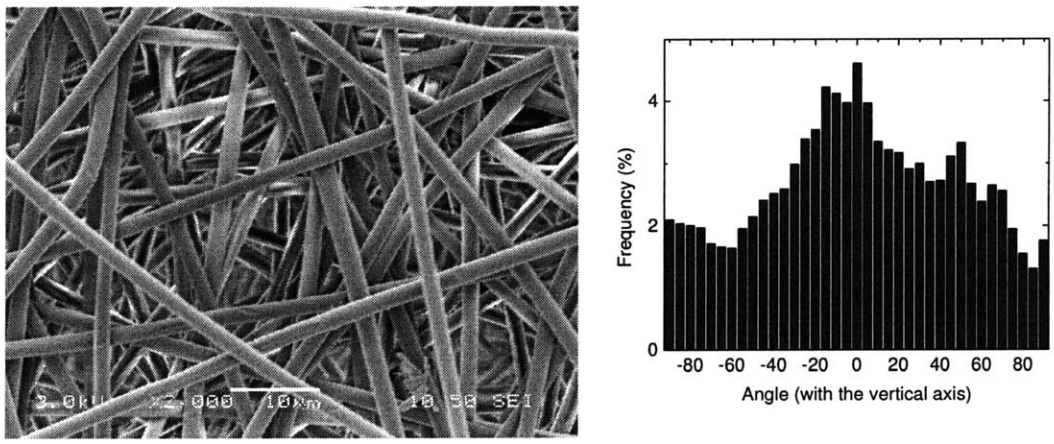

Figure 6.9 a)SEM image of random Nylon6(3) nanofibers. b) Fiber orientation histogram of random Nylon6(3) nanofibers, which is calculated by averaging 10 SEM images that are similar to the one in part a.

6.4.3 Property match example: Comparison of fiber orientations with experimental mats

In an effort to demonstrate how the properties of MC generated mats can be matched to the experimentally prepared mats, in this section, we calculate the fiber orientations of the MC model generated mats and compare them with the Nylon6(3) electrospun mats.

We generated nonwoven systems with N = 100, d_0/R = 2, L/d_0 = 49, G/E = 0.3, R = 2.5×10^{-7} m and $E = 4\times10^9$ N/m^2 for several T^* values. These parameters were chosen to match the properties of the Nylon6(3), which are given in the previous section.

Figure 6.10 shows the order parameter as a function of log(T^*) at 10% volume fraction of fibers. Images of the nonwoven mats are also given to show how orientation is changing as T^* is altered. Similar plots can be created for different fiber volume fractions. As it can be seen from these images and the orientation parameter plot, we observe randomly dispersed rod-like fibers for $5 \leq T^*$. For $T^* \leq 5$ the fibers start to align and the fibers are aligned along one direction for $T^* \leq 0.05$.

In Figure 6.10, the order parameter was calculated from equation 6.10. Since alignment of the vector connecting junction i-1 to i+1 was measured in this calculation, the distance over which this calculation was made can be estimated as 1×10^{-6} m for a straight fiber (Figure 6.11a). On the other hand, the fiber orientations for Nylon6(3) mats were calculated from SEMs which are 256 pixels (~130×10^{-6} m) long on one side (Figure 6.11b). As mentioned above, a window size of 2 pixels was chosen as the input parameter; resulting in a distance of ~ 1×10^{-6} m over which the fiber orientation is calculated (Figure 6.11b). Since both of these orientation calculations were carried out on the same local length scale, we can compare the MC model generated nonwoven mats with the experimental samples. As we can see from Figure 6.10, we can generate random rod-like fibers as well as fibers aligned along a certain direction (and other intermediate structures), just like the Nylon6(3) mats. In this way, MC model is promising in

generating nonwoven mats whose fiber orientations match with the real electrospun nonwoven mats.

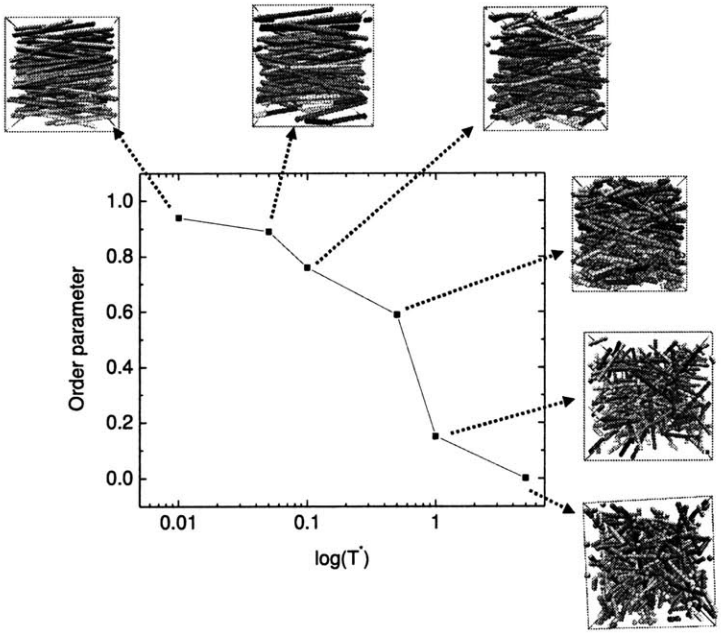

Figure 6.10 Order parameter vs. log(T^*) for MC model generated nonwoven mats with parameters $N = 100$, $d_0/R = 2$, $L/d_0 = 49$, $G/E = 0.3$, R = 2.5×10^{-7} m and $E = 4\times10^9$ N/m^2 shows that a range of fiber orientations (from completely random to aligned in 1-D) can be attained.

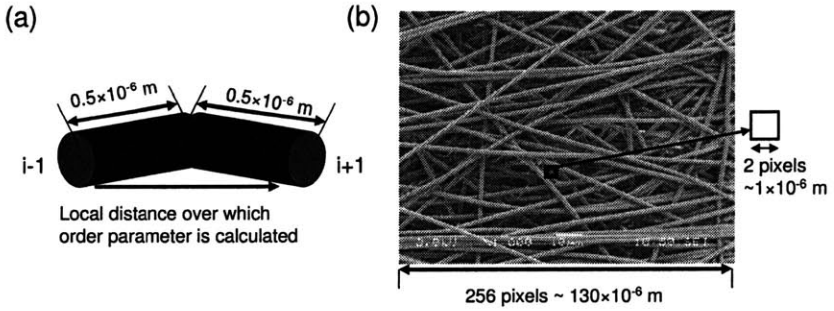

Figure 6.11 (a)The distance over which orientation parameter was calculated can be estimated as 1×10^{-6} m for a straight fiber. (b) A window size of 2 pixels was chosen as the input parameter in section 6.4.2; resulting in a distance of ~ 1×10^{-6} m over which the fiber orientation is calculated for Nylon6(3) mats.

6.5 Conclusions

We used direct stochastic Monte Carlo simulations to generate nonwoven mat structures that consist of nanofibers. In our novel MC model, that the fibers are comprised of several short cylinders which act like elastic beams. The interactions between different fibers are represented by a hard cylinder potential (equation 6.4) which prevents unphysical overlaps. As mentioned above, since we have recently finalized the derivation of an interfiber interaction potential using molecular scale simulations (Chapter 5), we have not yet implemented it in the MC model. However, the MC model is set up such that this kind of interactions can be easily incorporated. These interactions are very important in determining the mechanical properties of the nonwoven mats since they control how the load is transferred from one fiber to another. Therefore, implementation of different types of interfiber interactions (like the ones defined by equations 5.1 and 5.4) would enable a detailed study of the mechanisms by which the nonwoven mats deform at the nanofiber level.

The MC simulation algorithm is set up such that the acceptance probability of MC moves depends on both the pseudo energy (S) and fiber properties (E, R). Above S was presented as an arbitrary parameter but it can actually be associated with the energy put into the system during processing (from the start of the process when the polymer solution is charged to the end of the process when the elongated jet is collected in different forms including random mats and well-aligned fibers). If energy input into the system (e.g. electrical energy spent to charge the polymer solution, the energy required to rotate the drum if the liquid jet is being collected on a rotating drum to align the fibers) for different processing conditions can be calculated, a correlation between S and processing parameters (such as voltage applied or viscosity of the polymer solution) can be derived. This would enable a direct relationship between experimental and modeling parameters. Up to our knowledge, none of the existing nonwoven models are capable of this.

Using this model, several nonwoven structures with different fiber orientations, fiber structures and fiber volume fractions have been successfully generated. An example of parametric analysis was given in order to show how the model parameters affect the generated nonwoven structures. The model would greatly benefit from similar parametric analysis of different dimensionless variables (e.g., L/d_0, R/d_0, G/E) in order to explore the model capabilities and limits.

Finally, fiber orientation distributions from SEM images of electrospun mats were compared with the fiber orientations of MC generated mats, to illustrate how the model generated mats can be realistic representations of the experimental samples. In this way, MC model is promising in generating nonwoven mats whose fiber orientations match with the real electrospun nonwoven mats.

The work presented in this chapter constructs the basis for future studies of the nonwoven mat generation and properties. Once the model capabilities and limits are thoroughly investigated, many relevant and experimentally verifiable properties of the nonwoven materials can be quantified.

REFERENCES

[1] Barhate R.S.; Ramakrishna S. *Journal of Membrane Science* **2007**, *296*, 1-8.

[2] Martins A.; Araujo J.V.; Reis R.L.; Neves N.M. *Nanomedicine* **2007**, *2*, 929-942.

[3] Liang D.; Hsiao B.; Chu B. *Advanced drug delivery reviews* **2007**, *59*, 1392-1412.

[4] Yeo L.Y.; Friend J.R. *Journal of experimental nanoscience* **2006**, *1*, 177-209.

[5] Burger C.; Hsiao B.; Chu B. *Annual Review of Materials Research* **2006**, *36*, 333-368.

[6] Abdel-Ghani M.S.; Davies G.A. *Chemical Engineering Science* **1985**, *40*, 117.

[7] Jerauld G.R.; Hatfield, J.C.; Scriven L.E.; Davis H.T. *Journal of Physics C* **1984**, *17*, 1519.

[8] Winterfeld P.H.; Scriven L.E.; Davis H.T. *Journal of Physics C* **1982**, *14*, 2361.

[9] Mason G. *Proceedings of the Royal Society Lond. A* **1988**, *415*, 453.

[10] Seaton N.A. *Chemical Engineering Science* **1991**, *46*, 1895.

[11] Portsmouth R.L.; Gladden L.F. *Chemical Engineering Science* **1991**, *46*, 3023.

[12] Constantinides G.N.; Payatakes A.C. *Chemical Engineering Communication* **1989**, *81*, 55.

[13] Tsakiroglou C.D.; Payatakes A.C. *Journal of Colloidal Interface Science* **1991**, *146*, 479.

[14] Mayagoitia V.; Cruz M.J.; Rojas F. Journal *of Chemical Society Faraday Transactions* **1989**, *85*, 2071.

[15] Cruz M.J.; Mayagoitia V.; Rojas F. *Journal of Chemical Society Faraday Transactions* **1989**, *85*, 2079.

[16] Mayagoitia V.; Rojas F.; Kornhauser I.; Zgrablich G.; Faccio R.J.; Gilot B.; Guiglion C. *Langmuir* **1996**, *12*, 211.

[17] Mayagoitia V.; Rojas F.; Kornhauser I.; Perez-Aguilar H. *Langmuir* **1997**, *13,* 1327.

[18] Ramirez-Cuesta A.J.; Cordero S.; Rojas F.; Faccio R.J.; Riccardo J.L. *Journal of Porous Materials* **2001**, *8*, 61.

[19] Cordero S.; Rojas F.; Riccardo J.L. *Colloids and Surfaces A* **2001**, 187-288, 425.

[20] Armatas G.S.; Pomonis P.J. *Chemical Engineering Science* **2004**, *59*, 5735.

[21] Androutsopoulos G.P.; Salmas C.E. *Industrial and Engineering Chemical Research* **2000a**, *39*, 3747.

[22] Androutsopoulos G.P.; Salmas C.E. *Industrial and Engineering Chemical Research* **2000b**, *39*, 3764.

[23] Schmid C.F.; Switzer L.H.; Klingenberg D.J. *Journal of Rheology* **2000**, *44*, 781.

[24] Sampson W.W. *The Science of Papermaking,* Trans. XIIth Fund. Res. Symp. **2001**, 1205.

[25] Yamamoto S.; Matsuoka T. *Poly. Eng. Sci.* **1995**, *35*, 1022-1030.

[26] Yamamoto S.; Matsuoka T. *J. Chem. Phys.* **1995**, *102*, 2254-2260.

[27] Yamamoto S.; Matsuoka T. *J. Chem. Phys.* **1993**, *98*, 644-650.

[28] Ross R.F.; Klingenberg D.J. *J. Chem. Phys.* **1997**, *106*, 2949-2960.

[29] Skjetne P.; Ross R.F.; Klingenberg D.J. *J. Chem. Phys.* **1997**, *107*, 2108-2121.

[30] Ning Z.M.; Melrose J.R. *J. Chem. Phys.* **1999**, *111*, 10717-10726.

[31] Jahne B. In *Digital Image Processing*; Springer: New York, 2005.

[32] Unpublished data, measured by Chia-ling Pai, Rutledge group.

CHAPTER 7: CONCLUSIONS AND DIRECTIONS FOR FUTURE RESEARCH

7.1 Thesis summary

This thesis focused on developing the necessary modeling tools to understand and describe the structural, thermal and mechanical properties of polymer nanofibers and interactions between such nanofibers. Another focus of this work was to construct a framework for a novel simulation technique that incorporates individual nanofiber properties and inter-fiber interactions, to generate realistic nonwoven structures and to establish a quantitative connection between nanoscale features and nonwoven properties.

The first focus of this thesis was to study the size-dependent properties of amorphous polymer nanofibers using molecular simulations. For this, we used molecular dynamics methods. The fibers consist of chains that mimic the prototypical polymer polyethylene, with chain lengths ranging between 50 and 300 carbons (C50 to C300). These nanofibers have diameters in the range 1.9 to 23.0 nm, as determined by GDS method. We analyzed these nanofibers for signatures of emergent behavior in their structural and thermal properties as a function of diameter. The mass density at the center of all fibers is constant and comparable to that of the bulk polymer. The surface layer thickness, which is defined as the distance over which the mass density of the fiber decreases from 90% to 10% of the corresponding bulk value, ranges from 0.78 to 1.39 nm for all fibers and increases slightly with fiber size. The interfacial excess energy is calculated to be 0.022 ± 0.002 J/m^2 for all of the nanofibers simulated and no size-dependence was found for this property. The chains at the surface are found to be more confined as compared to the chains at the center of the nanofiber; the latter acquire unperturbed dimensions in sufficiently large nanofibers. Consistent with experiments and simulations of amorphous polymer films of nanoscale thickness, the glass transition temperature of these amorphous nanofibers are found to decrease with decreasing fiber diameter, and is independent of molecular weight over the range considered.

We used the same molecular dynamics techniques to investigate the emergent mechanical properties of these amorphous, polyethylene nanofibers. We found that the elastic mechanical properties (i.e., Young's modulus E) are dependent on the fiber diameter at a given temperature. We reported E for fibers of diameter less than 10 nm can be as much as 52% lower than that of the corresponding bulk material. This physical phenomenon was described in terms of a two layer model, which is similar to composite material model, for which the surface of the fiber has different mechanical properties than the center of the fiber. We also studied the plastic deformation of the same nanofibers by straining them up to and beyond their elastic limit. We found that the yield stress can be as much as 80% lower than that of the same polyethylene simulated in the amorphous bulk. Our findings also indicate that a small but finite stress exists on the simulated nanofibers prior to elongation. This was attributed to surface tension and was explained in terms of the Young-Laplace equation, showing the validity of this continuum-scale equation for these nanoscale structures.

Our molecular dynamics simulation results enabled us to evaluate properties of polymer nanofibers at the molecular level as a function of fiber size, and thereby understand the origin of transition from the regime of bulk-like behavior to that of nanomaterial behavior. It also allowed us to estimate and predict some properties that are challenging to measure due to the limitations of experimental capabilities. With these modeling tools and results in hand, we now know that the structural, thermal and mechanical properties change as the polymer nanofibers are made smaller. This realization should thus be considered while designing polymer nanofibers for selected design objectives.

Our second main focus was to investigate the interfiber interactions between polymer nanofibers. For this purpose, we employed two different techniques; molecular dynamics simulations similar to the ones explained above and energy minimization, or molecular statics (MS). We studied the interfiber interactions between prototypical polymeric fibers of C100 chains that are 4.6 nm in diameter. Our MD simulations showed that fibers aligned parallel and within 9 nm of one another experience a significant force of attraction. These fibers tend to coalesce on a very short time scale, even below T_g. In

contrast, our MS simulations suggest an interfiber interaction that transitions from an attractive to a repulsive force at a separation distance of 6 nm. The results of either simulation approach can be used to obtain a quantitative, closed-form relation describing fiber-fiber interactions. However, the predicted form of interaction is quite different for the two approaches. MD predicts an eventual coalescence of the nanofibers with a significant work of adhesion where energy minimization results predict that the interaction between fibers becomes repulsive for smaller separation distances. This difference can be understood in terms of differences in molecular mobility within and between fibers.

The results of our interfiber interaction simulations can be used to interpret experimental observations for electrospun polymer nanofiber mats. Our findings highlighted the role of temperature and kinetically accessible timescales in predicting interface-dominated interactions at polymer fiber surfaces, which is very important not only in determining the physical and functional properties of polymeric nonwoven mats, but also for the purposes of polymer surface characterization.

Our third and final focus was to lay the groundwork for developing a novel method in order to generate nonwoven structures. We employed a stochastic Monte Carlo method in which the fibers consisted of elastic cylinders. We have demonstrated that the model can generate nonwoven mats comprised crimpled fibers and rod-like fibers (representing the different types of materials electrospun into nonwoven mats) and nonwoven mats with different fiber orientations (representing the different processing conditions during electrospinning. The MC presented in this thesis constructs the basis for future studies of the nonwoven mat generation and properties.

Nonwoven mats are of mat lengths of several centimeters and thickness of several millimeters. These mats comprise polymer fibers of diameters in the nanometer scale and several centimeters in length. Thus such nonwoven polymer mats are truly *multiscale* materials. Our model is capable of incorporating *nanoscale* features (i.e., individual fiber properties and interfiber interactions) for the modeling of a macroscale structure. Thus, it

can be used to relate the fiber characteristics to the performance of nonwoven fabrics comprised of these materials in key performance applications.

7.2 Suggestions for future research

7.2.1 MD simulations of larger polymer nanofibers (R_{fiber} > 15 nm)

The molecular dynamics studies of individual nanofibers, which is described in this thesis, examine the properties of nanofibers of radius R_{fiber} < 15 nm. However, the experimental electrospun nonwoven mats usually comprise of nanofibers of R_{fiber} > 100 nm. Thereby, a natural extension of this thesis is to simulate larger polymer nanofibers.

Currently available force fields are quantitatively accurate, and the methods are soundly rooted in statistical mechanics. Variations in polymer structure on the scale of 1-10 nm (comparable to intermolecular interaction distances) can be efficiently simulated, and both bulk and interfacial structure and properties can be determined in a consistent manner. However, current computer speeds are practically limited to studies of O(5000 atoms) and O(10 ns) for molecular dynamics on a single CPU, which generates a nanofiber R_{fiber} = 3.1. nm. For larger fibers, additional techniques are required, such as massively parallel computation and coarse-grained modeling.

We have used both of these techniques in order to create larger nanofibers. The largest system we have simulated consisted of 150,000 C atoms and generated a nanofiber R_{fiber} = 11.5 nm. This simulation required 3 months of real time to simulate this system for 10 ns running LAMMPS in parallel on 18 2.33 GHz processors. Figure 7.1 shows a plot of R_{fiber} (calculated using GDS [1] at 495 K) vs. total number of atoms N in the simulation system. From this figure, it can be seen that, when the total number of atoms in the system is doubled, the new fiber radius is $R_{2N} = 1.26\times R_N$. To generate a fiber with radius R_{fiber} = 100 nm, a total system size of N = 19,200,000 is required. Recently a montmorillonite clay system that consisted of ten million atoms was successfully simulated using LAMMPS on 1024 processors [2]. Thus, if the computational resources

are available, nanofibers of 100 nm ≤ R_{fiber} can be generated using the similar molecular dynamics that are used in this thesis.

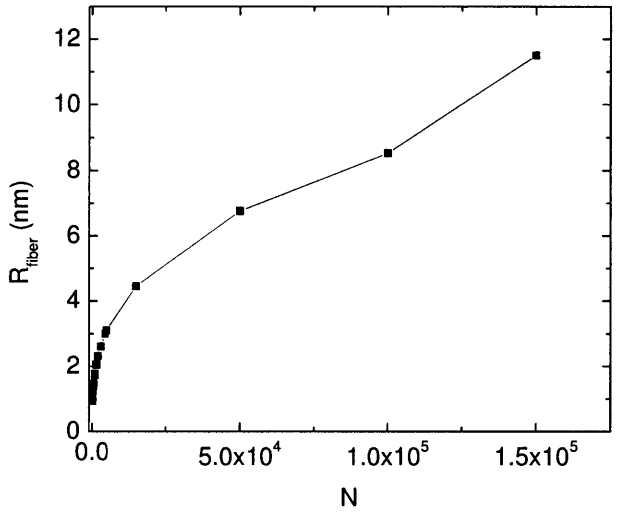

Figure 7.1 R_{fiber} (calculated from GDS for simulations at 495K) vs. total number of C atoms in the simulation system.

Another approach might be to employ the wavelet-based coarse graining procedure (Wavelet Accelerated Monte Carlo, WAMC), which was developed by the Rutledge group. This method employs successive wavelet transformations to represent the polymer chain on increasingly coarse length scales, ranging from atomistic detail to Gaussian-like coils [3]. Using this method, the total computational time can be orders of magnitude less than the equivalent atomistic simulation.

7.2.2 Studying nanoconfined crystallization using MD simulations of crystalline polymer nanofibers

This thesis focused on the properties of amorphous polymer nanofibers. Although it is true that there are some amorphous polymers (i.e., polystyrene, Nylon6(3)) that are electrospun into nanofibers and electrospun mats, several other crystalline polymers (i.e.,

PEO, PCL, PLLA) are also used in electrospinning. The crystallization of a polymer and the extent to which this occurs depends on many factors including confinement. For ex. the effect of nanoconfinement upon the crystallization behavior of PCL has been investigated by Zhang et al. and low percentage of crystallinity was found for nanoconfined PCL relative to that for PCL homopolymer [4]. Molecular simulation methods can also be used to study nanoconfined crystallization and they have the advantage of studying free-standing systems of the polymer, which eliminates the effect of interaction between the polymer and the confining walls. Then the inherent influence of the confinement to a nanoscale environment will be solely responsible for any differences in the crystallization of the confined polymer and the same polymer in its unconfined melt. Nanofiber simulations are a good candidate for such systems. One study investigated the crystallization of a confined, short polyethylene chain n-tetracone, quenched from the melt by a dynamics Monte Carlo method on high coordination lattice [5]. It was found that crystallization produces a single crystalline domain, in which the chains are oriented parallel to the fiber axis, in contrast with the multiple, differently oriented crystalline domains that are usually produced in the similar quench of a free-standing thin film. Similar simulations can be used to investigate nanoconfined crystallinity using the MD techniques described in this thesis. Previous molecular dynamics studies, using the same force field that is used in this thesis [6-8], successfully captured the crystallization of polyethylene. The technique used in these studies can be used to analyze confined crystallization of different polymers in nanofibers and compare it with the bulk polymer crystallization.

7.2.3 Interfiber interactions for different fiber sizes and orientations

The inter-fiber interaction studied in this thesis represents the interaction between parallel polymeric fibers of C100 chains that are 4.6 nm in diameter. One extension to this study would be to study this interaction for different polymer fiber diameters to investigate if the fiber size has an effect on this interaction. Another interesting extension to this study would be to investigate the effect of orientation on the inter-fiber interaction. The orientation of one fiber with respect to the other change the effective interaction area

between the fibers. While parallel configuration (when fibers are placed on top of each other in a parallel fashion), which is studied in this thesis, represents the largest interaction area, the perpendicular alignment (when fibers are placed on top of each other in a perpendicular fashion) represents the smallest interaction area between the fibers. Wu et al. showed that the adhesive force and the area of contact decrease rapidly with the increase of the angle between two filaments [9]. Orthogonal filaments were found to have the minimum adhesive force and the minimum area of contact zone.

Molecular dynamics simulations that are used in this thesis can be used to study both the effect of fiber diameter and orientation on the inter-fiber interactions. Simulating larger nanofibers would require large computational resources, as explained in Section 7.2.1.

7.2.4 Measurement of interfiber interactions by experiments

One of the challenges in the macroscopic modeling of nonwoven materials is the accurate representation of the fiber-fiber contact interactions. Several models have been developed, each based on various assumptions of fiber-fiber interactions, without confirmation by direct experimental measurements or finer-scale simulations. Direct experimental measurements of fiber-fiber interactions are very challenging, particularly for polymeric fibers of sub-micrometer diameter, due to the difficulty of isolating and handling fiber-fiber couples and the uncertainties involved in measuring forces and energies at this scale. However, advances in experimental techniques will allow measurement of such small forces and energies and eventually will enable us to compare our results with these measurements. For ex. direct measurement of single gecko foot-hair was reported by using a 2-D micro-electro-mechanical systems force sensor and a wire force gauge [10]. The dual-axis atomic force microscopy (AFM) cantilever with independent piezoresistive sensors used in this study was previously developed by Chui et al. [11] for simultaneous detection of vertical and lateral forces. This cantilever can perform microfriction measurements as well as obtain simultaneous vertical-force and lateral-force AFM images [11]. With the advancement of experimental techniques that

would enable handling of fiber couples and measurement of interaction forces between these fibers, the effect of inter-fiber interactions on the nonwoven mats can be studied.

7.2.5 Improvements to the MC model and characterization of mat properties

While the MC model described in this thesis is a promising method to generate nonwoven mats and to investigate nonwoven mat properties, several open questions need to be answered to understand the capabilities and the limits of the model.

As briefly mentioned at the end of Chapter 6, the interfiber interaction potentials derived in Chapter 5 have not yet been implemented in the model. These interactions are very important in determining the mechanical properties of the nonwoven mats since they control how the load is transferred from one fiber to another. Once they're implemented, the effect of different type of potentials on the mechanical properties of the nonwoven mats can be analyzed. The results of such a study can help us understand and possibly explain the deformation mechanisms of nonwoven mats at the fiber level, which is not possible with the current experimental techniques.

Another interesting study would be to perform a systematic parametric analysis of the important dimensionless variables of the model, to determine the most critical variables and how they affect the results, which would help us understand the model in more detail.

Once the model is thoroughly studied, many characteristics of the nonwoven mats can be quantified in detail for several properties including pore size and shape distributions; tortuosity and pore interconnectivity; resistance to vapor transport; effective surface area of fabric for different sized reagents; surface roughness and effective liquid-solid contact angle and mechanical response of the mesh under different loading conditions. These characteristics, and their dependence on fiber size and method of fabrication, are crucial to understanding and designing better filtration media, permselective membranes for personal protection garments against chemical and biological warfare agents, durability of the fabric to thermal cycling and mechanical loading.

For example pore size and shape distributions can be quantified by making use of algorithms that are used to calculate free volume in molecular simulations [12, 13]. Misra et al. [12] determined the free volume in polybutadiene by hard spherical probes that see the atoms as hard spheres of radii which equal 89% of their van der Waals radii. The total free volume, the free volume distribution, and the shape of the voids were analyzed. In't Veld et al. [13] developed an algorithm that is based on energetic rather than geometric considerations, and used it to determine the cavity size distribution in liquids. It is applicable to any liquid structure, including polymers, and is readily extended to fiber nonwovens. Tomadakis et al. [14] applied a Brownian diffusion random-walk simulation technique to obtain the pore size distribution and its moments in random and ordered array of fibers. Brownian diffusion random walk method can also be used to calculate the properties of the nonwoven networks. The mechanical properties of the nonwovens (i.e. Young's modulus) and effects of inter-fiber interaction, fiber size and fiber orientation on these mechanical properties can also be investigated. These results can be compared with the experimental mechanical properties which can be easily determined with today's experimental capabilities.

7.2.5.1 Preliminary results for mechanical characterization of the nonwoven mats

In order to demonstrate how the mechanical characterization of the nonwoven mats can be achieved, we have calculated the Young's modulus of the nonwoven mats that have been generated with the system parameters (N = 100, d_0/R = 2, L/d_0 = 49, G/E = 0.3, R = 2.5×10^{-7} m and $E = 4\times10^9$ N/m^2) as explained in more detail in Section 6.4.3. In these simulations, Young's modulus of the single nanofibers as well as the average radius of the nanofibers were matched with the electrospun Nylon6(3) mats. While the random mats were created with T^* = 10, the aligned mats were created with T^* = 0.05. Once the mats were generated, the uniaxial deformation was imposed by displacing the fiber junctions affinely to a predetermined strain. While this was done along a random direction for the random mats, the mats that composed of oriented fibers were strained either parallel to the aligned fiber direction or perpendicular to the aligned fiber direction

in order to investigate the differences between the two. After the mats were deformed, the minimum energy of the system was calculated by using a conjugate gradient energy minimization algorithm. The stress at a given strain was calculated from

$$\sigma_i = \frac{1}{V_0}\left[\frac{\partial E}{\partial \varepsilon_i}\right]_{T,\varepsilon_{k\neq i}} \tag{7.1}$$

for the nonwoven structures at the end of energy minimization simulation. The stress vs. strain plot for uniaxially stretched random mats is given in Figure 7.2. Similarly, the stress vs. strain plots for the uniaxially stretched oriented nonwoven mats are given in Figures 7.3 (deformed parallel to the aligned fiber direction) and 7.4 (deformed perpendicular to the aligned fiber direction). Uniaxial testing results of the corresponding Nylon6(3) electrospun mats were also given in the same figures in order to compare the stress-strain behavior of MC model generated mats and experimentally produced nonwoven mats.

As it can be seen from these figures, the MC model generated mats capture the linear elastic deformation behavior of the Nylon6(3) mats effectively. The Young's modulus values, which are calculated from the slope of the stress-strain curves from both data (i.e., MC generated mats and Nylon6(3) mats) are summarized in Table 7.1 and compare well with each other. However, the stress increases with increasing strain after the linear elastic region for the MC generated mats while the stress exhibits a turn and levels off (which can be a signature of yielding of the material) in case of the Nylon6(3) mats. This can be due to many reasons including the fact that the fibers continue to deform elastically even at large strains (in case of the MC generated mats) since the elastic beam theory was chosen to represent the deformation behavior of the individual segments that make up these fibers. It can also be due to the assumption of the interfiber potential (since the load is transferred from one fiber to another through this interaction) or the number of fiber-fiber contacts. A thorough investigation of the MC model (including studying the effect of each dimensionless parameter and different interfiber interactions) is required to

answer several questions that arise as a result of mechanical characterization of these mats.

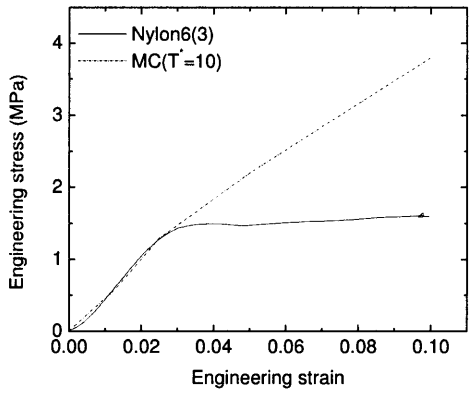

Figure 7.2 Stress-strain response of random Nylon6(3) nonwoven mats compared with MC generated random mats.

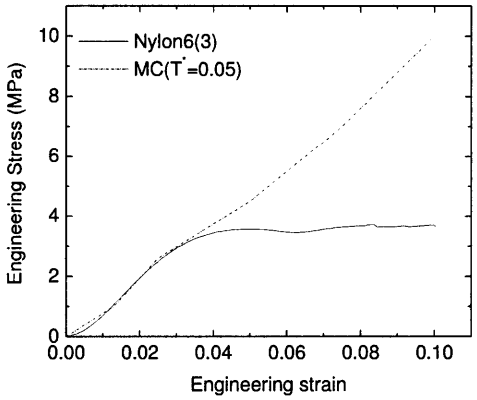

Figure 7.3 Stress-strain response of Nylon6(3) nonwoven mats comprised of oriented fibers compared with MC generated mats. Unixial deformation was applied parallel to the aligned fiber direction.

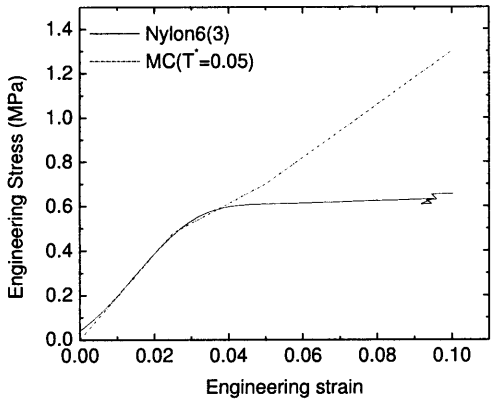

Figure 7.4 Stress-strain response of Nylon6(3) nonwoven mats comprised of oriented fibers compared with MC generated mats. Unixial deformation was applied perpendicular to the aligned fiber direction.

Mat	Random	Parallel	Perpendicular
Nylon6(3) (MPa)	20.5±3.8	129.3±6.4	20.5±3.8
MC generated (MPa)	19.2	104	21.2

Table 7.1 The Young's modulus values, which are calculated from the slope of the stress-strain curves of MC generated mats and Nylon6(3) mats.

REFERENCES

[1] Curgul S.; Van Vliet K.J.; Rutledge G.C. *Macromolecules* **2007**, *40*, 8483.

[2] Suter J.L.; Coveney P.V.; Greenwell H.C.; Thyveetil M.A. *J. Phys. Chem. C* **2007**, *111*, 8248.

[3] Ismail A.E.; Stephanopoulos G.; Rutledge G.C. *J. Polym. Sci. Phys.* **2005**, *43*, 897.

[4] Zhang Q.; Wang M.; Wooley K.L. *Current Organic Chemistry* **2005**, *9*, 1053.

[5] Xu G.Q.; Vao-soongnern V.; Mattice W.L. *Macromol. Theo. Sim.* **2002**, *11*, 494.

[6] Waheed N.; Lavine M.S.; Rutledge G.C. *J. Chem. Phys.* **2002**, *116*, 2301.

[7] Ko M.J.; Waheed N.; Lavine M.S.; Rutledge G.C. *J. Chem. Phys.* **2004**, *121*, 2823.

[8] Waheed N.; Ko M.J.; Rutledge G.C. *Polymer* **2005**, *46*, 8689.

[9] Wu X.F.; Dzenis Y.A. *J. Phys. D. App. Phys.* **2007**, *40*, 4276.

[10] Autumn K.; Liang Y.A.; Hsieh S.T.; Zesch W.; Chan W.P.; Kenny T.W.; Fearing R.; Full R.J. *Nature* **2000**, *405*, 681.

[11] Chui B.W.; Kenny T.W.; Mamin H.J.; Terris B.D.; Rugar D. *App. Phys. Lett.* **1998**, *72*, 1388.

[12] Misra S.; Mattice W.L. *Macromolecules* **1993**, *26*, 7174.

[13] In't Veld P.J.; Stone M.T.; Truskett T.M.; Sanchez I.C. *J. Phys. Chem. B* **2000**, *104*, 12028.

[14] Tomadakis M.M.; Robertson T.J. *J. Chem. Phys.* **2003**, *119*, 1741.

APPENDIX A: DERIVATION OF T_g LAYER MODEL FOR DIFFERENT SHAPES

If we consider an ellipsoid with semi-major axes of length a, b and c, of which the outermost layer having thickness ξ(T) is considered to be "surface" material with a glass transition temperature $T_g = T_{g,surf}$, and the remaining core material exhibits a glass transition $T_g = T_{g,bulk}$, then a simple volume-averaged T_g can be calculated as:

$$T_g = T_{g,bulk} - \left[\frac{(ab+ac+bc)\xi(T_g)}{abc} - \frac{(a+b+c)(\xi(T_g))^2}{abc} + \frac{(\xi(T_g))^3}{abc} \right] (T_{g,bulk} - T_{g,surf}) \quad \text{(A1)}$$

For a thin film, a = $h_{1/2}$ and $b = c \to \infty$ resulting in the thin film equation:

$$T_g = T_{g,bulk} - \frac{\xi(T_g)}{h_{1/2}} (T_{g,bulk} - T_{g,surf}) \quad \text{(A2)}$$

For a cylinder, a=b=R and $c \to \infty$, so we obtain the nanofiber result:

$$T_g = T_{g,bulk} - \left[\frac{2\xi(T_g)}{R} - \left(\frac{\xi(T_g)}{R} \right)^2 \right] (T_{g,bulk} - T_{g,surf}) \quad \text{(A3)}$$

where the factor of 2 in the linear term is due to the two-fold symmetry of the cylindrical cross-section.

For a sphere, a=b=c=R, so we obtain:

$$T_g = T_{g,bulk} - \left[\frac{3\xi(T_g)}{R} - 3\left(\frac{\xi(T_g)}{R} \right)^2 + \left(\frac{\xi(T_g)}{R} \right)^3 \right] (T_{g,bulk} - T_{g,surf}) \quad \text{(A4)}$$

where the factor of 3 in the linear and quadratic terms is due to the three-fold symmetry of the sphere.